Atmospheric washout of radioactive aerosol for different types of precipitation events

Felix Bernauer

München 2015

Aus dem Institut für Strahlenschutz
des Helmholtz Zentrum München
Aufsichtsratsvorsitzende: MinDir'in Bärbel Bumme-Bothe

Atmospheric washout of radioactive aerosol for different types of precipitation events

Felix Bernauer

Dissertation
zum Erwerb des Doktorgrades der Naturwissenschaften
an der Medizinischen Fakultät
der Ludwig–Maximilians–Universität
München

vorgelegt von
Felix Bernauer
aus Eggenfelden

2015

Mit Genehmigung der Medizinischen Fakultät
der Universität München

Erstgutachter: Prof. Dr. Werner Rühm
Zweitgutachter: Prof. Dr. Gunnar Brix
Dekan: Prof. Dr. med. dent. Reinhard Hickel
Tag der mündlichen Prüfung: 15.12.2015

Abstract

Ionizing radiation is widely used in many applications such as medical diagnostics and radiotherapy, where the beneficial aspect of radiation exposure is obvious. However, the exposure of human beings to ionizing radiation may also have some negative effects on human health.
After the Fukushima Dai-Ichi nuclear power plant accident measured deposition patterns did not match to patterns predicted by atmospheric transport models used in decision support systems. It was suggested that one reason for these discrepancies might be that these models do not differentiate between deposition by rain and snow. Up to now much effort has been spent on the theoretical and experimental investigation of the washout of atmospheric aerosol particles by rain. In contrast, only limited knowledge is available on the washout efficiency of snow, due to the complexity of the process.
Therefore, the aim of the presented work was to analyze wet deposition of aerosol particles and particle bound radionuclides in different types of precipitation events. The thesis focused on below-cloud scavenging of aerosol particles in a size range from 10 nm to 510 nm in solid phase precipitation events. It is based on measurements of natural precipitation and natural aerosol particle concentration that were performed in the free atmosphere, at the Environmental Research Station Schneefernerhaus.
For this purpose, a method was developed to characterize and classify precipitation events, which goes beyond the common differentiation between liquid, mixed and solid phase precipitation. The method included use of a 2D-Video Disdrometer (2DVD), that was adapted for the detection of mixed and solid phase hydrometeors (e.g. snowflakes). A new matching algorithm, that was developed for this thesis, allowed detection of solid, mixed and liquid phase hydrometeors with a maximum dimension larger than 0.5 mm. On the basis of shape and velocity descriptors, a classification algorithm that differentiates between three classes of crystal types and three classes of riming was developed.
A number of meteorologically stable precipitation events was identified, including 34680 minutes of precipitation with 74% in solid, 19% in mixed and 7% in liquid phase. In agreement with literature the calculated scavenging coefficients were found in a range from $(5.0\pm0.7)\cdot10^{-5}\,\mathrm{s}^{-1}$ to $(1.0\pm0.2)\cdot10^{-3}\,\mathrm{s}^{-1}$. As expected, the scavenging coefficients showed a clear *Greenfield gap* between 30 nm and 60 nm.
The Greenfield gap was more pronounced for liquid phase events than for mixed and solid phase events. In the particle size range between 30 nm and 60 nm solid phase events showed the largest scavenging coefficients. Due to the very efficient interception and impaction mechanisms, mixed phase

events showed the largest scavenging coefficients for aerosol particles larger than 60 nm. For solid phase precipitation events, and aerosol particles larger than 30 nm, the dependence of the scavenging coefficient on maximum dimension and vertical velocity was not as pronounced as the dependence on hydrometeor crystal type and surface structure. As expected, all types of precipitation showed increasing mean scavenging coefficients averaged over the whole aerosol particle size range, for increasing precipitation rates. The clearest dependence of the scavenging coefficient on precipitation rate was observed for liquid phase precipitation, while for solid phase precipitation additionally to the precipitation rate also hydrometeor crystal type and surface structure played an important role.
Parameterizing the scavenging coefficient λ as a function of precipitation rate I using the equation $\lambda = A \cdot (I/I_0)^B$, is commonly done in decision support systems and atmospheric transport models. The values for A and B are fixed and do not depend on the type of precipitation. The most important result of this study is that precipitation events consisting of different types of hydrometeors can be parametrized by different values of A and B, for a range of precipitation rates from $0.1\,\mathrm{mmh}^{-1}$ to $4.0\,\mathrm{mmh}^{-1}$. For water equivalent precipitation rates of less than $1.5\,\mathrm{mmh}^{-1}$, snow turned out to show larger scavenging coefficients than rain. More specifically, the scavenging coefficients for snow and rain can differ by up to a factor 8 for precipitation rates of less than $0.5\,\mathrm{mmh}^{-1}$. This can be one reason for the discrepancies observed in Fukushima between predicted and observed wet deposition.
Therefore, it is recommended that different parameterizations of the scavenging coefficient for different types of precipitation events, as reported in this thesis for the first time, should be implemented into decision support systems and atmospheric transport models. This will allow a more reliable estimate of the exposure of the public to ionizing radiation, in the case of accidental atmospheric release of radionuclides.

Zusammenfassung

Ionisierende Strahlung hat in vielen Anwendungsbereichen vorteilhafte Eigenschaften, wie zum Beispiel in der medizinischen Diagnostik oder in der Strahlentherapie. Es existieren jedoch auch verheerende negative Auswirkungen ionisierender Strahlung auf die Gesundheit des Menschen.
Nach dem Umfall im Kernkraftwerk Fukushima stimmten gemessene und von atmosphärischen Ausbreitungsmodellen vorhergesagte Depositionsmuster nur schlecht überein. Diese Unterschiede wurden zum Teil darauf zurück geführt,

dass die verwendeten Modelle nicht zwischen der Deposition durch Regen und der durch Schnee unterscheiden. Zum derzeitigen Stand der Forschung existieren zahlreiche theoretische sowie experimentelle Studien zum Auswaschen atmosphärischen Aerosols durch Regen. Wegen seiner Komplexität und wegen seiner vielfältigen Erscheinungsformen gehört die Auswascheffizienz von Schneefall zu den bisher unzureichend untersuchten Größen.
Es war die zentrale Aufgabe der hier vorgestellten Arbeit, die Auswascheffizienz von Regen, Schnee und Schneeregen zu analysieren und gegenüberzustellen. Besonderes Augenmerk wurde dabei auf die Auswascheffizienz verschiedener Arten von Schneekristallen gerichtet. Der untersuchte Aerosolpartikelgrößenbereich lag zwischen 10 nm und 510 nm.
Ein 2D-Video-Disdrometer (2DVD) wurde für die Aufzeichnung von Schnee und Schneeregen modifiziert. Zur Charakterisierung und Klassifizierung von Schneefall wurden computergestützte Routinen entwickelt und in die Analyse-Software des 2DVD eingebunden. So konnten Regen-, Schnee- und Schneeregenereignisse mit Hydrometeorgrößen über 0.5 mm zuverlässig aufgezeichnet werden. Durch die Einführung von Faktoren zur Beschreibung der Hydrometeoroberflächenstruktur und Größen-Geschwindigkeitsrelation wurde ein Klassifizierungsalgoritmus entwickelt, der zwischen drei verschieden Kristalltypen und drei verschiedenen Bereifungsgraden unterscheiden kann.
Alle aufgezeichneten Niederschlagsereignisse wurden auf ihre meteorologische Stabilität analysiert und aussortiert. So stand ein Datensatz bestehend aus 34680 Minuten Niederschlag mit 74% Schnee, 19% Schneeregen und 7% Regen zur weiteren Untersuchung zur Verfügung. In guter Übereinstimmung mit Werten aus früheren Studien wurden Auswaschkoeffizienten zwischen $(5.0 \pm 0.7) \cdot 10^{-5}\,\mathrm{s}^{-1}$ und $(1.0 \pm 0.2) \cdot 10^{-3}\,\mathrm{s}^{-1}$ gefunden, die die erwartete Abhängigkeit vom Aerosolpartikeldurchmesser zeigten (*Greenfield gap*).
Für Regen wurde ein stärker ausgeprägtes Minimum bei Aerosolpartikeldurchmessern zwischen 30 nm und 60 nm gefunden als für Schnee und Schneeregen. Für Aerosolpartikeldurchmesser zwischen 30 nm und 60 nm zeigte Schnee die größten Auswaschkoeffizienten. Aufgrund von sehr effizienten Interceptions- und Impaktionsmechanismen wurden die höchsten Auswaschkoeffizienten für Schneeregen bei Partikeldurchmessern über 60 nm gemessen. Schneefallereignisse zeigten eine stärkere Abhängigkeit des Auswaschkoeffizienten vom Kristalltyp und der Hydrometeoroberflächenstruktur im Vergleich zur maximalen Dimension und vertikalen Fallgeschwindigkeit. Alle Niederschlagstypen zeigten ein klares Wachstum des Auswaschkoeffizienten mit zunehmender Niederschlagsrate.
In Entscheidungshilfesystemen für Notfälle wird der Auswaschkoeffizient λ mit Hilfe des Potenzgesetzes $\lambda = A \cdot (I/I_0)^B$ in Abhängigkeit von der Niederschlagsrate I parametrisiert. Die Werte für A und B sind dabei fest und hän-

gen nicht von der Art des Niederschlages ab. Ein zentrales Ergebnis dieser Arbeit ist, dass verschiedene Typen von Niederschlagsereignissen mit Intensitäten zwischen $0.1\,\mathrm{mmh}^{-1}$ und $4.0\,\mathrm{mmh}^{-1}$ mit verschiedenen Werten für A und B parametrisiert werden können. Besonders bei Niederschlagsereignissen mit schwachen Intensitäten (ca. $0.5\,\mathrm{mmh}^{-1}$) kann der Auswaschprozess durch Schneefall ca. achtmal effizienter als der durch Regen sein. Dies kann eine mögliche Ursache für die starken Unterschiede zwischen beobachteter und vorhergesagter nasser Deposition sein, die im Umkreis von Fukushima festgestellt wurden.
Die in der vorliegenden Arbeit zum ersten Mal vorgestellten Parametrisierungen des Auswaschkoeffizienten für verschiedene Arten von Niederschlag können in atmosphärischen Ausbreitungsmodellen implementiert werden. So trägt diese Arbeit dazu bei, dass verlässlichere Abschätzungen der Exposition der Bevölkerung mit ionisierender Strahlung möglich sind, falls es zu einer Freisetzung radioaktiven Materials in der Atmosphäre kommt.

Contents

Chapter 1

Introduction

Ionizing radiation is widely used in many applications such as medical diagnostics and radiotherapy, where the beneficial aspect of radiation exposure is obvious. However, the exposure of human beings to ionizing radiation may also have some negative effects on human health, and radiation protection aspects such as the internationally applied concept to keep radiation exposure as low as reasonably achievable should be considered in any exposure situation. Effects that are directly linked to the radiation dose can be subdivided into two main groups. Effects that are certain to occur under given exposure conditions are called deterministic effects. The acute radiation syndrome, for example, occurs when an individual is exposed to a dose of several grays over a short period of time (UNSCEAR, 2011). The second group is called stochastic effects that may occur when individuals are exposed especially to low doses of radiation. The major stochastic effect of ionizing radiation on human health, that could be demonstrated in human populations, is cancer (UNSCEAR, 2011). To take the right measures of remediation in case of exposure to ionizing radiation, it is important to have as much knowledge as possible about the absorbed dose and about the nature of the exposure.
One possible exposure pathway starts with the release of radionuclides (i.e. particles emitting ionizing radiation) to the atmosphere in accidental situations involving nuclear facilities. In this context the radionuclides Iodine-131 (^{131}I, $t_{1/2}$ = 8.02 days) and Cesium-137 (^{137}Cs, $t_{1/2}$ = 30.07 years) are of great importance, because they are produced in nuclear reactors as fission products and because they are volatile and readily released in an accidental radioecological event. Inhalation or ingestion of ^{131}I increases the risk of thyroid cancer and other thyroid diseases, while long-lived ^{137}Cs becomes distributed in soft tissues and its inhalation or ingestion increases the risk of various cancers (Hoeve and Jacobson, 2012). One example for such a radioecological emergency situation is the accident that happened in March

2011 in the Fukushima Dai-ichi Nuclear Power Plant. During this event large amounts of radioactive material were discharged into the atmosphere, mainly ^{131}I and ^{137}Cs (Terada et al., 2012). A significant fraction of this radioactive material was attached to aerosol particles and followed the pathways of atmospheric aerosols.

Two mechanisms, called dry and wet deposition, dominate the transfer of atmospheric aerosol particles from the atmosphere to the Earth's surface. The term wet deposition includes all processes associated with clouds and precipitation while the term dry deposition refers to processes taking place in absence of clouds and precipitation. Wet deposition can take place inside a cloud when aerosol particles serve as condensation nuclei and form cloud droplets. These droplets grow larger and are finally removed from the cloud in precipitating hydrometeors (e.g. snowflakes). On their way from the cloud base to the Earth's surface, falling hydrometeors can take up aerosol particles from the atmosphere and deposit them onto the ground. According to the locations where these processes take place they are called *in-cloud* and *below-cloud* scavenging.

In case of emergency situations with the risk of exposure to ionizing radiation, decision support systems help decision makers to perform appropriate actions of remediation (Raskob and Ehrhardt, 1999; Terada et al., 2004; Nasstrom et al., 2007). These computer-based systems rely on atmospheric transport models in which wet deposition plays a major role. Generally, the implementation of wet deposition into these atmospheric transport models does not consider different types of precipitation such as rain or snow. In studies by Morino et al. (2011) and Yasunari et al. (2011) on the deposition of radionuclides accompanying the accident in the Fukushima Dai-Ichi nuclear power plant, large discrepancies between calculated and observed deposition of the released radionuclides ^{131}I and ^{137}Cs were found. The authors of these studies attributed these differences to uncertainties in the treatment of emission, transport and deposition of radionuclides in the models.

The aim of the presented study was to analyze the washout efficiency of different types of precipitation in an effort to provide first experimental data on snow scavenging to be implemented in state of the art atmospheric models for decision support systems. The study focuses on the below-cloud scavenging coefficient for particle bound radionuclides in solid phase precipitation events. An outstanding feature of this study is the experimental determination of the dependence of the scavenging coefficient on hydrometeor crystal type and hydrometeor surface structure, under free atmospheric conditions. One central aspect was the improvement of instrumentation and software for solid phase precipitation measurements with a 2D-Video Disdrometer (2DVD by Joanneum Research, Austria). Furthermore, a universally appli-

cable method for solid phase precipitation classification according to hydrometeor surface structure was developed.
Scavenging coefficients were calculated from the results of continuous aerosol particle size distribution measurements using the well established differential mobility analyzer technique (Scanning Mobility Particle Sizer, SMPS by TSI, USA). Size-resolved collection of aerosol particles in a 14-stage cascade impactor delivered the database for activity size distribution measurements (Electric Low Pressure Impactor, ELPI+ by Dekati, Finland).
In addition the temporal development of atmospheric activity concentration during precipitation events was monitored by collecting bulk aerosol samples on fiber filters with a high volume aerosol sampling station (Aerosol Sampling Station, ASS1000 by PTI Fischer, Germany). With the results of these measurements activity scavenging coefficients were calculated.
Combining theses methods has the following advantages: A high temporal resolution for the calculation of scavenging coefficients is necessary to minimize the effect of mixing different types of precipitation. Aerosol particle size distributions are measured with high temporal resolution (approximately ten minutes) by the SMPS. The activity concentration measurements with the high volume sampling station allow for a detailed analysis regarding the contents of particle bound radionuclides. However, they have a relatively coarse temporal resolution of approximately two hours. Precipitation event characterization and classification, aerosol particle size dependent scavenging coefficients, activity size distributions and development of atmospheric activity concentration during precipitation build the basis for detailed statements on the efficiency of below-cloud scavenging of particle bound radionuclides in different types of precipitation events which will be reported for the first time in the present study.
Finally, based on the results obtained in the present work, recommendations for the further development of atmospheric transport models with respect to the implementation of wet deposition of different types of precipitation events are given, which will allow the improvement of state of the art decision support systems used in Germany and other countries.

Chapter 2

Theory and state of the art

2.1 Characterization and classification of precipitation

Observation of precipitation micro structure is of high interest in many areas of research. Not only the parametrization of wash out efficiency of particle bound radionuclides and atmospheric pollutants in general (Sportisse, 2007; Kyrö et al., 2009; Paramonov et al., 2011) require detailed characterization and classification of precipitation. But also the development, improvement and verification of numerical weather prediction models (Xue et al., 2000) and radar back scatter computations for microwave frequencies (Hiroshi, 2008) need precise observations of precipitation micro structure.
Solid precipitation micro structure can be described by analyzing single hydrometeors conserved on *Formvar* slides in the microscope (Schaefer, 1956). Zikmunda (1972) could observe hydrometeor micro structure together with fall speed by using stereo-photography and Frank et al. (1994) measured rain drop size distributions by using a CCD camera in combination with a proper illumination unit and digital image processing. Ground based observations with so called video disdrometers are a more recent development and meanwhile commonly used because of the large amount of data that can be retrieved in a flexible and low cost way compared to for example airborne particle probe imagers (Feind, 2008). Video disdrometer technique is well established for measurements of rain micro physics (Tokay et al., 2001; Schuur et al., 2001; Thurai and Bringi, 2005; Zhang et al., 2008; Thurai et al., 2009, 2014). Brandes et al. (2007) used 2D video disdrometer technique for a statistical description of hydrometeors in snowstorms. Huang et al. (2010) developed a methodology to derive radar reflectivity to liquid equivalent snow rate relations, and Zhang et al. (2011) described winter pre-

cipitation micro physics with a 2D-video disdrometer. Recently, 2D-video disdrometer technique was used by Grazioli et al. (2014) for an automatic snow event classification. The type of 2D-video disdrometers as described by Kruger and Krajewski (2002) gives supplementary details due to its two orthogonal views of the detected hydrometeors.
Another type of optical disdrometer which has two parallel light planes is the hydrometeor velocity and shape detector (HVSD) used for size and velocity measurements of liquid and solid phase precipitation (Barthazy et al., 2004; Barthazy and Schefold, 2006). The study from Battaglia et al. (2010) about a comparison between a 2D-video disdrometer and a Particle Size Velocity disdrometer (PARSIVEL) (Löffler-Mang and Joss, 2000) comes to the conclusion that both instruments have shortcomings in measuring size distributions and fall velocity of solid phase precipitation.
The present work also includes a classification of solid phase precipitation events according to the dominating degree of riming and crystal type of single hydrometeors. Classification methods based on the decision of an expert observer can be very detailed but they are time consuming and the amount of data that can be processed is limited. In contrast, automatic methods based on computational analysis allow for extensive studies involving a huge amount of data but require extensive and independent verification measurements. Commonly used among automatic methods are fuzzy logic and neural fuzzy logic systems in combination with polarimetric radar data (Starka et al., 2000; Liu and Chandrasekar, 2000; Lim et al., 2005). Grazioli et al. (2014) and Gavrilov et al. (2015) processed data retrieved with a 2D-video disdrometer in machine learning classification algorithms.
In this work a 2D-Video Disdrometer (2DVD, compact version by Joanneum Research, Graz, Austria) delivers detailed data on micro physical parameters of hydrometeors such as size, shape and vertical velocity. With the 2DVD data in combination with detailed on site observations a decision tree approach is derived for solid phase precipitation event classification according to the dominating degree of riming and crystal type of hydrometeors contained in one minute intervals of precipitation. The method has the advantage of being independent and universally applicable because it is simply based on constraints for the ranges of directly measured shape and velocity parameters.

2.2 Aerosol particle size distributions

It is widely accepted that the washout efficiency for atmospheric aerosol depends on the particle size of the scavenged aerosol. Therefore, the aerosol

particle size distribution is an important parameter in the present study. In general aerosol particle size distributions are described mathematically by so called log-normal distributions:

$$\frac{df}{d\log(d_p)} = \frac{N}{\sqrt{2\pi}\log(\sigma_g)} \exp\left(-\frac{(\log(d_p) - \log(\bar{d_{p_g}}))^2}{2(\log(\sigma_g))^2}\right) \tag{2.1}$$

$$\log(\bar{d_{p_g}}) = \frac{\sum N_i \log(d_{p_i})}{N} \tag{2.2}$$

$$\log(\sigma_g) = \left(\frac{\sum N_i(\log(d_p) - \log(\bar{d_{p_g}}))^2}{N-1}\right)^{1/2} \tag{2.3}$$

N denotes the total particle number, $\log(\bar{d_{p_g}})$ is the geometric mean and $\log(\sigma_g)$ stands for the standard deviation of the distribution of particle diameters d_p. In this discrete notation the summation over the subscript i stands for a summation over specific particle size classes. Particle size distributions of atmospheric aerosol are well characterized by a trimodal model consisting of three additive log-normal distributions. The exact parameters describing a single mode depend on time and location of a specific measurement. But in general for the geometric mean sizes the following typical values are found (Whitby, 1978):

- Nucleation mode: 0.015 μm to 0.04 μm
- Accumulation mode: 0.15 μm to 0.5 μm
- Coarse mode: 5 μm to 30 μm

The smallest mode is called nucleation mode. It contains so called secondary aerosol particles originating from combustion processes or from gas-to-particle conversions. Usually their life time is relatively short (in the order of one to three days) and they grow through coagulation to larger accumulation mode particles. The region between nucleation and accumulation mode is sometimes referred to as Aitken mode which contains older nucleation mode particles between 0.06 μm and 0.15 μm. The coarse particle mode contains primary aerosol particles originating for example from wind blown dust, sea spray, volcanic eruptions or plants (Whitby, 1978).

2.3 The radionuclides of interest

To draw conclusions on the wet deposition of particle bound radionuclides the development of atmospheric activity concentrations of the naturally occurring isotopes Beryllium-7 (^{7}Be) and Lead-210 (^{210}Pb) as well as the anthropogenic Cesium-137 (^{137}Cs) is investigated.

- ^{7}Be is a cosmogenic isotope with a half life of $t_{1/2} = 53.3$ days. Its production mainly takes place in the upper troposphere and lower stratosphere by interactions of cosmic rays with atmospheric nitrogen and oxygen. ^{7}Be atoms are attached to atmospheric aerosol particles soon after their formation. With the advantage of the short half life and relatively easy determination, ^{7}Be has been widely used as a tracer in atmospheric science (Winkler et al., 1998; Doering, 2007; Ioannidou and Paatero, 2014).

- ^{210}Pb is a progeny of ^{222}Rn. The main source of atmospheric ^{210}Pb is the emanation of short lived ^{222}Rn from the continents. ^{210}Pb atoms become quickly attached to aerosol particles after their formation in the planetary boundary layer. Therefore, they are associated with the aerosol population and allow the investigation of tropospheric transport and removal processes. ^{210}Pb is widely used in atmospheric research and modeling (Winkler et al., 1998; Winkler and Rosner, 2000). It has a half life of $t_{1/2} = 22.3$ years.

- The isotope ^{137}Cs has a half life of $t_{1/2} = 30.07$ years and is produced anthropogenically by several types of nuclear activities including past testing of nuclear weapons, accidents in nuclear facilities, reprocessing of spent nuclear fuel and nuclear power reactors. The atmospheric activity of ^{137}Cs in central and northern Europe is expected to be strongly controlled by the influence of the Chernobyl nuclear power plant accident in April 1986 (Kulan, 2006).

2.4 Below-cloud scavenging

In general the process of wet deposition is dominated by two mechanisms called in-cloud and below-cloud scavenging. This work focuses on the mechanism of below-cloud scavenging which summarizes all processes associated with the capture of aerosol particles by falling hydrometeors on their way from the cloud base to the Earth's surface. In theory the efficiency of below-cloud scavenging is described by the so called *below-cloud scavenging coefficient* λ (subsequently referred to as *scavenging coefficient*). The following

integral describes the aerosol particle size dependent scavenging coefficient $\lambda(d_p)$ mathematically for a polydisperse distribution of hydrometeor diameters D (Sportisse, 2007):

$$\lambda(d_p) = \int_0^\infty \frac{\pi}{4} D^2 v(D) E(D, d_p) n_h(D) dD \tag{2.4}$$

This integral over the whole hydrometeor size range is dominated by three factors:

- The factor $\frac{\pi}{4} D^2 v(D)$ describes the volume that is swept out by a falling hydrometeor with diameter D and vertical velocity $v(D)$. The equilibrium between the downward oriented gravitational force and the upward oriented drag force caused by friction between the hydrometeor surface and the surrounding air determines the vertical fall velocity. Several studies have been conducted on the relationship between size and velocity of falling hydrometeors. The most important ones for this study are summarized graphically in Fig. 2.1. The equation (Atlas et al., 1973)

  $$v(D) = 9.65 - 10.3 \cdot e^{-0.6 \cdot D} \tag{2.5}$$

  reliably describes the size-velocity relation for raindrops. For solid phase precipitation Hanesch (1999), Locatelli and Hobbs (1974) and Barthazy and Schefold (2006) found a wide range of velocities for hydrometeors with a single size depending on their surface structure.

- The factor $n_h(D)$ describes the hydrometeor size distribution. Many different expressions exist for the hydrometeor size distribution. The most common one is the Gamma-distribution:

  $$N(D) = N_0 \cdot D^\mu \cdot \exp(-\Lambda D) \tag{2.6}$$

  D is the hydrometeor diameter, N_0 [$mm^{-\mu-1}$ m^{-3}] is a number concentration parameter, μ is a distribution shape or curvature parameter and Λ [mm^{-1}] is a slope term. The distribution parameters depend on the precipitation rate and the type of precipitation. Typical values for precipitation rates of 3.0 mmh^{-1} found in literature are summarized in Tab. 2.1.

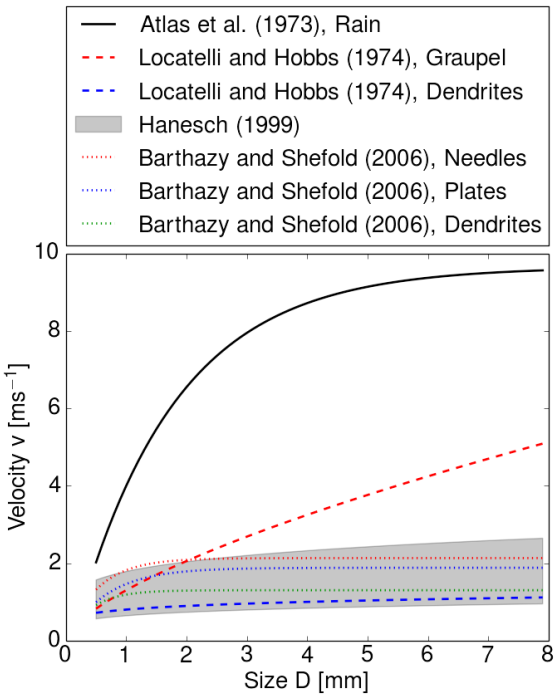

Figure 2.1: Size-velocity relationships for different types of hydrometeors as reported in literature. The term *size* means *diameter* in case of rain, in case of snow it means *height* or *maximum dimension*.

Table 2.1: Typical values for the Gamma-distribution parameters (Eq. 2.6) representing hydrometeor size distributions for precipitation rates of 3.0 mmh^{-1}.

precipitation type	N_0 [mm$^{-\mu-1}$ m^{-3}]	Λ [mm^{-1}]	μ
Marshall and Palmer (1948)	$8.0 \cdot 10^3$	3.3	0
Drizzle, Joss and Waldvogel (1969)	$30.0 \cdot 10^3$	4.5	0
Thunderstorm, Joss and Waldvogel (1969)	$1.4 \cdot 10^3$	2.4	0
Snow, Brandes et al. (2007)	$(0.07 \text{ to } 23.3) \cdot 10^3$	0.35 to 2.25	-0.78 to 1.23

- The so called collection efficiency $E(D, d_p)$ describes the ratio of collected particles to the particles contained in the volume swept out by the hydrometeor. The major contributors to the collection efficiency are the mechanisms of Brownian diffusion, interception and impaction

(Fig. 2.2). Especially for smaller aerosol particles (around 10 nm) Brownian diffusion is a very efficient process. For larger aerosol particles (around 1.0 μm), interception and impaction play the major role. For interception, the cross sectional area between aerosol particle and hydrometeor plays the major role while for impaction, it is the fact that larger and heavier aerosol particles cannot follow the streamlines around the hydrometeor and therefore, impact on its surface. The aerosol particle size range in between is less efficiently scavenged. This relationship between aerosol particle diameter and collection efficiency was first observed by Greenfield (1957) and is therefore called *Greenfield gap*. According to a comprehensive review by Sportisse (2007), values for the size range of the Greenfield gap reported in literature range from 0.01 μm to 2.0 μm.

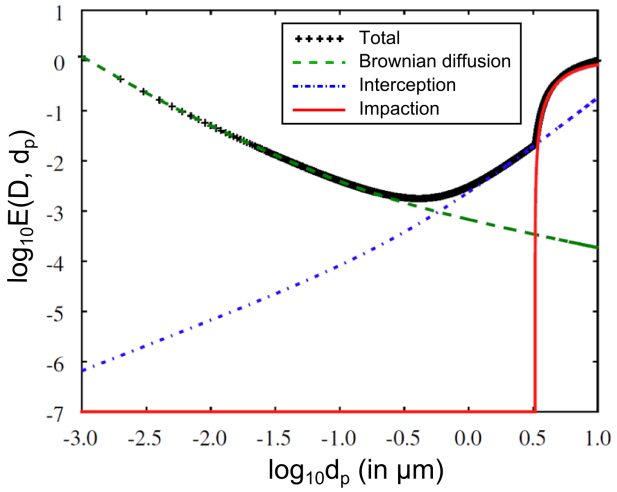

Figure 2.2: Contributions of Brownian diffusion, interception and impaction for $E(D, d_p)$. From Sportisse (2007)

According to Pruppacher and Klett (1978) the width and the depth of the Greenfield gap is sensitive to phoretic and electric forces. For solid phase precipitation the collection efficiency is expected to be strongly influenced by the crystal type and the surface structure of the hydrometeors (Kyrö et al., 2009).

2.5 Existing studies on rain and snow scavenging

In past years many laboratory, field and theoretical studies have been conducted on rain and snow scavenging. Mitra et al. (1990) and Bell and Saunders (1995) analyzed the washout efficiency of different types of artificial snow crystals for laboratory generated aerosol particles larger than $0.2\,\mu$m in cold chamber experiments. Outdoor experiments with artificial tracer aerosol and natural snowflakes by Sauter and Wang (1989), Sparmacher et al. (1993) and Tschiersch et al. (2000) lead to the conclusions that the washout efficiency depends on the snow crystal type and that snow scavenging is more efficient than rain scavenging.
Early studies using direct measurements of atmospheric aerosol particle concentration during real snowfall events were done by Magono et al. (1974). Graedel and Franey (1974) explain the high washout efficiencies for snow with the large effect of thermal turbulence and Brownian motion for falling snowflakes and measure scavenging coefficients between $4.8 \cdot 10^{-4}\,\mathrm{s}^{-1}$ and $6.3 \cdot 10^{-3}\,\mathrm{s}^{-1}$. Hydrometeor concentrations and the temporal evolution of aerosol with different meteorological conditions in a winter precipitation field study at Mt. Rigi, Switzerland were investigated by Schumann et al. (1988) and Volken and Schumann (1993). They measured aerosol particle size dependent scavenging coefficients from $10^{-4}\,\mathrm{s}^{-1}$ to $10^{-5}\,\mathrm{s}^{-1}$ for an aerosol particle size range from $0.6\,\mu$m to $10\,\mu$m. Kyrö et al. (2009) studied snow scavenging of ultra fine aerosol particles at a boreal site in Finland. They measured a median snow scavenging coefficient of $1.8 \cdot 10^{-5}\,\mathrm{s}^{-1}$ which applies for slight continuous snow fall with low intensities up to $0.8\,\mathrm{mmh}^{-1}$. A very similar study for an urban site in Finland was conducted by Paramonov et al. (2011). In addition they presented a parametrization of the scavenging coefficient regarding aerosol particle diameter and relative humidity. In both studies the need of further investigation of snow scavenging with respect to precipitation rate and crystal type is underlined.
Work on rain scavenging in combination with parametrization of the scavenging coefficient taking the dependency from the precipitation rate into account was published by Laakso et al. (2003). Chate and Pranesha (2004) measured rain scavenging coefficients of up to $7.6 \cdot 10^{4}\,\mathrm{s}^{-1}$ for an aerosol particle size range from $0.013\,\mu$m to $0.75\,\mu$m in field experiments. Andronache et al. (2006) implemented their observations of rain scavenging to a model that includes below-cloud scavenging processes, mixing of ultra fine particles from the boundary layer into the cloud, as well as cloud condensation nuclei activation and in-cloud removal by rainfall.

In recent years much effort has been spent on the parameterization of below cloud scavenging which is essential for the implementation to atmospheric transport models (Croft et al., 2009; Feng, 2009; Wang et al., 2010, 2011; Chate, 2011; Chate et al., 2011). A very comprehensive overview on the modeling of below cloud scavenging by rain and snow and the uncertainties associated with the use of different parameterizations is given by Zhang et al. (2013). From this publication also Fig. 2.3 is taken which summarizes the results from the most recent field and theoretical studies on below-cloud scavenging.

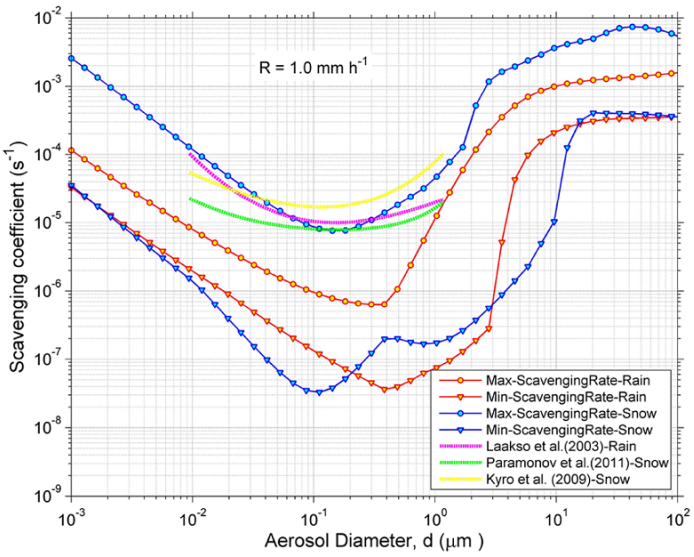

Figure 2.3: Minimum and maximum below-cloud scavenging coefficients calculated for rain and snow with different parameterizations for a preciptation rate of $R = 1.0\,\mathrm{mmh}^{-1}$. Additionally the results from field studies by Laakso et al. (2003), Kyrö et al. (2009) and Paramonov et al. (2011) are shown. From Zhang et al. (2013).

Concerning particle bound radionuclides Ioannidou and Papastefanou (2006) published a work on atmospheric depositional fluxes of ^{7}Be and ^{137}Cs. They found that snowfall is more efficient than rainfall in removing the radionuclides from the atmosphere. A review of parameterizations for modeling scavenging of radionuclides is given by Sportisse (2007). A parameterization very commonly used in decision support systems (Raskob and Ehrhardt, 1999; Terada et al., 2004; Nasstrom et al., 2007) is represented by the formula

$$\lambda = A \left(\frac{I}{I_0} \right)^B \tag{2.7}$$

where I is the precipitation intensity, I_0 is a normalization factor and A and B are aerosol particle size dependent coefficients. Typical values used for example in the Real-time On-line Decision Support system for off-site emergency management in Europe (RODOS) are $A = 8.0 \cdot 10^{-5}\,\mathrm{s}^{-1}$ and $B = 0.8$ (Thykier-Nielsen et al., 1999).

Chapter 3

Description of the measuring site

3.1 Location of the Schneefernerhaus

The Environmental Research Station Schneefernerhaus (UFS) is located at the south slope of Mt. Zugspitze, which is part of the Wettersteingebirge in the south of Germany. With an elevation of 2650 m a.s.l. the station represents a high alpine site (Fig. 3.1). Very good transport connections via train and cable cars provide easy access to the station all over the year. Electricity and internet access is provided at the station which is permanently maintained and supervised by a supporting staff. The station is organized as a virtual institute and is supported by the Bavarian Government. Research groups working at the UFS include those from the German Aerospace Center (DLR), the *Deutscher Wetterdienst* (DWD), the *Helmholtz Zentrum München* (HMGU), the Karlsruhe Institute of Technology (KIT), the *Ludwig Maximilians Universität München* (LMU), the Max Planck Society (MPG), the *Technische Universität München* (TUM), the Federal Environment Agency (UBA) and the University of Augsburg.

Figure 3.1: The Environmental Research Station Schneefernerhaus.

3.2 Meteorology

Data sampling for this study took place from November 2012 to December 2014. Monthly average values of temperature, amount of precipitation and snow depth recorded at the DWD weather station Zugspitze are shown in Fig. 3.2 for the years 2013 and 2014. In the summer months June, July, August and September mean temperatures are slightly above the freezing point. The average temperatures over the whole years were −3.9°C for 2013 and −3.1°C for 2014 which are quite high values compared to the long range average temperature of −4.8°C given by the DWD for the period from 1961 to 1990. In 2013 62% of the total precipitation fell in periods with negative mean temperature, while it was 60% in 2014. With a total precipitation amount of 1905.4 mm in 2013 and 1969.4 mm in 2014, about 2.6 times more precipitation was registered than on average for the rest of Germany (752.9 mm average precipitation amount for 2013 and 2014). The maximum snow depth was measured with 480 cm in June in 2013 and with 400 cm in May in 2014. Except from August the whole year long a snow cover could be observed.

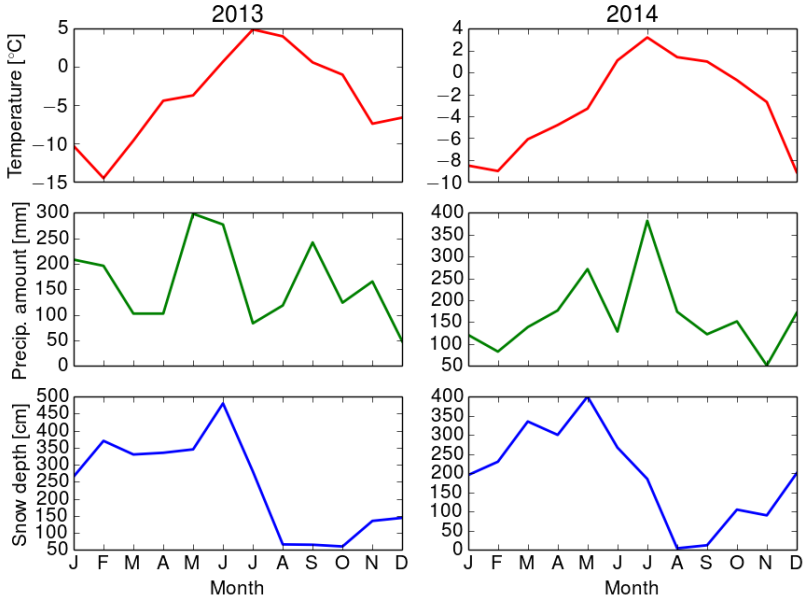

Figure 3.2: Meteorological data from from the DWD weather station Zugspitze provided by the *Deutscher Wetterdienst*.

3.3 Aerosol

The present work deals with the variation of aerosol particle concentration during precipitation events. For this reason the general physical characteristics of the aerosol at the measuring site are important. A comprehensive study on the physical characteristics of the aerosol occurring on Mt. Zugspitze was conducted from 2005 to 2007 by Birmili et al. (2007).
In their study Birmili et al. (2007) investigated the aerosol particle size range from 10 nm to 600 nm. In general, they measured relatively clean air in wintertime with particle concentrations between 540 cm^{-3} and 1700 cm^{-3} depending on the origin of the air masses. It is noted that mostly free tropospheric conditions determine aerosol particle size distributions in winter. Due to boundary layer convection in spring, in summer and in autumn considerably higher particle concentrations from 1400 cm^{-3} to 3300 cm^{-3} were detected.

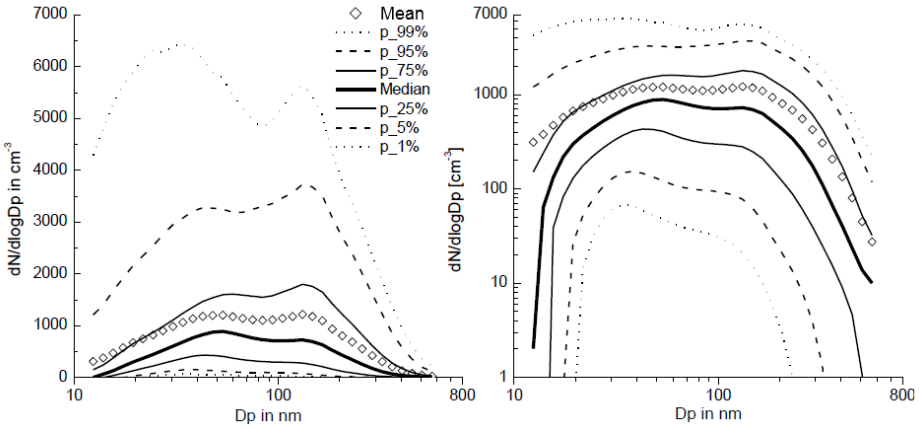

Figure 3.3: Atmospheric particle size distribution at the Schneefernerhaus. Mean values and percentiles of measurements between December 2004 and March 2007 are shown. (modified from Birmili et al. (2007)).

Analyzing the continuously measured particle size distributions from December 2004 to March 2007 showed that 98% of the particle sizes spread over two orders of magnitude (Fig. 3.3 right panel). This spread was approximately equal for the whole observed size range. Another important aspect is that the size distribution clearly showed a bimodal structure consisting of an Aitken mode with a maximum between 30 nm and 60 nm and an accumulation mode with a maximum around 150 nm (Fig. 3.3 left panel). The relative frequency of the mean geometric diameter for 200 fitted log-normal distributions (Fig.

3.4) confirm the bimodal structure of the particle size distribution and allows to choose the following size intervals for the different modes:

- 10 nm - 30 nm: nucleation mode
- 30 nm - 60 nm: young Aitken mode (older nucleation mode particles)
- 60 nm - 150 nm: Aitken mode
- 150 nm - 600 nm: accumulation mode

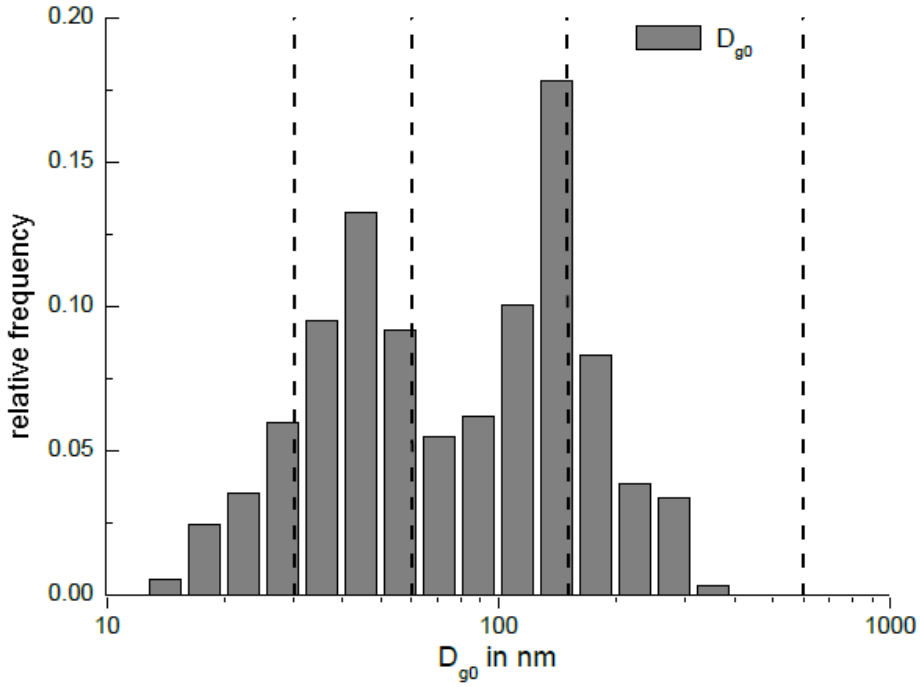

Figure 3.4: Frequency distribution of the mean geometric diameter D_{g_0} of 200 fitted log-normal distributions. The dashed vertical lines indicate the size ranges of the modes (modified from Birmili et al. (2007)).

Fig. 3.5 confirms that the highest particle concentrations of up to 4000 cm^{-3} were measured in the summer months from May to July. The maximum values predominantly occurred in a size range above 100 nm, during the afternoon hours. These accumulation mode particles probably originate from the planetary boundary layer and are transported through convective processes to higher altitudes. In April and August the bimodal distribution could be observed directly. In contrast, most particles measured in January

and December had diameters from 30 nm - 60 nm (young Aitken mode). In general particles from the nucleation and Aitken mode show a much weaker dependence on season or daytime than those from the accumulation mode. One feature should be explicitly mentioned in the context of the present study: Due to the permanent occurrence of nucleation and young Aitken mode particles (10 nm - 60 nm), independent from convective processes, it can be assumed that the source for these particles is not only in the boundary layer but also in the free troposphere. Especially the observation of nucleation mode particles at night seams to contradict to other observations where nucleation was driven photochemically mostly during midday (Birmili and Wiedensohler, 2000). This aspect shows that some unknown processes determine the life circle of aerosol particles, and that there is a continuous source of particle formation during day and night on Mt. Zugspitze.
The aerosol particle size distribution as a function of the local wind direction shows a relatively homogeneous pattern (Fig. 3.6). This observation confirms that particle size distribution on Mt. Zugspitze is generally not influenced much by local sources (Birmili et al., 2007).

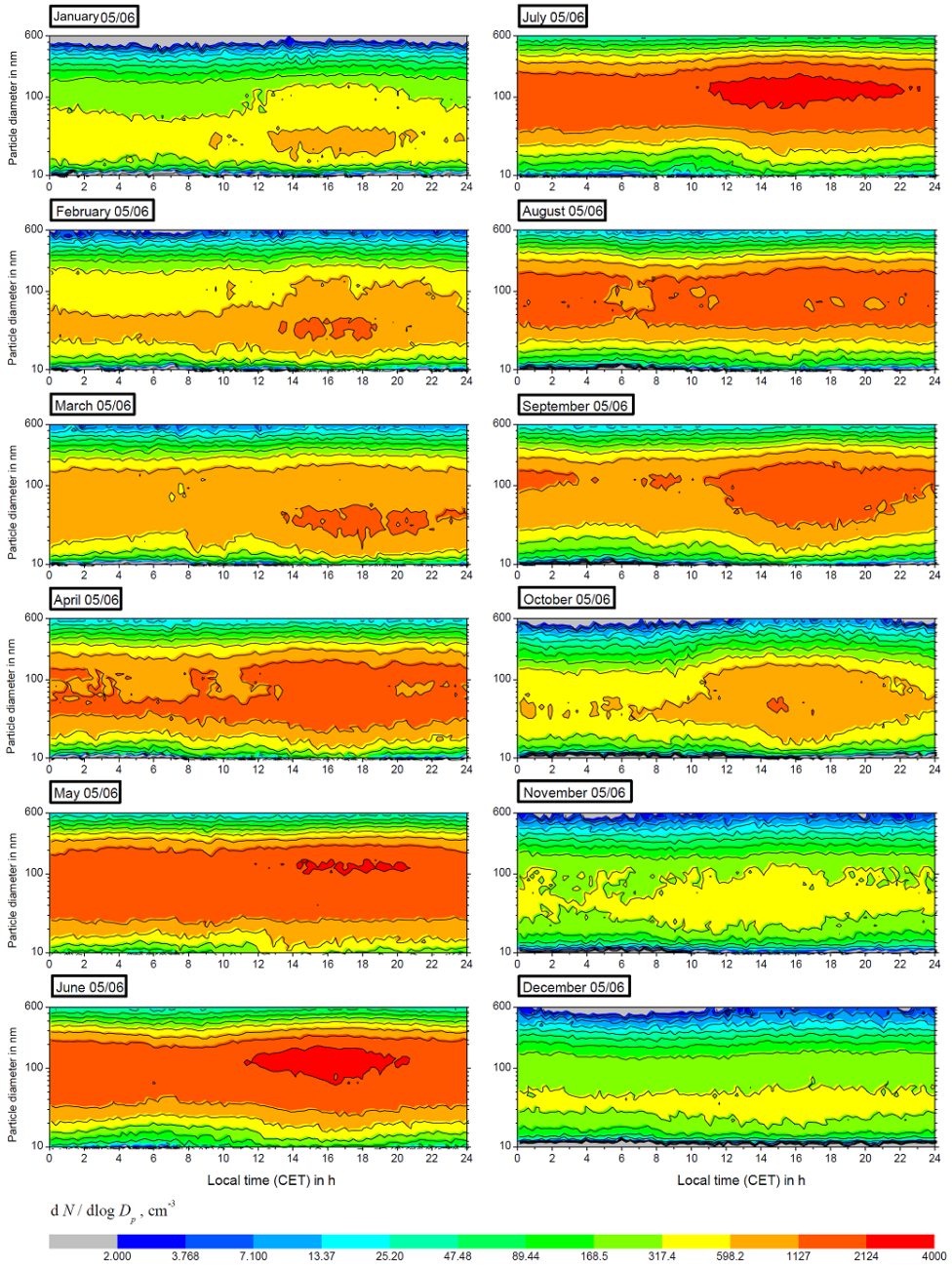

Figure 3.5: Contour diagrams of the particle size distributions at the Schneefernerhaus. Monthly mean values for the period from January 2005 to December 2006 are shown. Ordinates show the particle diameter (from Birmili et al. (2007)).

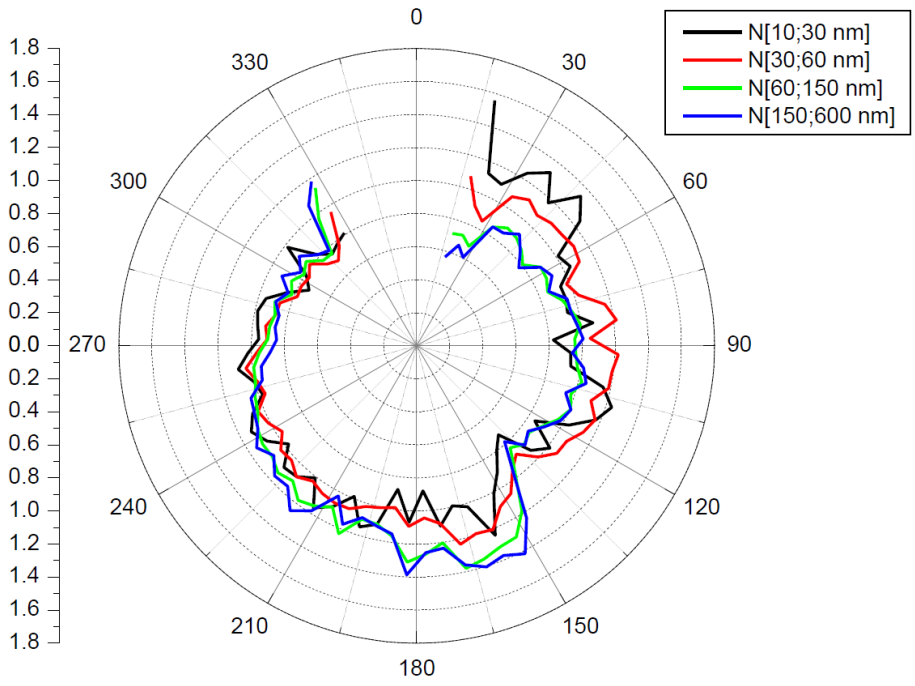

Figure 3.6: Distribution of wind direction and mean particle concentration for different size modes. For better comparability every curve was normalized to a mean value of one (from Birmili et al. (2007)).

Chapter 4

Methods

4.1 Precipitation event characterization and classification

4.1.1 The 2D-Video Disdrometer

4.1.1.1 Principle of operation

One of the primary tasks in this study is the characterization and classification of precipitation events. The instrument used in this study for precipitation event characterization is a Compact 2D-Video Disdrometer (2DVD, by Joanneum Research, Graz, Austria; Fig. 4.1).

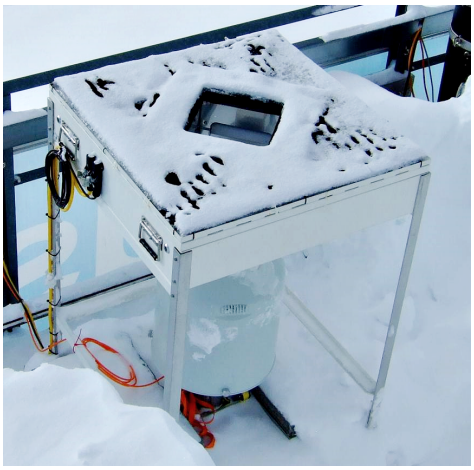

Figure 4.1: The Compact 2DVD at the Environmental Research Station Schneefernerhaus. Below the sensitive area a weighing precipitation gauge is mounted.

A schematic view of the 2DVD measurement principle is shown in Fig. 4.2. The main parts of the device are two illumination units and two CCD line scan cameras. By means of a halogen lamp, a mirror and a Fresnel lens each illumination unit produces an approximately homogenous background light which is scanned by one of the cameras. The combination of the two illumination units and the two cameras results in two light planes that enclose an angle of 90° and have a vertical distance of approximately 6 mm. The exact plane distance can be found with a standard calibration procedure recommended by the manufacturer. The area of overlap is approximately $10 \times 10\,\mathrm{cm}^2$ large and is called the sensitive area. A hydrometeor falling through one of the light planes produces a shadow on a certain amount of pixels in each line. Stacking these lines to a complete picture delivers shape information for every single hydrometeor. A detailed description of an earlier version of the 2DVD and an investigation on its potential in measuring rain parameters can be found in Kruger and Krajewski (2002). The smaller housing design of the Compact 2DVD makes it less sensitive to horizontal winds. Its cameras scan a line containing 632 pixels with a frequency of 55.272 kHz which results in a higher spacial resolution than provided by previous models.

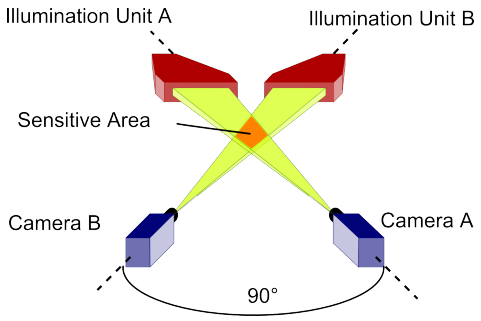

Figure 4.2: Measurement principle of the 2DVD (modified from Kruger and Krajewski (2002)).

4.1.1.2 The matching problem

Every hydrometeor that falls through the 2DVD within the shaded areas (see Fig. 4.3) is seen by at least one camera. But only hydrometeors that are seen by both cameras (cross shaded area) can be used for subsequent data analysis. The most critical step in processing 2DVD raw data is finding exactly that pair of pictures that belongs to the same hydrometeor. This process is called matching.

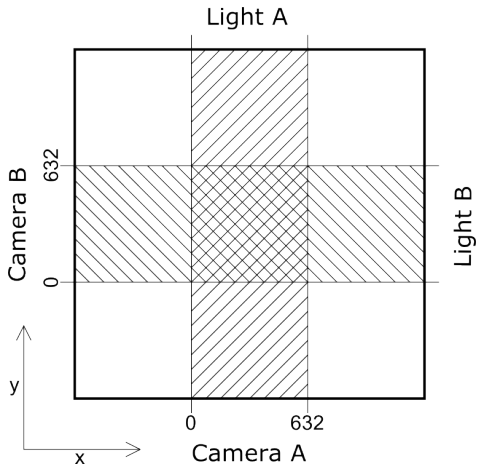

Figure 4.3: A schematic view of the 2DVD measuring area seen from above.

In contrast to rain where a well known symmetry and size-velocity relation can be assumed, the shapes of solid and mixed phase hydrometeors are more complex. This makes it more difficult to find a pair of 2DVD images that belongs to the same hydrometeor. Without implementing an appropriate matching algorithm the probability of errors in shape and velocity measurement through matching artifacts is very high. To find the right matching partner to a picture recorded in camera A a time window has to be defined in which the matching partner has to appear in camera B. The narrower the time window the higher is the probability to find the right match. Raindrops have a well known relationship between their size and terminal fall velocity (Gunn and Kinzer, 1949; Atlas et al., 1973) and the time window can be set very narrow. In case of solid phase precipitation the fall velocity depends not only on size but also on shape and degree of riming (Locatelli and Hobbs, 1974; Barthazy and Schefold, 2006).
A first attempt of solving the matching problem for snow measurements was done by Hanesch (1999). In the present study the approach of Huang et al. (2010) was applied with few modifications. In principle, several ranges of parameters were defined, which the hydrometeors must match to be identified as a single one. Huang et al. (2010) set a fixed velocity range from $0.5\,\mathrm{ms}^{-1}$ to $6.0\,\mathrm{ms}^{-1}$ for the whole size range. In the present work a dynamic upper bound velocity is used for each hydrometeor with the width w. It is set to the velocity $v(w)$ which a raindrop with width w would have (Atlas et al., 1973):

$$v(w) = 9.65 - 10.3 \cdot e^{-0.6 \cdot w} \tag{4.1}$$

This adjustment makes sure that also partially melted and mixed phase hy-

drometeors can be matched. Fig. 2.1 summarizes the size velocity relationships for different types of hydrometeors in a size range from 0.5 mm to 8.0 mm as determined by several investigators. It justifies the assumption of Eq. (4.1) as upper limit.
With the known scan frequency this time window can be translated into an interval of lines in camera B that has to contain the right matching partner (see the shaded region in Fig. 4.4). In the example from Fig. 4.4 three possible matching partners are found within the shaded region. Three so called matching factors are now calculated for each pair of pictures:

- $f_1 = 1 - \frac{|SL_A - SL_B|}{max(SL_A, SL_B)}$
  with $SL_{A/B}$: number of scanned lines in camera A and B
- if $F \leq 1 : f_2 = F$, else: $f_2 = 2 - F$
  with $F = \frac{min(W_{max}, H_{max})}{0.8 \cdot max(W_{max}, H_{max})}$
- $f_3 = W_{min}/W_{max}$

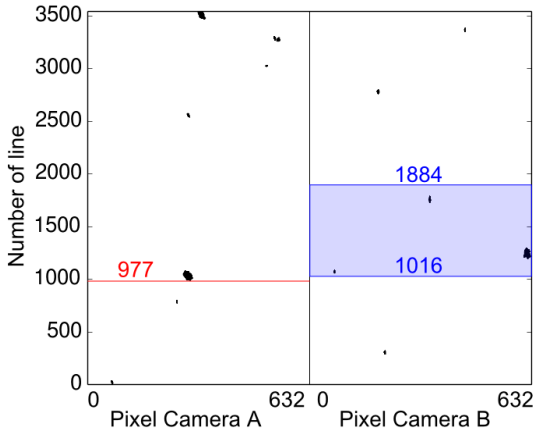

Figure 4.4: This example shows two raw camera streams. For the specific snowflake hitting camera A at the red line, all possible matching partners in camera B are within the shaded region.

W_{max}, H_{max} and W_{min} denote the maximum and minimum height and width in each picture. The final matching function is a weighted sum of all three matching factors (Huang et al., 2010): $f = 0.6f_1 + 0.2f_2 + 0.2f_3$. The matching partner with the highest f is the best match (see Hanesch (1999) and Huang et al. (2010)).

It is worth mentioning that in this study the newly implemented matching algorithm is applied directly to the raw data streams coming from the cameras. The original matching algorithm supplied by the manufacturer (hereafter referred to as *original matching algorithm*) is explicitly not used for the data analysis in this work. Therefore the algorithm used in this study is not called *rematching*. But in the studies from Huang et al. (2010) and Grazioli et al. (2014) the term *rematching* lets the reader assume that the original algorithm is used at some stage of data evaluation.

4.1.1.3 Size, velocity and shape parameters

The result of the matching software is a pair of pictures from each hydrometeor falling through the sensitive area. The great advantage of the 2DVD is that a very detailed set of parameters can be derived from two orthogonal views. For each picture a width (W), a height (H), a perimeter (P) and an area (A) can be defined as in Fig. 4.5. A set of shape characterizing parameters can be assigned to each component of a 2DVD image pair. This work deals with three factors which are commonly used in land use analysis (Jiao and Liu, 2012) and recently also in snow classification (Grazioli et al., 2014).

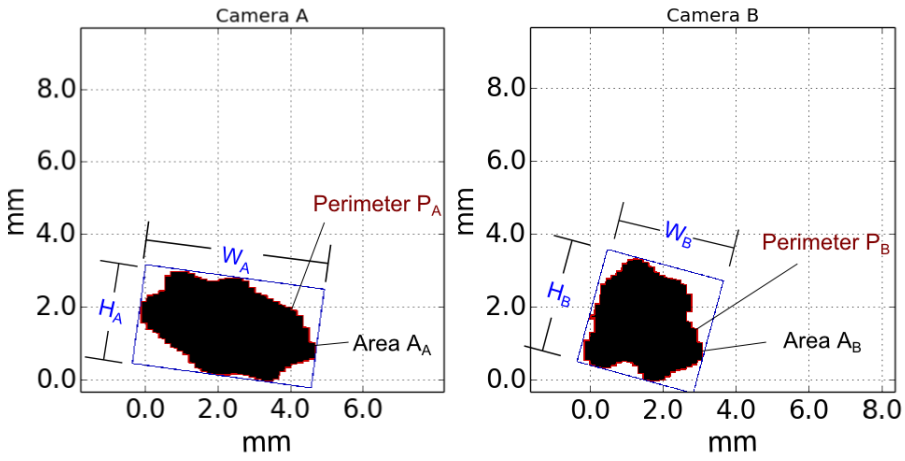

Figure 4.5: The definition of width (W), height (H), perimeter and area for a hydrometeor as recorded with the 2DVD.

a) **Elongation:** $E = \frac{max(W,H)}{min(W,H)}$
The elongation describes the ratio between width and height. The more elongated a hydrometeor is, the larger is E. Needles have a large elon-

gation. Rain and graupel particles have an elongation of approximately one.

b) **Roundness:** $R = \frac{4A}{\pi(max(W,H))^2}$
The roundness is a quantity that describes how well the hydrometeor fills out the area that is enclosed in the circumscribing circle. Needles and dendrites have a low roundness. Rain or graupel particles have a roundness of approximately one.

c) **Shape factor:** $S = \frac{4\pi A}{P^2}$
The shape factor sets the surface area of a particle in relation to its perimeter. An idealy spherical particle has a shape factor of one. Needles and columns have a low shape factor. The shape factor of rain and graupel particles is approximately one.

Another, size describing, set of parameters can be derived with the combination of both camera pictures:

d) The **maximum dimension** D [mm] is the maximum value of width and height seen in both cameras.

e) The **volume** V [mm^3] of a hydrometeor is calculated the following way: Every line scan cuts the hydrometeor into slices. The volume of each slice is defined by the area of an ellipse with the length of the shadowed line in each camera as semi axis and the height of the line. The sum of these volumes is the volume of the hydrometeor.

f) The **equivalent diameter** D_{eqd} [mm] is the diameter a sphere with the same volume as the hydrometeor would have.

g) The **vertical fall velocity** $v(D)$ [ms^{-1}] is the exact plane distance at the (x,y) location of the hydrometeor in the sensitive area divided by the time interval from the first hit in camera A to the first hit in camera B.

An ensemble of hydrometeors that fell during a certain time interval is described with mean values of the mentioned microscopic parameters.

4.1.1.4 Experimental methods

Calibration and validation of shape parameters with solid spheres

Possible misalignment of the optical components due to transport, strong winds and the use of a new data analysis software motivated a recalibration of the device in addition to the calibration done by the manufacturer: For this purpose, steel spheres with diameters from 0.5 mm to 10 mm were dropped through the measuring area. For each size, between 30 and 70 calibration spheres were released from the same height (0.52 m) above the first camera plane, and the values for height and width measured in camera A and B were compared to the known nominal values for the spheres. For the determination of the size of an object, the pixel width p has to be known. This parameter is defined as the actual width of a shaded line divided by the number of shaded pixels n_{pix} and depends on the exact x and y position of the object and on a size dependent correction factor f_{corr} supplied by the manufacturer. Because of the individual positions in the sensitive area, every detected object has its own pixel width:

$$p = p(x, y) \cdot f_{corr} \tag{4.2}$$

$p(x, y)$ denotes the width of a single camera pixel seen from the location (x, y). f_{corr} is the correction factor supplied by the manufacturer. Dropping solid spheres from a known height through the sensitive area is also suitable for verification of shape and velocity measurements because of the following reasons:

- The real values of elongation (E), roundness (R) and shape factor (S) are easily determined as $E = R = S = 1$, for spherical objects.
- The real values of elongation, roundness and shape factor are independent from the orientation of the object to the recording camera, which makes the experiment easily reproducible.
- For spherical objects the expected velocity after a certain distance of free fall can be calculated solving the equation of motion

  $$m\frac{dv}{dt} = mg - \frac{1}{2}\rho C_D A v^2 \tag{4.3}$$

  for Reynolds numbers, Re, between 100 and 2000. m, v and A are the mass, velocity and surface area of the falling object respectively. g is the gravitational acceleration and ρ the air density.

The drag coefficient C_D depends on the Reynolds number and varies approximately linearly from 1.0 for $Re = 100$ to 0.35 for $Re = 2000$.

Test of the matching algorithm

The originally implemented analysis software for solid phase precipitation supplied by the manufacturer was evaluated in the following way: As an example, a real snow fall event was analyzed with the original matching algorithm on the one hand and the established criteria after Hanesch (1999) on the other hand (see Tab. 4.1). These are mainly geometric criteria which snow flakes must fulfill. In addition, particles with velocities larger than $6.0\,\mathrm{ms}^{-1}$ (which is not reasonable for snow) were sorted out.

Table 4.1: Filter criteria for the test of the original matching algorithm (adapted from Hanesch (1999)).

Filter type
$D > 0.2\,\mathrm{mm}$ (spatial resolution, sr)
sr + Velocity: $0.5\ \mathrm{ms}^{-1} < v < 6.0\ \mathrm{ms}^{-1}$
sr + Velocity: $v(D) < v_{Rain}(D)$
sr + Geometry: $0.1 < H/W < 10.0$
$0.1 < W_A/W_B < 10.0$
sr + $H_A - H_B < 0.2H_{max}$

For the evaluation of the performance of the new matching algorithm a reproducible experiment with falling objects that behave like solid or mixed phase precipitation particles was performed. Fourteen irregularly shaped styrofoam particles with different maximum dimensions from 2 mm to 15 mm (Fig. 4.6) were dropped through the sensitive area one after the other. This was repeated five times and the mean value of the measured fall velocity was calculated for each size. In a second step an ensemble of styrofoam particles where each size was represented by at least one particle was released at the same time from the same height as in the first step. By comparing the measured velocities in the second step to those from the first step mismatches could easily be identified. The styrofoam particles were coated with a stabilizing spray color to avoid breaking of the particles, when they hit the ground. A mean density of $270.0\,\mathrm{kgm}^{-3}$ was measured for the particles.

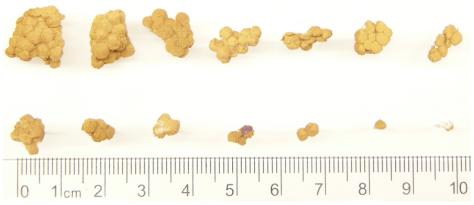

Figure 4.6: Fourteen styrofoam particles with maximum dimensions from 2 mm to 15 mm simulate solid hydrometeors to validate the matching algorithm.

Real snow flakes

A third method for evaluation of 2DVD performance was applied by measuring shape parameters of real precipitation particles. For 38 one minute intervals of solid phase precipitation the mean values of the measured shape parameters were calculated. For an independent verification of the measurement prinziple, the self-consistency of 2DVD measured shape parameters was tested. Events with high mean elongation are expected to have low mean roundness and low mean shape factor and vice versa. Events with a low mean shape factor should also have a low mean roundness.

4.1.2 Precipitation event classification

In this work a precipitation event classification according to parameters that are expected to influence the scavenging coefficient is developed. Precipitation events are classified according to the phase of the hydrometeors into liquid phase (rain), solid phase (snow) and mixed phase (a mixture of rain and snow). Solid phase events are further subdivided into three classes of crystal types and three classes of riming.
The precipitation event classification consists of two major steps. First, all precipitation events are subdivided into the three phases of hydrometeors, solid, liquid and mixed. The three phases of hydrometeors are visually identified by analyzing the size velocity distribution for each individual event. Typical size velocity distributions for liquid, mixed and solid phase events are shown in Fig. 4.7. In liquid phase events hydrometeors follow the relation established by Atlas et al. (1973) (dashed line, a), hydrometeors in solid phase events have lower velocities and spread over a wide range for a single size (Hanesch (1999), shaded region, c) and mixed phase events clearly show both branches (b). In a second step all solid phase events are classified using the method described in detail in the next sections.

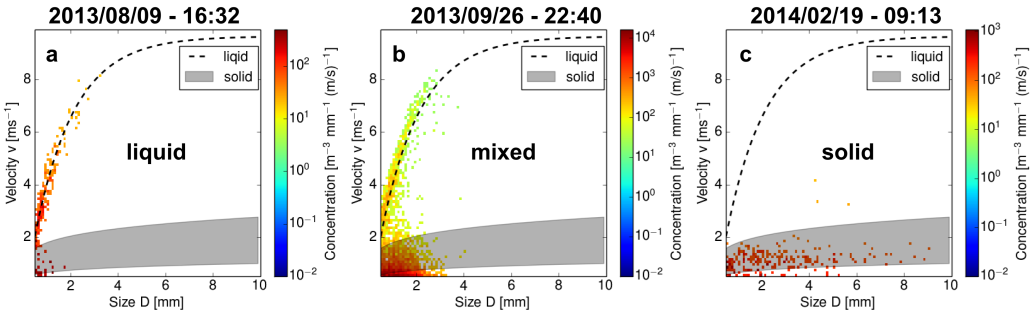

Figure 4.7: Size velocity distributions for the three phases of precipitation events. The dashed line represents the relation established by Atlas et al. (1973) for rain, the shaded region represents the region established by Hanesch (1999) for solid phase events. Typical examples for liquid phase (a), mixed phase (b) and solid phase (c) are shown.

4.1.2.1 Data processing for solid phase precipitation

The 2DVD delivers a pair of pictures for each hydrometeor that fell through the sensitive area. For each picture the perimeter P, the area A, the width W and the height H are derived for further image processing. With these quantities the shape factor S and the roundness R of the hydrometeor are calculated. Additionally the vertical velocity v is measured by the 2DVD. In general the terminal fall velocity of a hydrometeor depends on its size (Atlas et al., 1973). For solid phase hydrometeors the size velocity relation $v(D)$ tends to follow a power law:

$$v(D) = \alpha \cdot D^{\beta} \tag{4.4}$$

where D is the maximum dimension and the coefficient α and the exponent β depend on the dominating surface structure of the hydrometeors (Locatelli and Hobbs, 1974; Barthazy and Schefold, 2006). The coefficient α and the exponent β are found with a least squares fit of Eq. (4.4) to the measured size velocity distribution.

4.1.2.2 The classes of solid phase precipitation

In the following a classification of solid phase precipitation events with respect to fall velocity and surface structure of hydrometeors is introduced. For solid hydrometeors the main factors determining the fall velocity and the surface structure are the degree of riming and the crystal type.
On the surface of weakly rimed hydrometeors only a few cloud droplets are

observed. When half or more of the hydrometeors surface is covered with cloud droplets it is considered as moderately rimed. Strong riming is observed when the total hydrometeor surface is covered with one ore more layers of droplets (Tab. 4.2 modified after Barthazy and Schefold (2006)).

Table 4.2: The different degrees of riming.

Degree of riming	Coverage of surface	Description
weak (1)	$\leq 25\%$	Only a few droplets can be found on crystal surface.
moderate (2)	$\approx 50\%$	Approximately half or more of the surface is covered with droplets.
strong (3)	$\geq 100\%$	The whole crystal surface is covered with one or more layers of droplets.

Solid phase precipitation events were subdivided into three classes of dominating crystal type (Tab. 4.3). The class of *complex crystals* (c) contains aggregates of single crystals and irregular shaped crystals, such as broken dendrites. Also dendritic structures are included in this class. The *single crystals* class (s) contains only hydrometeors with needle, column ore plate like structures that do not stick together. The class called *pellets* (p) contains mainly hydrometeors with spherical structures. Graupel, snow pellets and ice pellets are included herein as well as very densely rimed hydrometeors.

Table 4.3: The three classes of dominating crystal type.

crystal type	description
complex crystals (c)	irregular crystals and aggregates of single crystals
pellets (p)	nearly round particles including very strong riming and graupel
single crystals (s)	isolated single plates, needles or columns

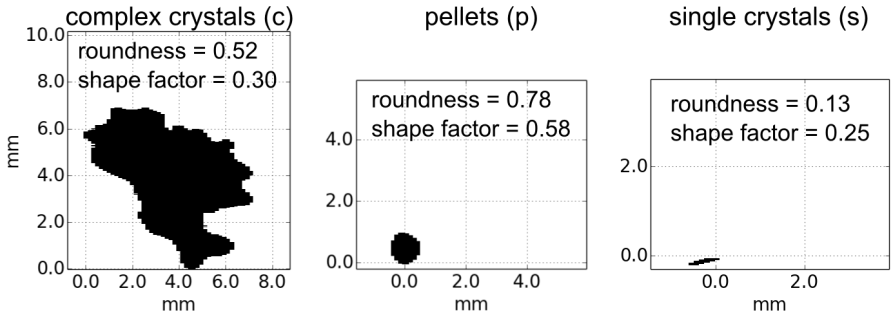

Figure 4.8: The three classes of crystal types with the corresponding shape descriptors.

4.1.2.3 The data set for development of the classification

The 2DVD data sampling took place from November 2012 to December 2014. To develop the classification algorithm, 38 snowfall events each lasting one minute were considered and the degree of riming and the dominating crystal type were visually determined on site. In addition, for each of these 38 events the recorded 2DVD pictures were classified visually, i. e., each recorded picture was labeled with one of the dominating crystal type classes depending on its similarity to one of the pictures in Fig. 4.8. Each event was labeled with the crystal type class dominating the pictures. This procedure is further referred to as *visual picture classification*. Tab. 4.4 summarizes the on-site observations and the visually identified classification (last column). The picture classification was done by two independent observers. For validation of the classification algorithm the visual picture classification was done for further 33 one-minute events. Independently from these well characterized one-minute events three snowfall events lasting two to four hours are taken as examples to show consistency with bulk density and temperature measurements. In these three events a total of 468 minutes of snowfall was classified.

4.1.2.4 The classification method

Once the discrimination in the dominating crystal type and degree of riming is introduced, an automatic classification scheme for the 2DVD must be established.
The parameter that reflects the degree of riming in the 2DVD measurements is the vertical fall velocity (Barthazy and Schefold, 2006). For unrimed or weakly rimed snow crystals the terminal fall velocity does not increase with

increasing size because the increase of friction dominates the increase of mass in the balance of forces. Riming creates a smoother surface, it decreases the friction and increases the mass. The fit parameter β from the power function fit to the size velocity diagram (see Eq. 4.4) reflects this behavior: A low value for β means a large curvature and the velocity remains small also for larger hydrometeors. In contrast, a large value for β means a low curvature and the velocity increases with size.
In terms of parameters measured with the 2DVD it is possible to discriminate the crystal type classes by means of the roundness R and shape factor S. Fig. 4.8 shows a typical picture for every class of crystal types along with the calculated roundness and shape factor. Single crystals appear elongated and show a small roundness and shape factor. In contrast pellets have a regular shape and mainly convex features with high roundness and shape factor. Finally complex crystals are irregular and have an intermediate roundness and shape factor.
The ensemble of hydrometeors that was observed during a one-minute interval was described with the velocity fit parameter β and the mean values for the roundness R and the shape factor S. The basic idea behind the classification method is to find the ranges of the values of the velocity fit parameter β, the roundness R and the shape factor S, for a certain class of riming and a certain class of crystal type. These ranges are implemented in a classification algorithm that takes β, the mean roundness and the mean shape factor for a one-minute event as input parameters and returns the dominating degree of riming and the dominating crystal type in a tuple (t, r), where t stands for the crystal type and can be s, p, or c. r denotes the degree of riming which is 1, 2 or 3. A one-minute event classified as $(c, 2)$ would describe a solid phase precipitation event containing mostly moderately rimed complex crystals. Ambiguous events are labeled as *not classified*.
On the one hand the short time step of one minute guaranties to minimize the effect of mixing different hydrometeor types, on the other hand it is long enough for the event to contain a sufficient number of hydrometeors even for events with low precipitation rate.

4.1.3 The density of snow flakes

For the derivation of the precipitation rate from the microscopic quantities measured with the 2DVD the equivalent amount of water contained in a snow flake is an important parameter. To quantify this critical parameter the so called snow bulk density ρ_s is introduced: According to Brandes et al. (2007) ρ_s is defined as the increase of mass during a certain time interval divided by the sum of all snow flake volumes measured with the 2DVD in

the same time interval. It is a common assumption that the density of snow flakes depends on their size D (Fabry and Szyrmer, 1999; Heymsfield et al., 2004; Brandes et al., 2007). In the present work the size density relation from Brandes et al. (2007) is used to derive water equivalent precipitation rates for snowfall events:

$$\rho_s(D) = 0.178 D^{-0.922} \tag{4.5}$$

In Brandes et al. (2007) D is the median diameter of the snow flakes. The density of single solid hydrometeors also depends on the surface structure and on the degree of riming of the snow flakes. The higher the degree of riming, the larger is the equivalent amount of water contained in the snow flake volume and the higher is the snow density. Measuring the snow flake volume with the 2DVD and the increase of mass with a weighing precipitation sensor simultaneously can deliver information on the dominant degree of riming in an ensemble of snow flakes. For validation of the classification of the degree of riming a weighing precipitation sensor (OTT Pluvio^2, version 200) was placed right under the sensitive area of the 2DVD (see Fig. 4.1). The measured bulk densities were compared to those found by Locatelli and Hobbs (1974) for graupel and other types of hydrometeors.

Table 4.4: For 38 one-minute events of snowfall the degree of riming and the dominating crystal type was visually identified on site. The last column shows the result of the single picture classification: c = complex crystals, s = single crystals, p = pellets (see also Fig.4.8).

#	Time (UTC)	on site observation		Class
		Riming	Dominating crystal type	
1	2013/11/28-12:00	moderate	large crystals, dendrites	c
2	2014/01/13-20:25	weak	very small, fine crystals	c
3	2014/01/14-10:20	moderate	irregular structure	c
4	2014/01/14-20:54	strong	small pellets	p
5	2014/01/20-11:22	weak	small flakes, irregular structure	c
6	2014/01/23-14:12	strong	irregular structure	c
7	2014/01/23-16:17	strong	many single crystals, dendrites	s
8	2014/01/23-20:00	strong	jumping pellets	p
9	2014/01/24-04:46	moderate	small crystals, some dendrites	s
10	2014/01/24-05:27	strong	large flakes	c
11	2014/01/24-06:51	strong	flakes with irregular structure	c
12	2014/01/24-11:18	weak	small flakes, dendrites sticking together	c
13	2014/01/24-11:42	weak	mixture of dendrites and needles	c
14	2014/02/13-18:28	strong	flakes with irregular structure	c
15	2014/02/13-19:35	strong	flakes with irregular structure	c
16	2014/02/13-21:35	strong	small, fine crystals	s
17	2014/02/13-22:56	strong	irregular structure	c
18	2014/02/19-04:41	moderate	small crystals, dendrites, branches	s
19	2014/02/19-09:13	moderate	flakes, some large dendrites	c
20	2014/02/19-09:59	moderate	large flakes, some dendrites	c
21	2014/02/19-10:51	strong	jumping pellets	p
22	2014/02/19-11:01	moderate	irregular structure	c
23	2014/02/19-11:14	strong	small crystals	s
24	2014/02/19-12:44	moderate	irregular structure, large flakes	c
25	2014/02/19-15:07	moderate	flakes, dendrites	c
26	2014/02/19-17:54	strong	flakes with irregular structure	c
27	2014/02/19-20:51	strong	harsh pellets	p
28	2014/05/14-15:07	strong	small pellets	p
29	2014/05/14-17:25	strong	irregular structure	p
30	2014/05/14-20:07	strong	irregular structure	p
31	2014/05/14-22:25	strong	jumping pellets	p
32	2014/05/15-06:19	strong	irregular structure	p
33	2014/05/15-08:13	strong	irregular structure	p
34	2014/05/15-11:04	strong	pellets	p
35	2014/05/15-13:42	strong	pellets	p
36	2014/05/15-16:29	strong	small pellets	p
37	2014/05/15-16:51	strong	small pellets	p
38	2014/05/15-21:02	strong	irregular structure	p

4.2 Aerosol characterization and calculation of scavenging coefficients

4.2.1 Measurement of aerosol particle size distribution

To calculate size dependent scavenging coefficients, aerosol particle size distributions must be measured in consecutive time intervals. In this study aerosol particle size distributions were monitored using the well-established differential mobility analyzer technique: A Scanning Mobility Particle Sizer (SMPS, model 3080 by TSI, USA) in combination with a Condensation Particle Counter (CPC, model 3010, by TSI, USA) measures the aerosol particle size distribution from 10 nm to 510 nm in 36 size classes. The SMPS delivers a size spectrum every 10 to 12 minutes.
The inlet system of the SMPS is called whole air inlet. This means that the aerosol is sampled without a preimpactor inlet head. The inlet head and the outer part of the inlet pipe are heated and kept at a constant temperature of approximately 20°C.
Calibration and quality assurance measurements are performed regularly with the whole SMPS measurement system. At weekdays the system undergoes a check for function and operation parameters with an additional weekly check of selected flow parameters. On a monthly basis a more extended check with flow calibration and a standard consisting of a dilution of 200 nm latex particles is performed. On an annual basis the SMPS instrumentation is checked with a standard which has been prepared and tested centrally at the TROPOS institute for tropospheric research. At least every two years the whole set of instruments is brought to the TROPOS Institute in Leipzig and checked thoroughly in a round robin together with other instruments from other European institutes. The SMPS measurement system used for this study is part of the German contribution to the World Meteorologic Organization Global Atmosphere Watch program (WMO/GAW, 2007). Therefore, it meets the instrumental standards required by this network (WMO/GAW, 2003). The relative uncertainty for the whole system was determined to be ±5% for the concentration measurements. The SMPS-data used in this study was kindly provided by the German Federal Environment Agency.

4.2.2 Measurement of activity size distribution

Scavenging coefficients generally depend on aerosol particle size. The radionuclides analyzed in this study, ^{7}Be, ^{137}Cs and ^{210}Pb, are bound to aerosol particles, and therefore, their atmospheric activity is associated with the

aerosol particle size distribution. The distribution of atmospheric activity with aerosol particle size is called activity size distribution. To analyze the washout efficiency for the mentioned particle bound radionuclides, the activity size distribution is an important parameter.
In the present work, activity size distributions were measured using an Electric Low Pressure Impactor (ELPI+ by Dekati, Finland), which is a cascade impactor consisting of 14 impactor stages and one filter stage (Marjamäki et al., 2000). The ELPI classifies aerosol particles in 15 size classes from 0.006 μm to 10 μm according to their aerodynamic diameter. Particles with diameters between 0.006 μm and 0.017 μm are detected in a filter stage. The aerosol particles are collected inside the impactor on sample substrates that can be analyzed further. For this study the ELPI impactor stages were equipped with removable aluminum foils of approximately 2.5 cm diameter on which the aerosol particles were collected (Fig. 4.9 a). When the aluminum foils are removed from the impactor after a certain sampling period, a size-resolved aerosol particle sample is obtained. Only the 14 impactor stages can be used for further analysis. From the filter stage no sample is available. To collect a sufficient number of aerosol particles for further analysis by gamma spectrometry, given the relatively low sampling flow of 0.6 m^3h^{-1}, the sampling period for the activity size distribution measurements was three to four weeks.

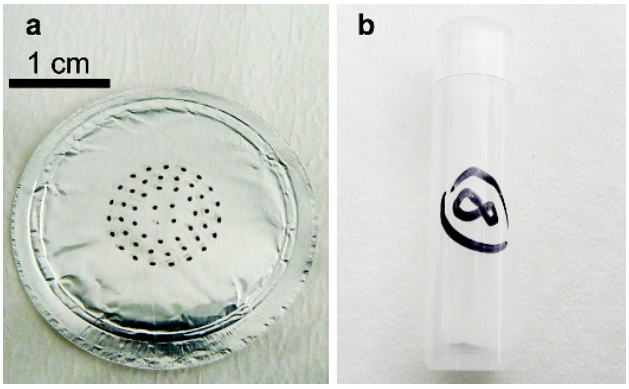

Figure 4.9: ELPI impactor stage number 8 equipped with a removable aluminum foil on which the aerosol particles are collected (a). The aluminum foil was then folded and placed inside a calibrated geometry for gamma spectrometry (b). The folded aluminum foil can be seen at the bottom of the vessel.

The size-resolved aerosol particle samples were further analyzed by means of gamma spectrometry, for the activity of the radionuclides ^{7}Be, ^{137}Cs and ^{210}Pb. For this, the aluminum foils with the aerosol particles were first folded

in a way that minimizes particle loss during the folding procedure. The folded foils were stored inside a vessel for gamma spectrometry measurement (Fig. 4.9 b).
Two different well calibrated p-type detectors with an energy range from 20 keV to 2000 keV were used for gamma spectrometry analysis of the aerosol particle samples. The detectors have a relative efficiency of 20.9% (30%) and an energy resolution (FWHM) of 2.02 keV (1.96 keV) for ^{60}Co (1330 keV). Quality assurance measurements of background and certified multi-nuclide standard materials (by Eckert und Ziegler Nuclitec GmbH, Germany) containing 11 different radionuclides in the energy range of 40 keV to 2000 keV were repeated every month. Most samples were measured for a time period of 14 days. Some measurements were stopped earlier, however, when the relative uncertainty of the ^{7}Be measurement was below 10%.

4.2.3 Measurement of atmospheric activity concentrations

To investigate the activity washout efficiency (i.e., the scavenging coefficient for the particle bound radionuclides) for ^{7}Be, ^{137}Cs and ^{210}Pb, consecutive measurements of the atmospheric activity concentration are necessary. In this study the activity concentration of the mentioned radionuclides was measured the following way: Bulk aerosol samples were taken with a high-volume Aerosol Sampling Station ASS1000 (by Fischer PTI, Germany, see Fig. 4.10 a). The ASS1000 generates a sample air stream of 700 m^3h^{-1} to 1100 m^3h^{-1} depending on the elapsed sampling time. The aerosol particles are collected in a polypropylene (Type G-3) filter (Fig. 4.10 b) with the following filter efficiencies for the radionuclides under investigation (Arnold et al., 2000):

^{7}Be: 96.4%, ^{137}Cs: 99.9%, ^{210}Pb: 93.1%

To perform consecutive measurements of the activity concentration, the filter was changed approximately every two hours during a precipitation event. Each filter containing the number of aerosol particles sampled in this two-hour interval was pressed to a geometry calibrated for analysis with gamma spectrometry (Fig. 4.10 c).
One n-type and six different p-type detectors with a measurement range from 20 keV to 2000 keV were used for gamma spectrometry analysis of the filter samples. The detectors have a relative efficiency of 26.3% to 90% and an energy resolution (FWHM) of 1.78 keV to 1.99 keV for ^{60}Co (1330 keV). The detectors were calibrated for the efficiency of the pressed filter geometry with a certfied liquid multi-nuclide standard material. For each measurement self

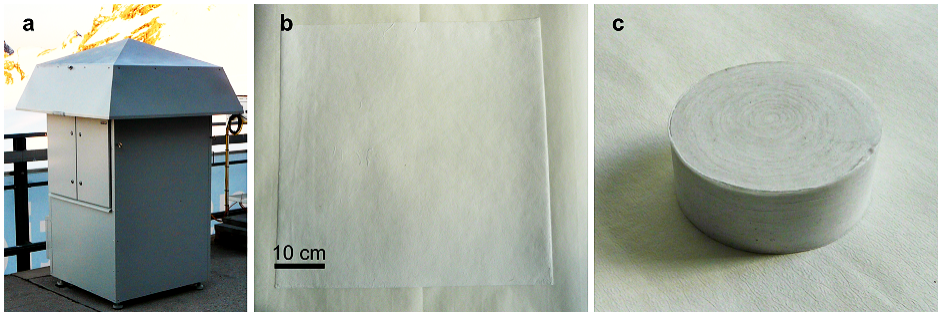

Figure 4.10: High volume Aerosol Sampling Station ASS1000 (a) installed to take bulk aerosol samples on a polypropylene (Type G-3) filter (b). The filter was pressed to a geometry calibrated for analysis with gamma spectrometry (c).

absorption correction, especially for the evaluation of ^{210}Pb, was performed. Quality assurance measurements concerning background, accuracy and reproducibility with certified multi-nuclide standard materials (by Eckert und Ziegler Nuclitec GmbH, Germany) containing 11 different radionuclides in the energy range of 40 keV to 2000 keV were repeated every month. All samples were measured in a time period of 14 days. The spectra were analyzed for the radionuclides ^{7}Be, ^{137}Cs and ^{210}Pb integrating the counts of the peak net area at the energies as summarized in Tab. 4.5 (Wahl, 2007).

Table 4.5: Emitted gamma ray energies of the analyzed radionuclides (Wahl, 2007).

Nuclide	^{7}Be	^{137}Cs	^{210}Pb
Energy [keV]	477.6	661.7	46.5

4.2.4 Data selection procedure

In this study, any change of aerosol particle concentration caused by precipitation is quantified. In general the following equation describes the change of aerosol particle concentration c for a certain aerosol particle size class in the atmosphere:

$$\frac{dc}{dt} = -\left(\frac{dc}{dt}\right)_{precip} \pm \left(\frac{dc}{dt}\right)_{inst} \pm \left(\frac{dc}{dt}\right)_{turb} \pm \left(\frac{dc}{dt}\right)_{adv} \pm \left(\frac{dc}{dt}\right)_{hygr} \pm \left(\frac{dc}{dt}\right)_{cond} \pm \left(\frac{dc}{dt}\right)_{coag} + \left(\frac{dc}{dt}\right)_{nucl} \tag{4.6}$$

The primary process for aerosol particle generation from the gas phase is nucleation (*nucl*). In the lower troposphere nucleation is a photochemically driven process which is most efficient during times with strong solar irradiation (Birmili and Wiedensohler, 2000). The most important reaction leading to nucleation is the photochemical oxidation of sulfur dioxide to sulfuric acid and sulfate (Roedel, 2000). On Mt. Zugspitze the permanent occurrence of nucleation mode particles (particles with diameters below 30 nm), whatever season or daytime, is a strong indicator that up to now unknown sources of nucleation are active in this region (Birmili et al., 2007).
Nucleation mode particles grow through coagulation (*coag*) to larger particles. The permanent presence of nucleation mode particles leads to a permanent variation of particle concentration through coagulation.
Particle growth by condensation (*cond*) occurs when the atmosphere is supersaturated with water vapor. Heating the inlet system for aerosol particle concentration measurements to a constant temperature of approximately 20°C together with the very low temperatures on Mt. Zugspitze (5.1°C in summer and −7.1°C in winter in average over the measurement period) guaranties that the humidity of the sample air containing the measured aerosol is below water vapor saturation, and particle growth due to condensation does not occur.
Aerosol particles consisting of hygroscopic compounds can grow by adsorbing or absorbing water molecules from their surrounding. This process is called hygroscopic growth (*hygr*) and depends strongly on the relative humidity of the surrounding air. Hygroscopic growth of aerosol particles can be excluded as a reason for any change in aerosol particle size distribution by selecting only events with a minimum change in relative humidity (Volken and Schumann, 1993; Laakso et al., 2003; Kyrö et al., 2009).
Turbulent mixing (*turb*) close to the boundary of two air masses with different aerosol loading (Volken and Schumann, 1993) can cause changes in the aerosol particle concentration. Replacing the initial air mass by another air mass in a passage of a frontal zone is called advection (*adv*) and is also a reason for aerosol particle concentration changes. These phenomena can

Table 4.6: For a period to be considered as stable the following criteria for the variation of meteorological parameters were chosen (from Kyrö et al. (2009)).

meteorological parameter	maximum accepted mean variation
temperature	$\pm 3°C$
pressure	$\pm 5\,hPa$
wind speed	$\pm 3\,ms^{-1}$
wind direction	$\pm 50°$
rel. humidity	$\pm 5\%$

be identified with rapidly changing meteorological conditions like temperature, pressure, wind speed and wind direction (Volken and Schumann, 1993; Laakso et al., 2003). Excluding all events with strongly changing meteorological conditions avoids biasing the measurements with variations in aerosol particle concentration due to turbulent mixing and advection.
A small bias caused by undiscovered instrumental uncertainties (*inst*) of random as well as systematic nature can not be avoided and contribute to the uncertainty of the results obtained in this study. The instrumental uncertainty of the SMPS-measurement system is kept as low as possible by performing regular calibration and quality assurance measurements (see section 4.2.1).
For a reliable observation of any change in aerosol particle concentration through precipitation it must be guaranteed that the effects of nucleation, coagulation, condensation, hygroscopic growth, turbulence and advection only play a minor role. For that reason a very strict data selection was applied in this study:
In a first step only precipitation events lasting at least 30 minutes with precipitation rates of more than $0.1\,mmh^{-1}$ were selected. Subsequently, these periods were analyzed according to their meteorological stability. The conditions for a period to be considered as stable are the same as those in Kyrö et al. (2009), and similar to those proposed by Laakso et al. (2003) and Paramonov et al. (2011) (Tab. 4.6). This procedure guarantees that the effects of advection, turbulent mixing and hygroscopic growth are minimized. Additionally, because of bad 2DVD performance at high wind velocities (Nešpor et al., 2000), data analysis was restricted to periods with mean wind velocities of less than $5.0\,ms^{-1}$. The meteorological data used in this study was kindly provided by the *Deutscher Wetterdienst*.
After applying the criteria given in Tab. 4.6 it is assumed that the primary sink for the aerosol particle concentration during a precipitation event is the process of washout. However, also rising aerosol particle concentrations were

detected during precipitation events. One reason for this is the variation due to instrumental uncertainties. In addition it seams that nucleation and coagulation processes can also not be excluded although the criteria in Tab. 4.6 were applied. Therefore data indicating rising aerosol particle concentration beyond the instrumental uncertainty was excluded from the analysis. Fig 4.11 illustrates this selection schematically. The instrumental uncertainty of the aerosol particle concentration measurement was determined in several calibration procedures conducted in the framework of the Global Atmosphere Watch program (WMO/GAW, 2003). The relative uncertainty of the whole particle number concentration measurement is ±5%.

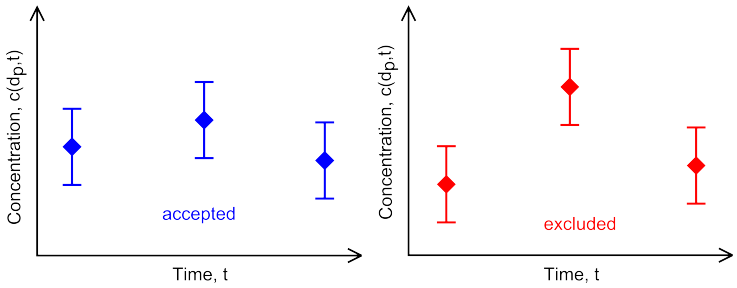

Figure 4.11: Schematic illustration of an accepted and an excluded time series of concentration measurements.

4.2.5 Calculation of scavenging coefficients

For this work scavenging coefficients for different types of precipitation events were calculated. The aerosol particle concentration $c(d_p, t)$ is a function of the aerosol particle diameter d_p and time t. Under the assumption that precipitation scavenging is the dominant sink for $c(d_p, t)$ Eq. (4.6) can be written as a first order decay equation

$$\frac{dc(d_p, t)}{dt} = -\lambda(d_p)c(d_p, t). \tag{4.7}$$

Integrating Eq. (4.7) yields the scavenging coefficient $\lambda(d_p)$:

$$\lambda(d_p) = -\frac{1}{t_1 - t_0} \ln\left(\frac{c(d_p, t_1)}{c(d_p, t_0)}\right). \tag{4.8}$$

One possibility to calculate the scavenging coefficient is using Eq. (4.8) and measuring the aerosol particle size distribution at times t_0 and t_1 (Laakso et al., 2003; Kyrö et al., 2009; Paramonov et al., 2011). If more than two consecutive measurements of the aerosol particle size distribution exist for

one precipitation event, scavenging coefficients can be calculated in another way. Rearranging Eq. (4.8) to

$$\ln\left(c(d_p,t)\right) = -\lambda(d_p)t + \ln\left(c(d_p,0)\right) \tag{4.9}$$

shows that $\lambda(d_p)$ is the slope of a linear fit to the logarithm of the aerosol particle concentration. The linear fit method has the advantage of minimizing the effects of instrumental noise (Volken and Schumann, 1993; Kyrö et al., 2009).

In this work the linear fit method was applied. Separately for each aerosol particle size bin, a least squares fit was performed to the logarithms of three consecutive measurements of the aerosol particle concentration which were made during selected precipitation events (the data selection procedure is described in chapter 4.2.4). Depending on the sampling interval of the Scanning Mobility Particle Sizer (SMPS) of 10 min to 12 min each scavenging coefficient represents an average value over 30 min to 36 min. The average interval was chosen as short as possible, to minimize the effect of mixing different hydrometeor types that might have occurred in one event.

Chapter 5

Results

5.1 Performance of the 2D-Video Disdrometer

5.1.1 Calibration with solid steel spheres

A very important part of the present work is the characterization and classification of precipitation events with a 2D-Video Disdrometer which was adapted for the detection of solid and mixed phase hydrometeors.
The calibration experiment for the height and width measurements with solid spheres shows that both the mean height and the width were overestimated constantly (Fig. 5.1, left panel). As summarized in Tab. 5.1 the overestimation ranges from 0.35 mm to 0.38 mm.

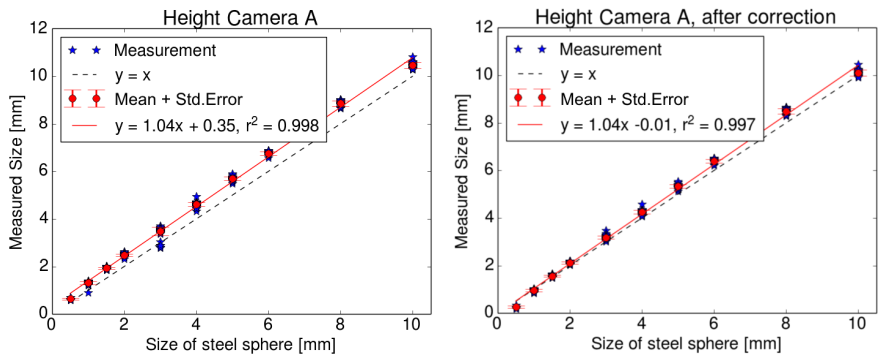

Figure 5.1: Comparison between nominal and measured height of calibration spheres before and after correcting the pixel width.

Table 5.1: Results of the calibration measurements with solid spheres. m and t denote the slope and intercept of the regression line, respectively. r is the correlation coefficient. H_A, H_B, W_A and W_B denote the height and width measured with camera A and B.

	m	t	r^2
H_A	1.04	0.35	0.998
H_B	1.03	0.38	0.998
W_A	1.04	0.35	0.998
W_B	1.03	0.37	0.998

The right panel in Fig. 5.1 shows the results of the size measurements after implementing the following equation as a correction of the pixel width p:

$$p = p(x, y) \cdot f_{corr} - t/n_{pix} \tag{5.1}$$

$p(x, y)$ denotes the pixel width at the (x, y) location where the sphere hit the sensitive area, f_{corr} is the correction factor supplied by the manufacturer and n_{pix} is the number of shaded pixels. The correction factor t can be found in Tab. 5.1 for the specific dimension. The result of this correction is that there is good agreement between measured and nominal dimensions.

5.1.2 Measurement ranges and uncertainties for solid spheres

For the experiments with solid spheres the relative standard deviation for each parameter (chapter 4.1.1.3 a to g) can be calculated (Fig. 5.2). It varies for the elongation, roundness and shape factor in camera A from 14% for spheres with a diameter of 0.5 mm to 1.7% for spheres with a diameter of 10 mm. In camera B it varies from 6% to 2%. The height and width can be measured with a relative standard deviation between 18% for small particles and 1.8% for larger ones in both cameras. The relative standard deviation for equivalent diameter and volume varies from 7% to 1.5% and from 22% to 5%, respectively. For the vertical velocity it stays below 1.5% in the observed size range.

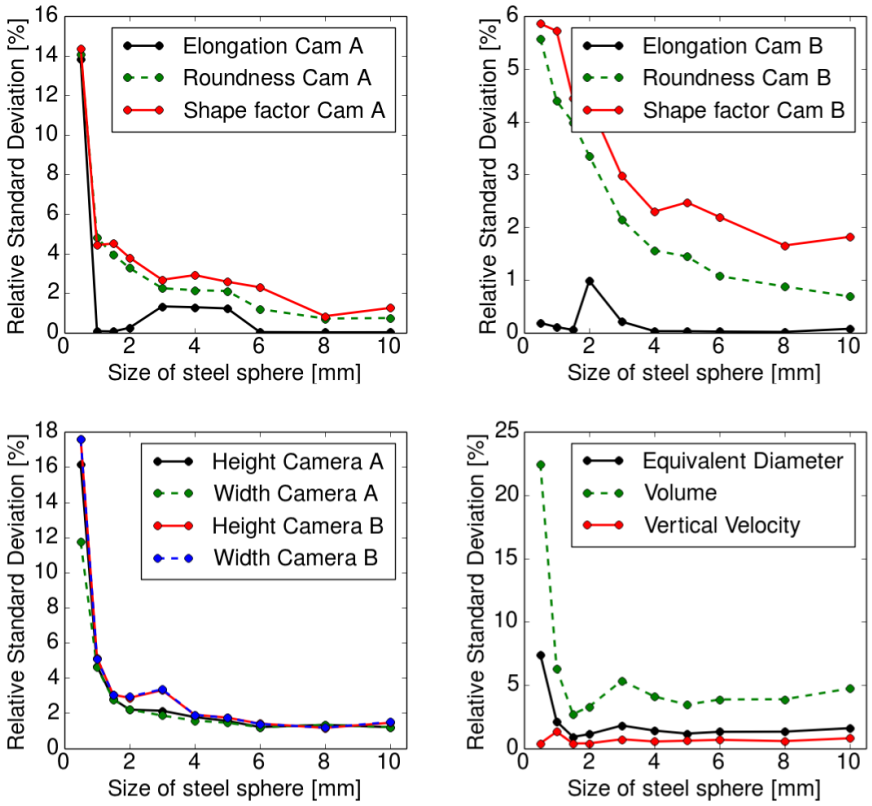

Figure 5.2: The relative standard deviation for the different quantities measured with solid spheres.

An important parameter for the whole data analysis procedure is the spatial resolution or the width of a single pixel. Depending on the x and y coordinate of the hydrometeor in the measuring plane (see Fig. 4.3) for the instrument used in this study, the single pixel width varies from 0.15 mm to 0.25 mm.

5.1.3 Validation of 2DVD measurements

The measurement results with the solid spheres reveal how well shape, size and velocity information gained with 2DVD measurements reproduce the nominal values.

a) The 2DVD measures **elongations** very close to $E = 1$ (Fig. 5.3 a and b). At 0.5 mm, 2 mm, 3 mm, 4 mm and 5 mm outliers can be identified.

b) The measured **roundness** values are very close to $R = 1$. The spread of the single measurements increases for smaller spheres (Fig. 5.3 c and d).

c) Fig. 5.3 e and f show the **shape factors** measured for the calibration spheres. They are between 0.6 and 0.7. Using a blurring edge filter that spreads over 20 pixels before detecting the perimeter of the object, values between 0.90 and 0.95 are measured (Fig. 5.3 g and h).

d) The slope m and intercept t for the linear regression line between nominal and measured **maximum dimension** are $m = 1.04$ and $t = -0.01$ (Fig. 5.1).

e) **Equivalent diameters** (Fig. 5.4 a) and

f) **volumes** are reproduced very well in 2DVD measurements (Fig. 5.4 b).

g) Measurements of the **fall velocity** show a very low spread around the theoretically predicted values (Fig. 5.4 c).

Testing the new matching algorithm with an ensemble of styrofoam particles showed that the velocities measured in the ensemble, where all the particles were released at the same time from the same height, have a very low spread around the single measurements, when the particles were released one after the other (Fig. 5.5). The measured velocities are between $2.0\,\mathrm{ms}^{-1}$ and $2.9\,\mathrm{ms}^{-1}$. Out of 30 detected particles only for the size between 8 mm and 9 mm one outlier has been detected.
Analyzing the original matching result for a real snow fall event on the contribution of hydrometeors with unreasonable geometry and velocity yields that the original data set contains 41% of particles with a maximum dimension above the mean spacial resolution of 0.2 mm, 20% of particles that additionally pass the geometry filter, 32% of particles with velocities between $0.5\,\mathrm{ms}^{-1}$ and $6.0\,\mathrm{ms}^{-1}$ and only 25% of particles with velocities lower than the velocity a raindrop with the same maximum dimension would have. Finally 9% of hydrometeors fulfill the criterion that the height measured in camera A is not more than 20% different to the height measured in camera B (Tab. 5.2).

Table 5.2: Contribution of detected hydrometeors after applying the original matching algorithm. D is the maximum dimension, v the vertical velocity and $H_{A/B}$ and $W_{A/B}$ are the width and height measured in camera A and B.

Filter type	Remaining number of flakes	%
Total (no filter)	439072	100
$D > 0.2$ mm (spatial resolution, sr)	178949	40.8
sr + Velocity: 0.5 $\text{ms}^{-1} < v < 6.0$ ms^{-1}	142299	32.4
sr + Velocity: $v(D) < v_{Rain}(D)$	111896	25.5
sr + Geometry: $0.1 < H/W < 10.0$ $0.1 < W_A/W_B < 10.0$	86185	19.6
sr + $H_A - H_B < 0.2 H_{max}$	38677	8.8

Figs. 5.6 a to c summarize the performance evaluation in case of real solid phase precipitation. The measured mean shape parameters show the following correlations: Higher elongation means lower roundness and shape factor. Lower elongation means higher roundness and shape factor. Intervals with lower roundness also have lower shape factors and vice versa.

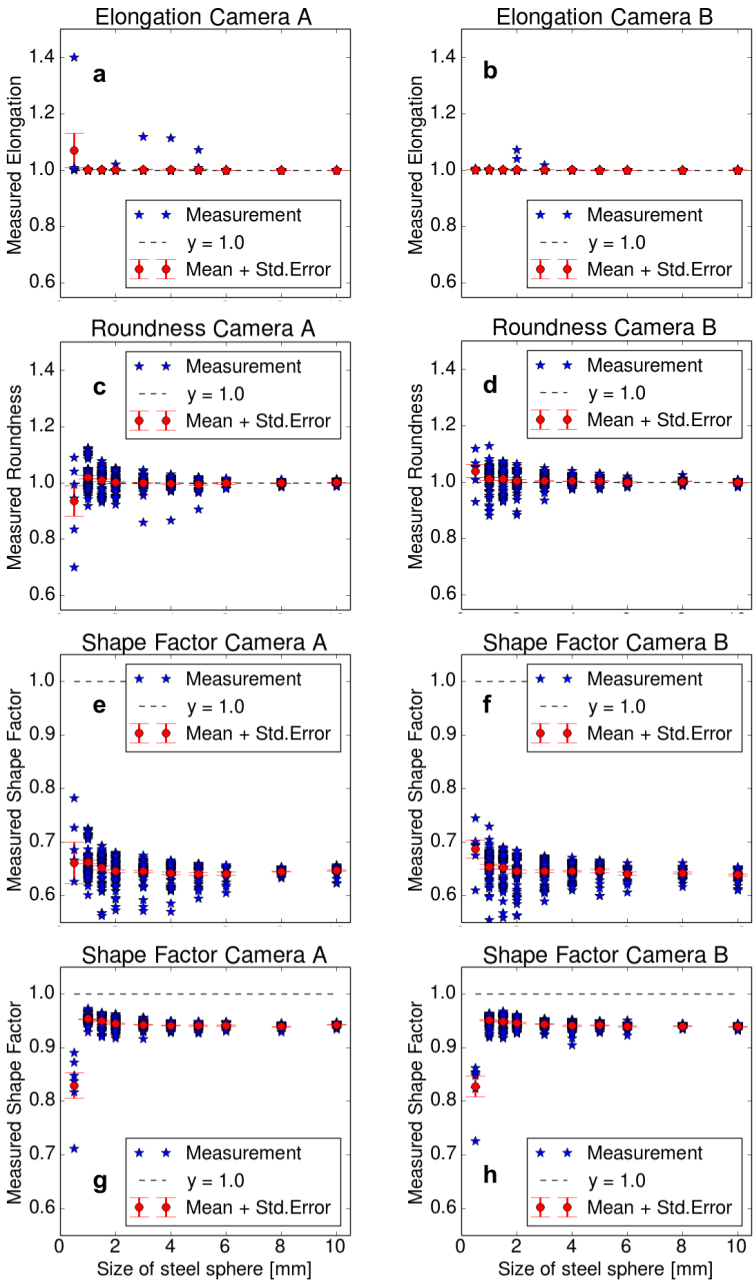

Figure 5.3: Comparison between measured and expected values for the shape parameters. Elongation (a and b), roundness (c and d), shape factor with (g and h) and without (e and f) treatment with a blurring edge filter. Relative standard deviations can be accessed in Fig. 5.2.

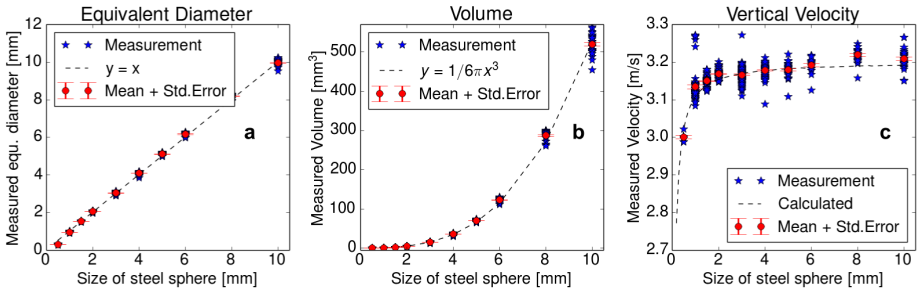

Figure 5.4: Comparison between measured and expected values for equivalent diameter (a), volume (b) and vertical velocity (c). Relative standard deviations can be accessed in Fig. 5.2.

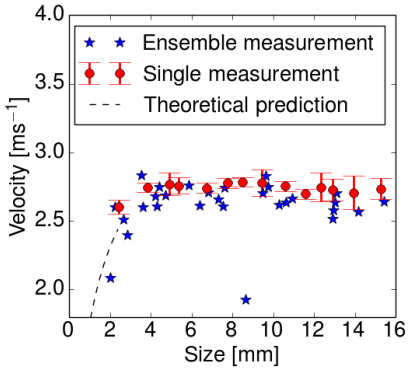

Figure 5.5: Comparison of velocity measurements of single styrofoam objects (dropped one after the other) and of the whole ensemble (all particles dropped at the same time from the same height). Relative standard deviations can be accessed in Fig. 5.2.

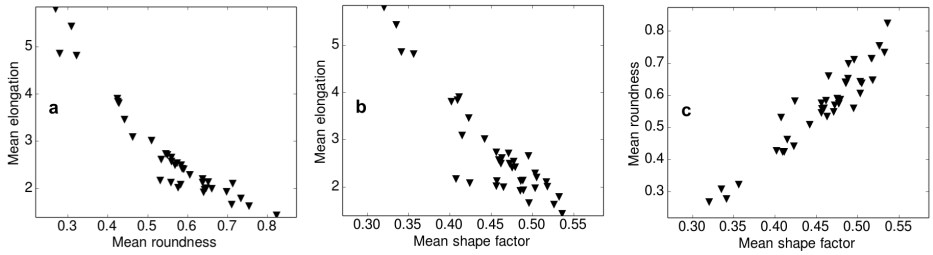

Figure 5.6: Comparison between mean shape parameters measured for real snowflakes. Higher elongation means lower roundness (a) and lower shape factor (b), lower roundness means lower shape factor (c) (and vice versa). Relative standard deviations can be accessed in Fig. 5.2.

5.2 Precipitation event classification

5.2.1 Definition of the solid phase hydrometeor classes

On-site observations allowed to clearly subdivide the hydrometeors into three classes of riming (Tabs. 4.2 and 4.4 3^{rd} column): Hydrometeors were classified as weakly rimed when only a few cloud droplets were observed on their surface. Moderately rimed hydrometeors had half or more of their surface covered with cloud droplets. Finally, when the total hydrometeor surface was covered with one ore more layers of droplets it was concluded that riming was strong.
In the 2DVD measurements the parameter that reflects the degree of riming is the vertical fall velocity and the power law fit parameter β. Fig. 5.7 shows power law fits to size velocity distributions for three events with diffenent degrees of riming: On 24^{th} of January 2014 at 11:18 UTC, for example, weakly rimed hydrometeors were observed (see Tab. 4.4). The size velocity distribution measured for this event shows many hydrometeors larger than 2 mm with velocities lower than $1.5\,\mathrm{ms}^{-1}$. With a value of 0.27 the fit parameter β shows a large curvature of the fitted power function. In contrast, on 19^{th} of February 2014 at 09:13 UTC moderately rimed hydrometeors were observed (see Tab. 4.4). The size velocity distribution suggests many large hydrometeors that reach velocities up to $2.0\,\mathrm{ms}^{-1}$. With a value of 0.40 the fit parameter β shows a lower curvature of the fitted power function than in the previous case. Finally, on 15^{th} of May 2014 at 13:42 UTC, for example, strongly rimed hydrometeors were observed (see Tab. 4.4). In this case the size velocity distribution suggests that only few hydrometeors are larger than 4 mm but reach velocities larger than $4.0\,\mathrm{ms}^{-1}$. With a value of 0.65 the fit parameter β shows a very low curvature of the fitted power function. The size velocity diagrams are shown in Fig. 5.7.
The observed solid phase precipitation events were subdivided into three classes of crystal type (Tab. 4.3). It is obvious that the crystal types *complex crystals*, *single crystals* and *pellets* only reflect a coarse classification of crystal types occurring in nature. Important for the presented classification algorithm is the visual classification of every single picture recorded by the 2D-Video Disdrometer (2DVD), and a clear visual identification of the crystal type shown in the 2DVD picture could only be established for these three classes (see Fig. 4.8). For single pictures detailed features such as dendritic, plate-like or column-like structures, could be identified. Whether or not such detailed features can be identified strongly depends on the orientation of the hydrometeor to the camera. Note that the spatial resolution of the 2DVD is too low to identify these features reliably. Therefore, in the present work the

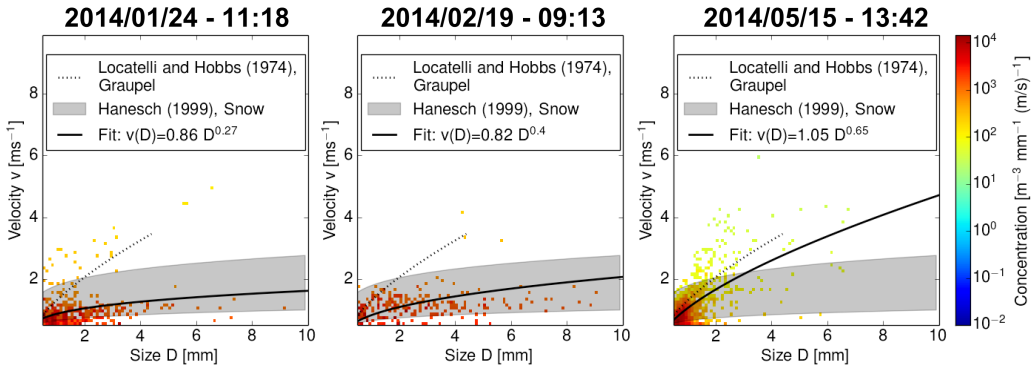

Figure 5.7: Size velocity relations for solid phase precipitation events with different degrees of riming. On 24^{th} of January 2014 at 11:18 UTC hydrometeors were weakly rimed. On 19^{th} of February 2014 at 09:13 UTC hydrometeors were moderately rimed. On 15^{th} of May 2014 at 13:42 UTC hydrometeors were strongly rimed.

classification of solid hydrometeors includes only three classes.
The set of 38 well observed one-minute events of solid precipitation shown in Tab. 4.4 serves to define conditions for the parameters β, R and S that have to be fulfilled when a one-minute event is labeled with a certain class of dominating degree of riming and crystal type. The results of the on-site observations and the visual picture classification are summarized in Tab. 4.4. The picture classification was always confirmed by two independent observers. All in all, the on-site observations and the picture classification match very well. Only on 14^{th} and 15^{th} of May, 2014 the observations do not match in 5 cases. These were excluded from further analysis. Plotting the mean values of the shape parameters against the fit parameter β, events with different crystal type classes and different riming regimes appear in different regions of the diagram. Fig. 5.8 shows $\beta - R$ and $\beta - S$ plots for the 33 remaining events. The following regions can be identified for the different degrees of riming and crystal types: For $\beta < 0.3$, weakly rimed hydrometeors were observed. For events consisting of moderately rimed hydrometeors, β is between 0.3 and 0.5, while for events with strong riming and events mainly consisting of pellets have β is larger than 0.5. The shape factor for single crystal events is below 0.35. The shape factor for complex crystals and pellets lays between 0.4 and 0.5. For some pellet events, however, it is even larger than 0.5. A similar behavior can be seen for the mean roundness. The roundness for single crystal events is below 0.3. Between 0.4 and 0.6 mainly complex crystal events can be found. For $R > 0.6$ most of the observed events consist of pellets.

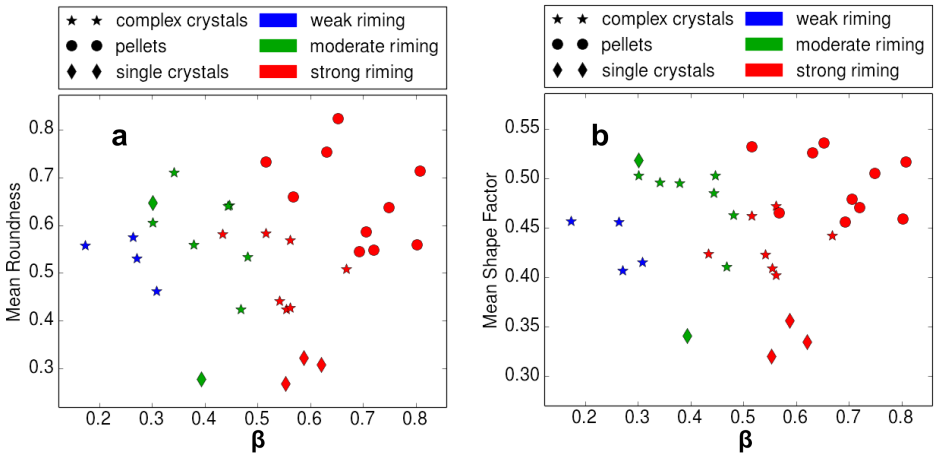

Figure 5.8: $\beta - R$ (a) and $\beta - S$ (b) plot for 33 precisely observed and visually classified one minute intervals. Colors and marker styles represent visual on-site observations. The different degrees of riming and the different crystal type classes clearly appear in different regions of the diagrams. The measurement uncertainty for the fit parameter β is below 6%. For roundness and shape factor, relative standard deviations can be accessed in Fig. 5.2.

From these observations boundary conditions for snow event classification could be defined (Tab. 5.3) that can easily be implemented as a decision tree in an algorithm for automatic classification of solid phase precipitation event.

Table 5.3: The classes of precipitation events.

Crystal type	single crystals (**s**) $S \leq 0.35$ $R \leq 0.4$	pellets (**p**) $S \geq 0.35$ $R \geq 0.4$ $\beta > 0.5$	complex crystals (**c**) $0.35 < S < 0.45$ $0.4 < R < 0.55$	$\Rightarrow$ t
Riming	weak (**1**) $\beta < 0.3$	moderate (**2**) $0.3 \leq \beta < 0.5$	strong (**3**) $\beta \geq 0.5$	$\Rightarrow r$

5.2.2 Validation of the classification

To validate the classification method for solid hydrometeors, an independent data set was compared with the automatic 2DVD classification. For that purpose, eleven events were identified for each crystal type randomly, 33 events in total. For complex crystals and aggregates, eight matches were found. Two events were falsely classified as pellets and one event was falsely

classified as single crystals. For pellets, ten matches were found and only one event was falsely classified as single crystals. For single crystals all eleven events matched. These results are summarized in a consistency matrix (Tab. 5.4) where the correct matches can be found on the diagonal.

Table 5.4: Consistency matrix showing the agreement between the automatic 2DVD classification of solid hydrometeors and the visual picture classification.

		2DVD		
		c	p	s
visual	c	**8**	0	0
	p	2	**10**	0
	s	1	1	**11**

5.2.3 Real case applications

In the following, three examples of real case applications of the automatic solid hydrometeor classification are shown.
In the time period shown in Fig. 5.9 (14^{th} of March 2013 from 17:21 to 21:21 UTC), the observed solid phase precipitation was automatically classified as pellets with a short period at 20:00 UTC which was classified as complex crystals. Until 19:51 UTC the precipitation rate stayed below $1\,\mathrm{mmh}^{-1}$ and increased up to $2.5\,\mathrm{mmh}^{-1}$ until 21:21 UTC. During the whole event the hydrometeors showed strong riming. The mean roundness stayed between 0.6 and 0.8. The maximum dimension stayed mostly below 5 mm and the mean maximum dimension was around 1.5 mm. The temperature stayed around $-20°\mathrm{C}$. The bulk snow density measured with the weighing precipitation gauge varied from $0.05\,\mathrm{gcm}^{-3}$ to $0.4\,\mathrm{gcm}^{-3}$ with a mean of $0.2\,\mathrm{gcm}^{-3}$.
For the period shown in Fig. 5.10, the situation was different. First a short period of complex crystals could be identified. From 19:57 to 20:31 (UTC) precipitation mainly consisted of single crystals. From 20:32 to 21:02 (UTC), the situation was more unstable but a majority of complex crystals could be seen. From 21:03 to 21:50 (UTC) again single crystals predominated. The precipitation rate was between $0.5\,\mathrm{mmh}^{-1}$ and $2.5\,\mathrm{mmh}^{-1}$. The degree of riming varied between moderate and strong. The roundness stayed below 0.6, while for the single crystal periods it even stayed below 0.3. Periods with complex crystals were associated with large maximum dimensions of up to a mean of 3 mm, while lower mean maximum dimensions around 1.5 mm

coincided with single crystal periods. The temperature reached a local maximum for a complex crystal period of $-6.2°C$ and a minimum of $-8.0°C$ for a single crystal period. The mean bulk density of the crystals was determined to $0.02\,\mathrm{gcm}^{-3}$.
In contrast, the event shown in Fig. 5.11 showed a very stable classification. The whole event is classified as a complex crystal event. The precipitation intensity was moderate at the beginning (up to $4.5\,\mathrm{mmh}^{-1}$) and low during the rest of the event. The degree of riming was mostly weak and the roundness stayed around 0.6. The maximum dimension spectrum indicated frequently occurring hydrometeors which were larger than 6 mm. The temperature stayed around 0.0°C. The mean bulk density for this event was $0.1\,\mathrm{gcm}^{-3}$.

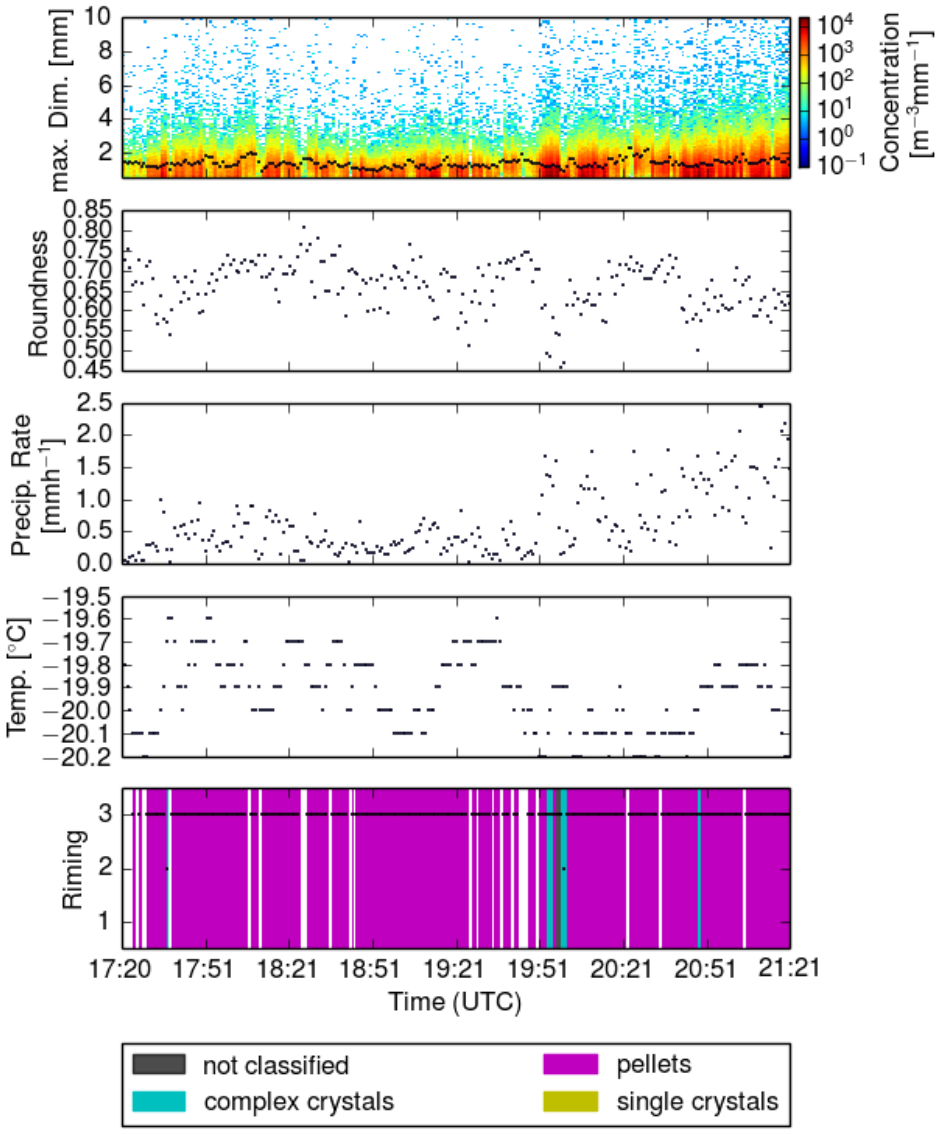

Figure 5.9: Distribution of maximum dimension and mean maximum dimension (dashed line, a), mean roundness (b), precipitation rate (c) temperature (d) and the automatic 2DVD classification (e) for a period of solid phase precipitation on 2013/03/14 from 17:21 to 21:21 UTC. Temperature data was kindly provided by the *Deutscher Wetterdienst*.

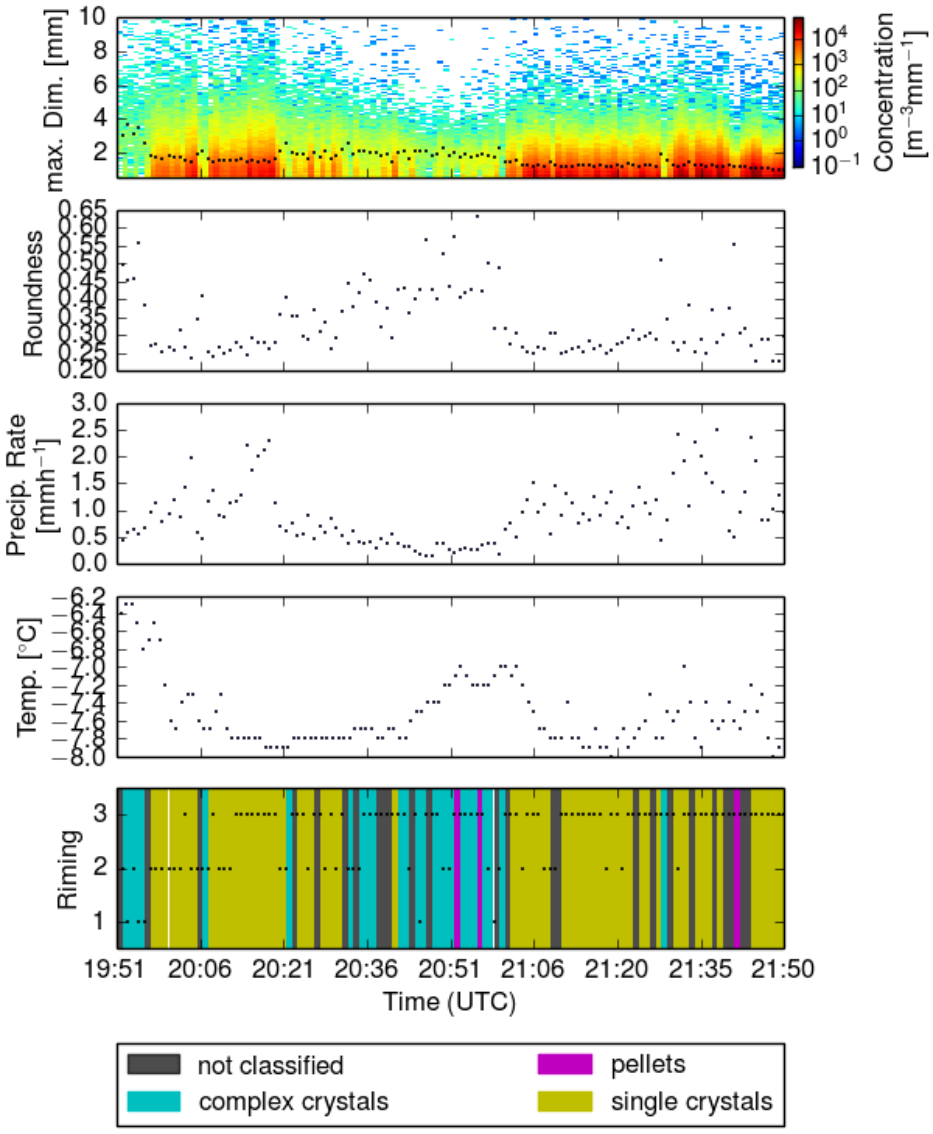

Figure 5.10: Distribution of maximum dimension and mean maximum dimension (dashed line, a), mean roundness (b), precipitation rate (c), temperature (d) and the automatic 2DVD classification (e) for a period of solid phase precipitation on 2013/03/25 from 19:51 to 21:50 (UTC). Temperature data was kindly provided by the *Deutscher Wetterdienst*.

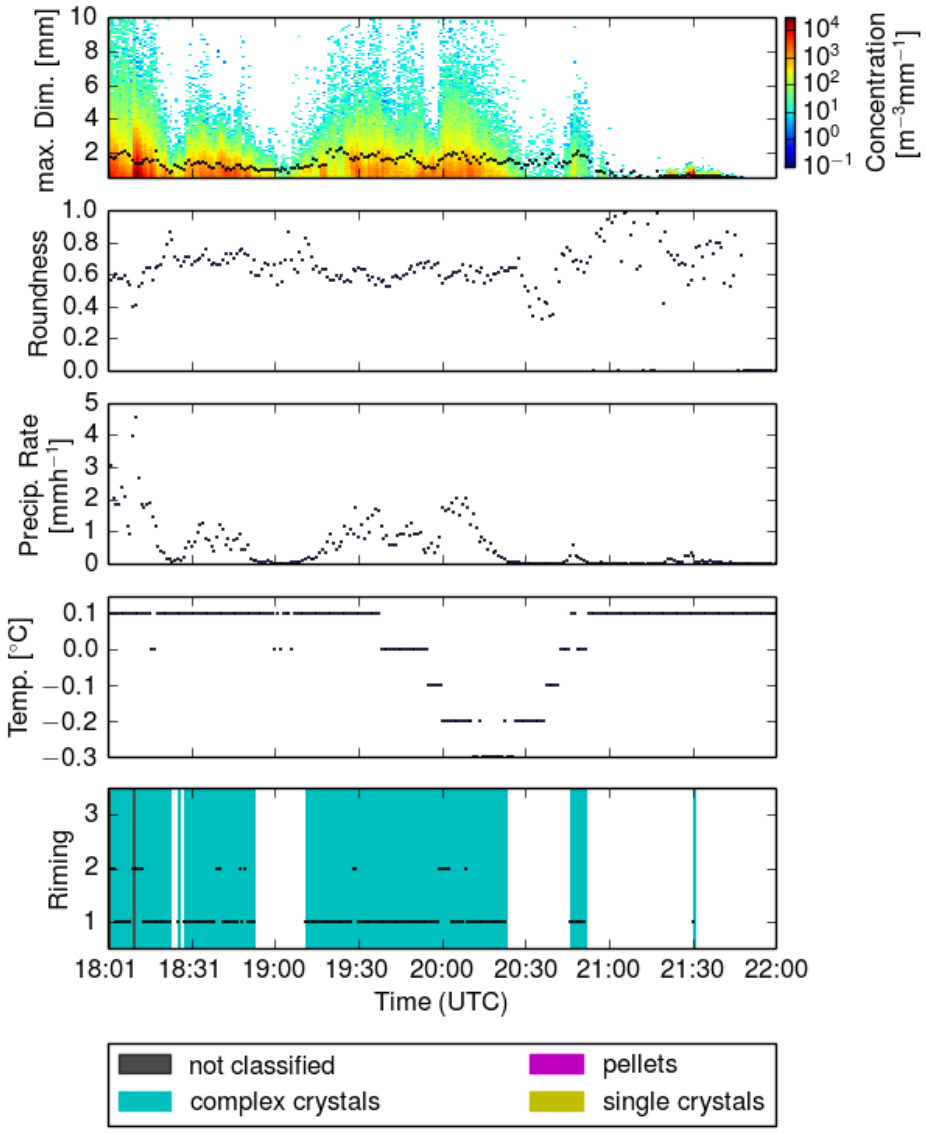

Figure 5.11: Distribution of maximum dimension and mean maximum dimension (dashed line, a), mean roundness (b), precipitation rate (c), temperature (d) and the automatic 2DVD classification (e) for a period of solid phase precipitation on 2013/06/11 from 18:01 to 22:00 (UTC). Temperature data was kindly provided by the *Deutscher Wetterdienst*.

5.3 The basic data set for analysis

To isolate the effect of scavenging as a major sink of aerosol particle concentration in the atmosphere, strict data selection criteria were applied to the total set of recorded precipitation events (see Tab. 4.6). Out of the recorded 4800 hours of precipitation 580 hours (12%) met the criteria for meteorological stability (Tab. 4.6). The remaining data set consisted of 25670 minutes (74%) of solid phase precipitation, 6730 minutes (19%) of mixed phase precipitation and 2280 minutes (7%) of liquid phase precipitation (Fig. 5.12 (a)). In most cases (90%) the water equivalent precipitation intensity was below 2.0 mmh^{-1}. 8% had precipitation intensities between 2.0 mmh^{-1} and 4.0 mmh^{-1}, while for 2% the precipitation intensity was above 4.0 mmh^{-1}.

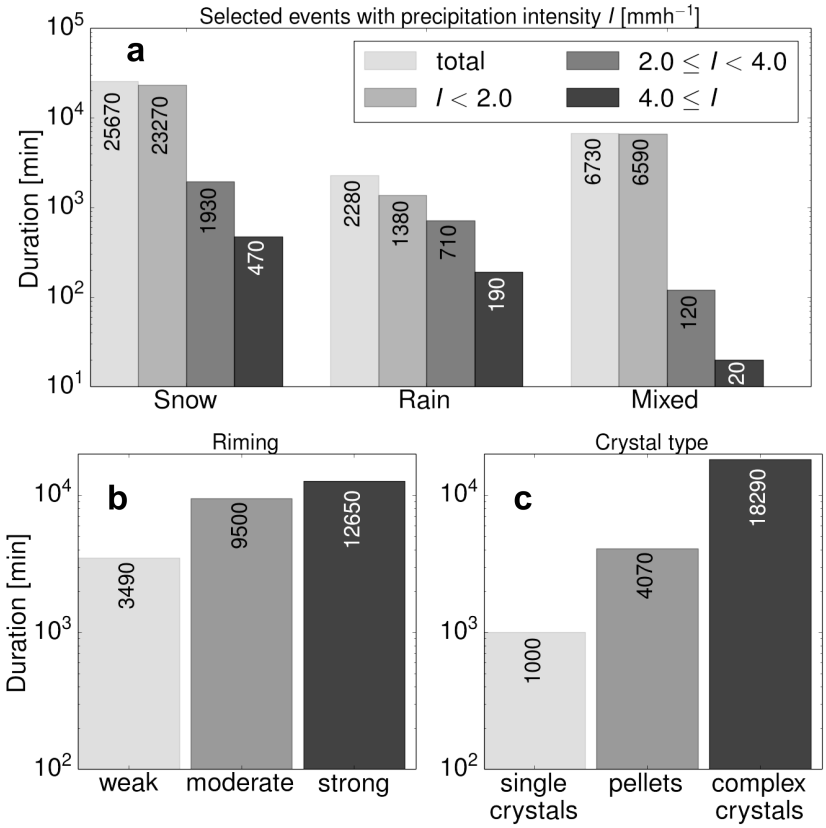

Figure 5.12: Out of the selected events the majority was classified as snow fall events (a). Mixed phase events occurred less frequently. Rain events occurred only rarely. Most snow fall events were classified as strongly rimed (b). The most frequent crystal type were complex crystals (c).

With respect to the degree of riming, 49% of all solid phase precipitation

events were classified as strongly rimed, 37% as moderately rimed and 14% as weakly rimed (Fig. 5.12 (b)). According to the dominating crystal type, 71% consisted mainly of complex crystals, 16% of pellets and 4% of single crystals, while 9% of all selected solid phase precipitation events could not be classified (Fig. 5.12 (c)).
Additionally, all aerosol particle concentration measurements indicating increasing concentration beyond the instrumental uncertainty were excluded (see Fig. 4.11), and only 40% of all aerosol particle concentration measurements passed this criterion.

5.4 Case studies

In this chapter two example measurements are used to further illustrate the data selection criteria. In Figs. 5.13 and 5.14, results of time-resolved particle size distribution measurements (provided by the German Environment Agency) along with those of parallel measurements of the precipitation amount and meteorological parameters (temperature, pressure, relative humidity, wind speed and wind direction measured by the *Deutscher Wetterdienst* (DWD) at the environmental research station Schneefernerhaus) are shown.
On 27^{th} of June 2013 particle concentrations of up to $2000\,\mathrm{cm}^{-3}$ were measured for particle diameters of about 200 nm, from midnight to noon (Fig 5.13 (a)). At 12:20 UTC the onset of significant precipitation was detected. With a short interruption from 13:30 UTC to 13:50 UTC the precipitation event lasted until 15:10 UTC (Fig 5.13 (b)). Due to only slightly varying meteorological conditions the precipitation event was accepted for further analysis (Fig 5.13 (b - d)). Only for the wind direction a few spikes can be identified which were, however, not significant enough to consider the period as unstable. With the onset of precipitation, especially for the particles with diameters around 200 nm, a decrease of particle concentration was detected.
In contrast, the event on 23^{rd} of January 2014 showed a different picture. The highest particle number concentrations were measured for diameters between 30 nm and 60 nm (Fig 5.14 (a)). Two periods of significant precipitation were detected, from 15:00 UTC to 16:50 UTC and from 20:00 UTC to 21:00 UTC (Fig 5.14 (b)). Due to strong changes in wind direction from 19:00 UTC to 21:00 UTC the later precipitation event is considered to happen during an unstable period (Fig 5.14 (d)). With the onset of precipitation at 15:00 UTC a decrease of particle number concentration for a wide range of particle diameters from 10 nm to 100 nm can be observed.

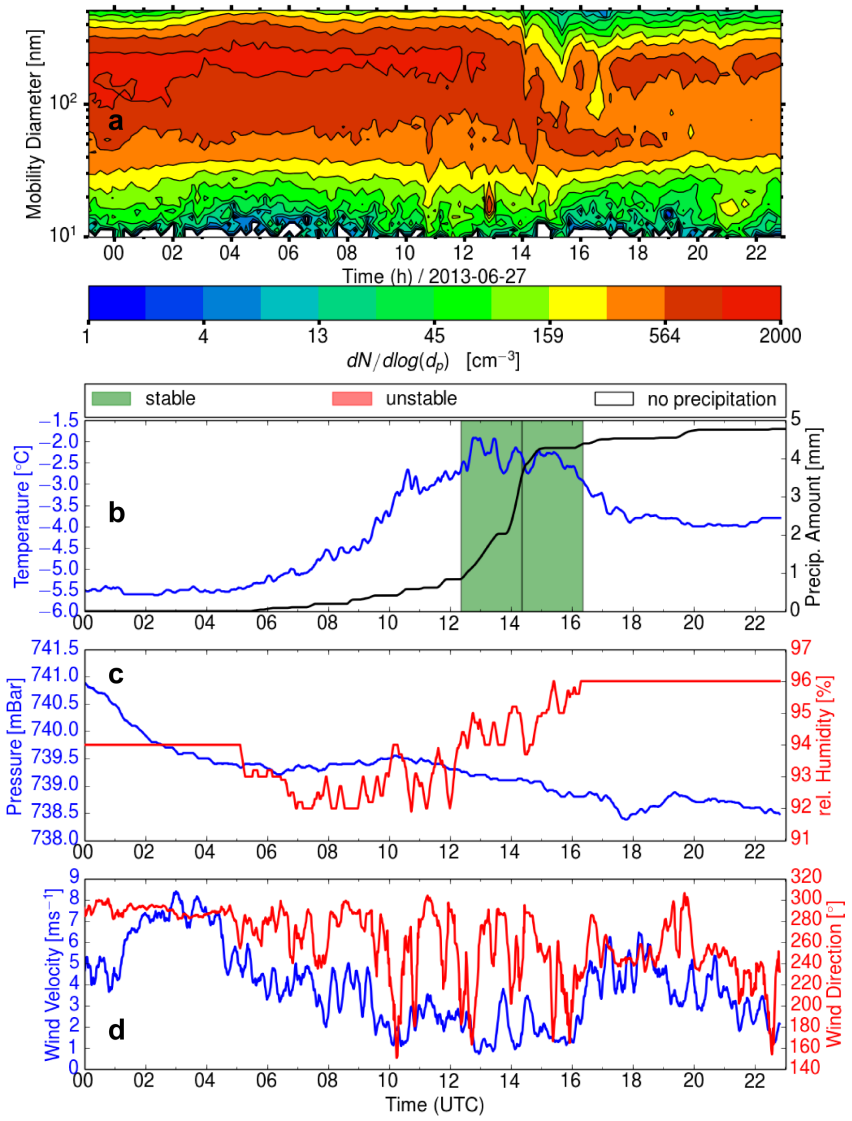

Figure 5.13: Time-resolved aerosol particle size distribution measured on 27^{th} of June 2013 (a). Temperature (b), pressure, relative humidity (c), wind speed and wind direction (d) were measured by the *Deutscher Wetterdienst* (DWD) at the environmental research station Schneefernerhaus. Particle size distribution measurements were provided by the German Environment Agency.

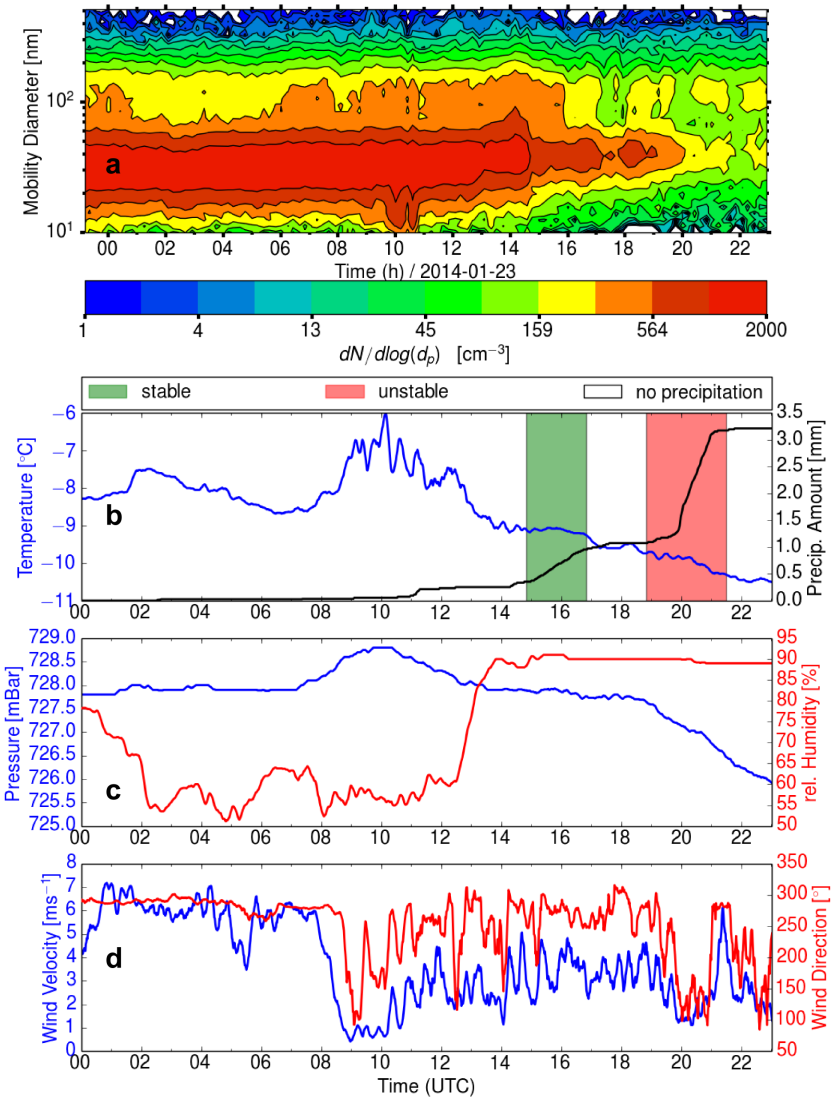

Figure 5.14: Time-resolved aerosol particle size distribution measured on 23^{rd} of January 2014 (a). Temperature (b), pressure, relative humidity (c), wind speed and wind direction (d) were measured by the *Deutscher Wetterdienst* (DWD) at the environmental research station Schneefernerhaus. Particle size distribution measurements were provided by the German Environment Agency.

5.5 Scavenging coefficients

For periods where precipitation could be identified as the major sink of aerosol particle number concentration, scavenging coefficients were calculated according to the linear fit method described in chapter 4.2.5. For solid, mixed and liquid phase precipitation, scavenging coefficients are shown in Fig. 5.15. For better comparability, these scavenging coefficients are also plotted with logarithmic scale in Fig. 5.16.

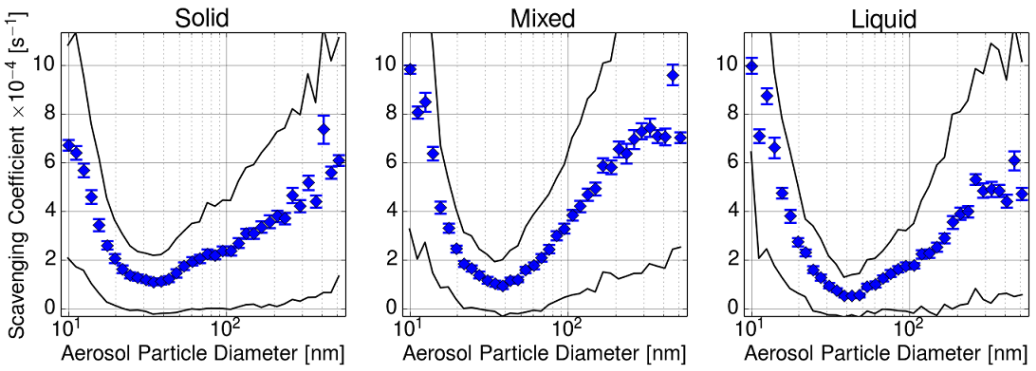

Figure 5.15: Mean scavenging coefficients for solid, mixed and liquid phase precipitation. The error bars denote the uncertainty of the mean value. The black lines mark the 16^{th} and the 84^{th} percentile.

The scavenging coefficients shown in Fig. 5.15 and Fig. 5.16 show a clear dependence on the aerosol particle diameter and spread over approximately one and a half orders of magnitude. The black lines in Fig 5.15 mark the 16^{th} and the 84^{th} percentile. This means that 68% of the measured scavenging coefficients are between the black lines. For solid phase precipitation events, scavenging coefficients range from $(1.0 \pm 0.1) \cdot 10^{-4}\,\mathrm{s}^{-1}$ to $(7.4 \pm 0.5) \cdot 10^{-4}\,\mathrm{s}^{-1}$ with a mean value averaged over the total size range of $(3.3 \pm 0.2) \cdot 10^{-4}\,\mathrm{s}^{-1}$. The highest scavenging coefficients can be found for the smallest aerosol particle diameters around 10 nm and for the largest diameters between 400 nm and 500 nm. In contrast, Aerosol particles with diameters from 30 nm to 50 nm have the lowest scavenging coefficients. The highest mean scavenging coefficient averaged over the whole size range is found for mixed phase events with $(4.5 \pm 0.2) \cdot 10^{-4}\,\mathrm{s}^{-1}$, spreading from about $(9.0 \pm 1.2) \cdot 10^{-5}\,\mathrm{s}^{-1}$ for aerosol particles between 30 nm and 50 nm to $(1.0 \pm 0.2) \cdot 10^{-3}\,\mathrm{s}^{-1}$ for the smallest and the largest particle diameters. Finally, liquid phase precipitation events have a mean scavenging coefficient of $(3.2 \pm 0.2) \cdot 10^{-4}\,\mathrm{s}^{-1}$ averaged over the whole size range. Here, a deep minimum of $(5.0 \pm 0.7) \cdot 10^{-5}\,\mathrm{s}^{-1}$ is

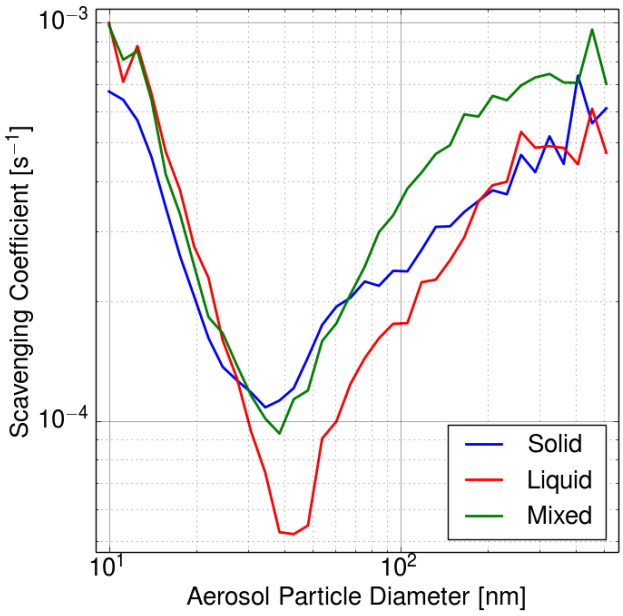

Figure 5.16: Mean scavenging coefficients for solid, mixed and liquid phase precipitation. For better comparability, the data from Fig. 5.15 is plotted onto the same axis with logarithmic scale. Uncertainties can be accessed in Fig. 5.15.

observed for particles between 40 nm and 50 nm. Maximum values of up to $(1.0 \pm 0.3) \cdot 10^{-3}\,\mathrm{s}^{-1}$ are found for the smallest particle diameters around 10 nm.
In the following, scavenging coefficients are plotted without error bars for reasons of clarity.

5.6 Scavenging coefficients for liquid phase events

For liquid phase precipitation events, the influence of precipitation intensity on the scavenging coefficient was also analyzed. Fig. 5.17 (a) shows the scavenging coefficients as a function of aerosol particle size for three different classes of precipitation rate. For events with precipitation rates of less than $2.0\,\mathrm{mmh}^{-1}$ the mean scavenging coefficient averaged over the whole size range is $(2.8 \pm 0.2) \cdot 10^{-4}\,\mathrm{s}^{-1}$, for those between $2.0\,\mathrm{mmh}^{-1}$ and $4.0\,\mathrm{mmh}^{-1}$ it is $(3.8 \pm 0.2) \cdot 10^{-4}\,\mathrm{s}^{-1}$ and for those larger than $4.0\ \mathrm{mmh}^{-1}$ it is $(4.4 \pm 0.3) \cdot 10^{-4}$

s^{-1}. Over the whole size range a tendency to higher scavenging coefficients for higher precipitation rates can be observed. This tendency is more pronounced for particles larger than 60 nm and for particles smaller than 30 nm, while it is less pronounced for particles between 40 nm and 50 nm.
Plotting the mean scavenging coefficient for the whole size range as a function of precipitation rate (Fig. 5.17 (b)) shows rising scavenging coefficients for rising precipitation rate. In this figure, the precipitation rate is represented by mean values and standard deviations in the intervals $I < 2.0\,\mathrm{mmh}^{-1}$, $2.0\,\mathrm{mmh}^{-1} \leq I < 4.0\,\mathrm{mmh}^{-1}$ and $4.0\,\mathrm{mmh}^{-1} \leq I$. A fit of a power function $\lambda = A \cdot (I/I_0)^B$ to the measured data yielded $A = (2.9 \pm 0.005) \cdot 10^{-4}\,\mathrm{s}^{-1}$ and $B = 0.25 \pm 0.001$.

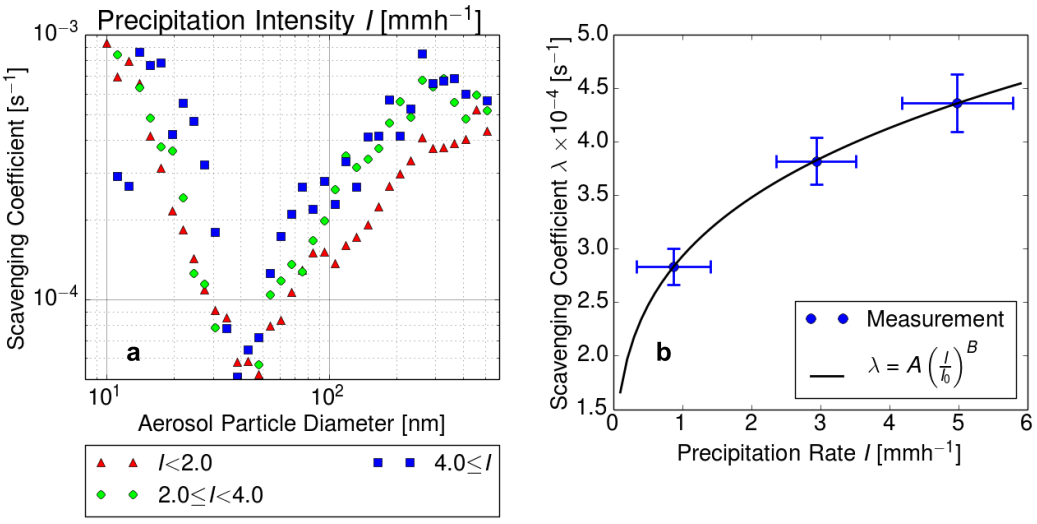

Figure 5.17: Aerosol particle size dependent scavenging coefficients, for three different classes of precipitation intensity and only liquid phase precipitation (a). Measurement uncertainties can be accessed in Fig. 5.15. Scavenging coefficients as a function of precipitation rate, for liquid phase events (b). The precipitation rate is represented by mean values and standard deviations in the intervals $I < 2.0\,\mathrm{mmh}^{-1}$, $2.0\,\mathrm{mmh}^{-1} \leq I < 4.0\,\mathrm{mmh}^{-1}$ and $4.0\,\mathrm{mmh}^{-1} \leq I$. For the fit parameters the following values were obtained: $A = (2.9 \pm 0.005) \cdot 10^{-4}\,\mathrm{s}^{-1}$, $B = 0.25 \pm 0.001$.

5.7 Scavenging coefficients for mixed phase events

For mixed phase precipitation events with precipitation rates below $2.0\,\mathrm{mmh}^{-1}$ the mean scavenging coefficient averaged over the whole size range is $(4.4 \pm$

$0.2) \cdot 10^{-4}\,\mathrm{s}^{-1}$, for those between $2.0\,\mathrm{mmh}^{-1}$ and $4.0\,\mathrm{mmh}^{-1}$ it is $(6.3 \pm 0.2) \cdot 10^{-4}\,\mathrm{s}^{-1}$ and for those larger than $4.0\,\mathrm{mmh}^{-1}$ it is $(1.3 \pm 0.1) \cdot 10^{-4}\,\mathrm{s}^{-1}$ (Fig. 5.18 (a)). The tendency of increasing scavenging coefficients with increasing precipitation rate is more pronounced for aerosol particles larger than 30 nm. In contrast, for aerosol particles between 20 nm and 30 nm lower scavenging coefficients for higher precipitation rates are observed.
Plotting the mean scavenging coefficient averaged over the whole size range as a function of precipitation rate (Fig. 5.18 (b)) shows increasing scavenging coefficients for increasing precipitation rate. In this figure, the precipitation rate is represented by mean values and standard deviations in the intervals $I < 1.0\,\mathrm{mmh}^{-1}$, $1.0\,\mathrm{mmh}^{-1} \leq I < 2.0\,\mathrm{mmh}^{-1}$ and $2.0\,\mathrm{mmh}^{-1} \leq I < 3.0\,\mathrm{mmh}^{-1}$. A fit of the power function $\lambda = A \cdot (I/I_0)^B$ to the measured data yielded $A = (5.3 \pm 0.2) \cdot 10^{-4}\,\mathrm{s}^{-1}$ and $B = 0.20 \pm 0.02$.

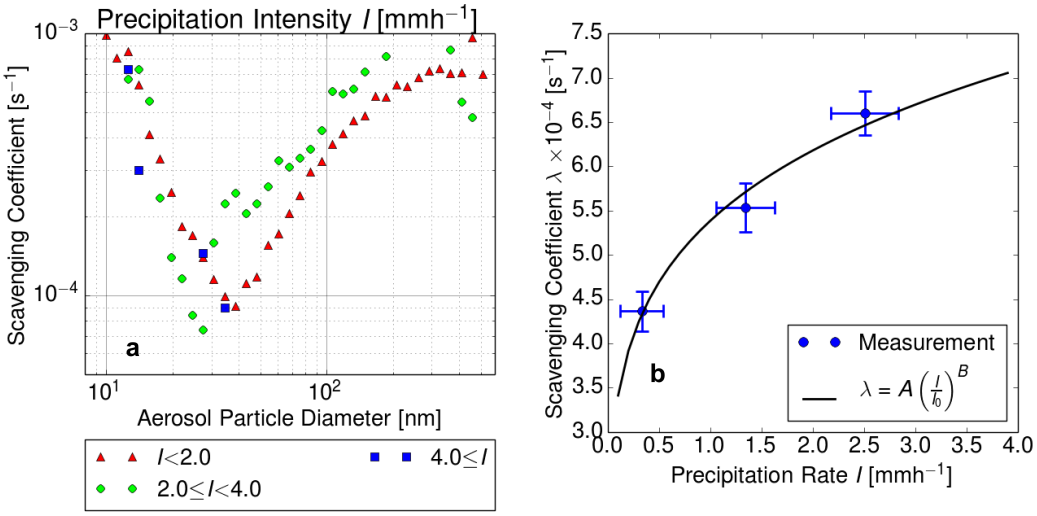

Figure 5.18: Aerosol particle size dependent scavenging coefficients, for three different classes of precipitation intensity and mixed phase precipitation (a). Measurement uncertainties can be accessed in Fig. 5.15. Scavenging coefficients as a function of precipitation rate, for mixed phase events (b). The precipitation rate is represented by mean values and standard deviations in the intervals $I < 1.0\,\mathrm{mmh}^{-1}$, $1.0\,\mathrm{mmh}^{-1} \leq I < 2.0\,\mathrm{mmh}^{-1}$ and $2.0\,\mathrm{mmh}^{-1} \leq I < 3.0\,\mathrm{mmh}^{-1}$. For the fit parameters the following values were obtained: $A = (5.3 \pm 0.2) \cdot 10^{-4}\,\mathrm{s}^{-1}$, $B = 0.20 \pm 0.02$.

5.8 Scavenging coefficients for solid phase events

Because of the large variety of surface structures of solid hydrometeors, scavenging coefficients for events consisting of solid phase hydrometeors were analyzed in more detail.

5.8.1 Precipitation rate

Considering only the dependencies on aerosol particle size and precipitation rate the following observations were made (Fig. 5.19 (a)): For events with precipitation rates of less than $2.0\,\mathrm{mmh}^{-1}$ the mean scavenging coefficient averaged over the whole size range is $(3.1 \pm 0.2) \cdot 10^{-4}\,\mathrm{s}^{-1}$, for those between $2.0\,\mathrm{mmh}^{-1}$ and $4.0\,\mathrm{mmh}^{-1}$ it is $(4.7 \pm 0.3) \cdot 10^{-4}\,\mathrm{s}^{-1}$ and for those larger than $4.0\,\mathrm{mmh}^{-1}$ it is $(4.5 \pm 0.2) \cdot 10^{-4}\,\mathrm{s}^{-1}$. A clear tendency to higher scavenging coefficients for higher precipitation rates is only seen for aerosol particles larger than 50 nm.

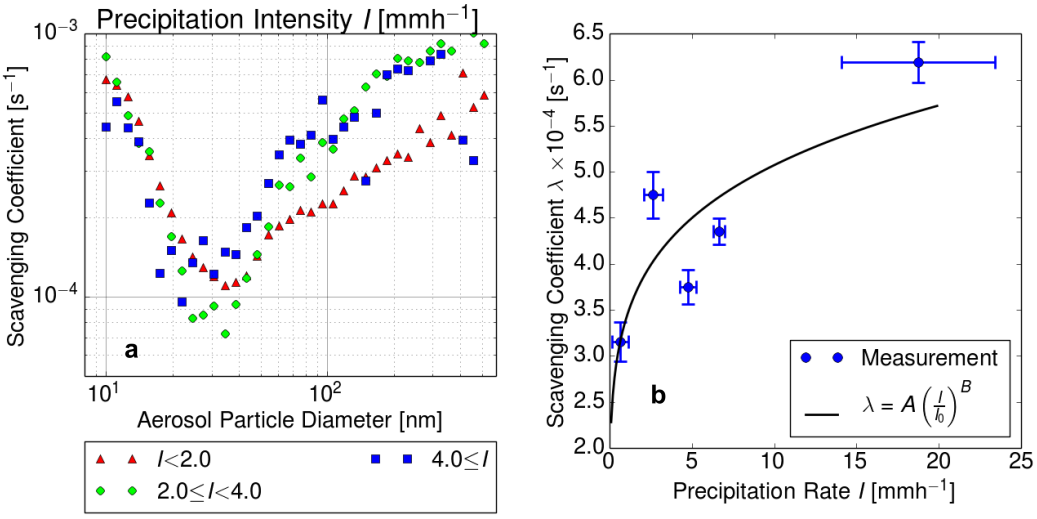

Figure 5.19: Aerosol particle size dependent scavenging coefficients, for three different classes of precipitation intensity and solid phase precipitation (a). Measurement uncertainties can be accessed in Fig. 5.15. Scavenging coefficients as a function of precipitation rate, for solid phase events (b). The precipitation rate is represented by mean values and standard deviations in the intervals $I < 2.0\,\mathrm{mmh}^{-1}$, $2.0\,\mathrm{mmh}^{-1} \leq I < 4.0\,\mathrm{mmh}^{-1}$, $4.0\,\mathrm{mmh}^{-1} \leq I < 6.0\,\mathrm{mmh}^{-1}$, $6.0\,\mathrm{mmh}^{-1} \leq I < 8.0\,\mathrm{mmh}^{-1}$ and $8.0\,\mathrm{mmh}^{-1} \leq I$. For the fit parameters the following values were obtained: $A = (3.4 \pm 0.4) \cdot 10^{-4}\,\mathrm{s}^{-1}$, $B = 0.17 \pm 0.02$.

Plotting the mean scavenging coefficient averaged over the whole size range as a function of precipitation rate (Fig. 5.19 (b)) again shows increasing scavenging coefficients for increasing precipitation rates. The precipitation rate is represented by mean values and standard deviations in the intervals $I < 2.0\,\mathrm{mmh}^{-1}$, $2.0\,\mathrm{mmh}^{-1} \leq I < 4.0\,\mathrm{mmh}^{-1}$, $4.0\,\mathrm{mmh}^{-1} \leq I < 6.0\,\mathrm{mmh}^{-1}$, $6.0\,\mathrm{mmh}^{-1} \leq I < 8.0\,\mathrm{mmh}^{-1}$ and $8.0\,\mathrm{mmh}^{-1} \leq I$. A fit of the power function $\lambda = A \cdot (I/I_0)^B$ to the measured data yielded $A = (3.4 \pm 0.4) \cdot 10^{-4}\,\mathrm{s}^{-1}$ and $B = 0.17 \pm 0.02$.

5.8.2 Classes of dominating degree of riming and crystal type

Applying the classification method for solid phase precipitation events described in chapter 4.1.2.4 allows calculation of scavenging coefficients for different classes of degree of riming and crystal type of hydrometeors dominating in the investigated precipitation event.
Fig. 5.20 (a) shows scavenging coefficients as a function of aerosol particle size and degree of riming of hydrometeors. For the whole size spectrum differences in scavenging coefficients between the single degrees of riming are very small. Looking at mean values averaged over the whole size range weakly rimed events show a mean scavenging coefficient of $(3.5 \pm 0.2) \cdot 10^{-4}\,\mathrm{s}^{-1}$, while moderately rimed events show a mean scavenging coefficient of $(3.3 \pm 0.2) \cdot 10^{-4}\,\mathrm{s}^{-1}$ and strongly rimed events a mean scavenging coefficient of $(3.1 \pm 0.2) \cdot 10^{-4}\,\mathrm{s}^{-1}$. When the scavenging coefficients are calculated separately for the different dominating crystal types observed in a certain precipitation event, the following observations are obvious (Fig. 5.20 (b)): Events consisting mainly of single crystal hydrometeors show the highest scavenging coefficients, especially for aerosol particle diameters larger than 30 nm. In the same size range complex crystal events show larger scavenging coefficients than events consisting mainly of pellets. For the smaller particle size range (10 nm to 30 nm), the differences are not so clear, although for aerosol particles around 10 nm, pellets have the largest scavenging coefficient. The mean values averaged over the whole size range are: $(4.0 \pm 0.2) \cdot 10^{-4}\,\mathrm{s}^{-1}$ for single crystals, $(3.4 \pm 0.3) \cdot 10^{-4}\,\mathrm{s}^{-1}$ for complex crystals and $(2.6 \pm 0.2) \cdot 10^{-4}\,\mathrm{s}^{-1}$ for pellets, respectively.

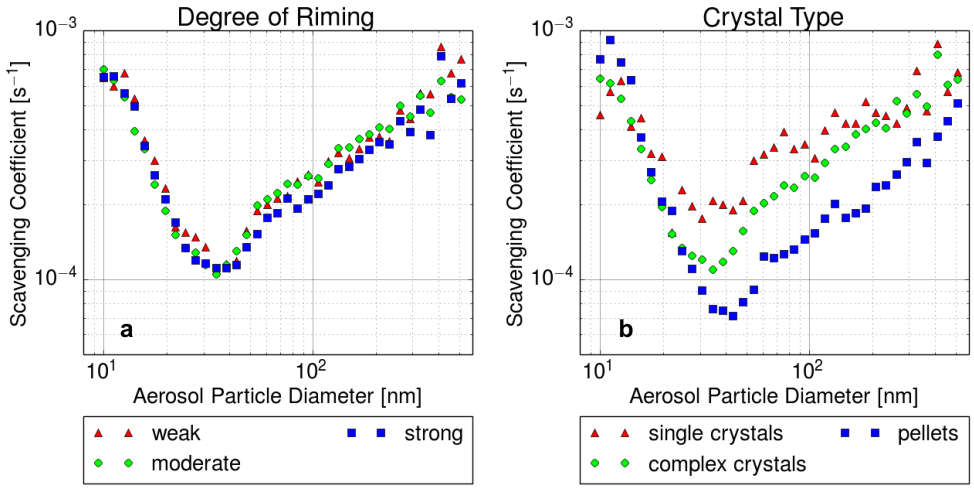

Figure 5.20: Scavenging coefficients as a function of aerosol particle size and degree of riming of hydrometeors (a). Scavenging coefficients as a function of aerosol particle size and dominating crystal type of hydrometeors (b). Measurement uncertainties can be accessed in Fig. 5.15.

5.8.3 Micro physical parameters of solid hydrometeors

Using directly recorded micro-physical parameters of hydrometeors instead of the precipitation event classes, allows a more detailed analysis.

- Regarding the elongation E of hydrometeors, a clear tendency towards higher scavenging coefficients with larger elongation can be observed for aerosol particle diameters between 30 nm and 100 nm. For elongations larger than 4.0 this behavior is less pronounced for aerosol particles larger than 100 nm (Fig. 5.21 (a)). In contrast, for aerosol particles smaller than 30 nm no clear tendency is seen. The following mean values averaged over the whole size range were obtained: $(2.7 \pm 0.2) \cdot 10^{-4}\,\mathrm{s}^{-1}$ for $E < 2.0$, $(3.3 \pm 0.2) \cdot 10^{-4}\,\mathrm{s}^{-1}$ for $2.0 \leq E < 3.0$, $(3.7 \pm 0.2) \cdot 10^{-4}\,\mathrm{s}^{-1}$ for $3.0 \leq E < 4.0$ and $(4.2 \pm 0.3) \cdot 10^{-4}\,\mathrm{s}^{-1}$ for $4.0 \leq E$, respectively.

- Regarding the shape factor S of hydrometeors, a clear tendency towards higher scavenging coefficients with smaller shape factor can be observed for aerosol particle diameters between 30 nm and 100 nm. For shape factors smaller than 0.4 this behavior is less pronounced for aerosol particles larger than 100 nm (Fig. 5.21 (b)). For aerosol particles around 10 nm, hydrometeors with larger shape factors tend to have larger

scavenging coefficients. The following mean values averaged over the whole size range were obtained: $(3.4 \pm 0.2) \cdot 10^{-4}\,\mathrm{s}^{-1}$ for $S < 0.4$, $(3.3 \pm 0.2) \cdot 10^{-4}\,\mathrm{s}^{-1}$ for $0.5 \leq S < 0.5$ and $(3.0 \pm 0.2) \cdot 10^{-4}\,\mathrm{s}^{-1}$ for $0.4 \leq S$.

- Regarding the roundness R of hydrometeors, a clear tendency towards higher scavenging coefficients with smaller roundness can be observed for aerosol particle diameters between 30 nm and 100 nm. For roundness values smaller than 0.4 this behavior is less pronounced, for aerosol particles larger than 100 nm (Fig. 5.21 (c)). For aerosol particles smaller than 30 nm no clear tendency is seen. The following mean values averaged over the whole size range were obtained: $(4.0 \pm 0.2) \cdot 10^{-4}\,\mathrm{s}^{-1}$ for $R < 0.4$, $(3.5 \pm 0.2) \cdot 10^{-4}\,\mathrm{s}^{-1}$ for $0.4 \leq R < 0.5$ and $(3.1 \pm 0.2) \cdot 10^{-4}\,\mathrm{s}^{-1}$ for $0.5 \leq R$.

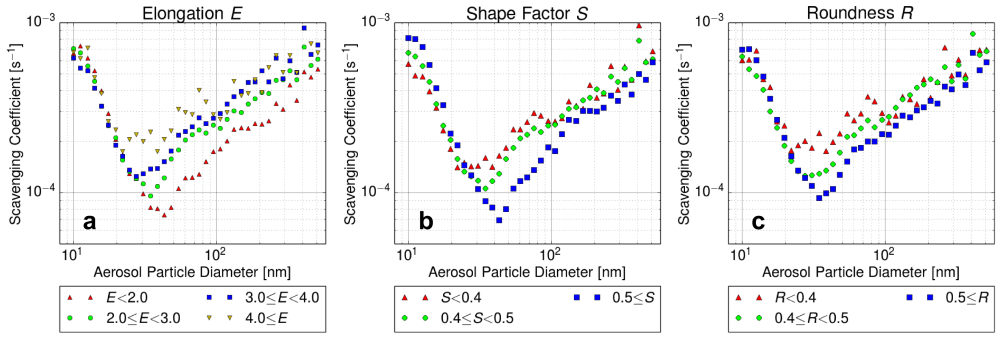

Figure 5.21: Scavenging coefficients as a function of aerosol particle diameter and micro physical parameters of solid hydrometeors: elongation (a), shape factor (b) and roundness (c). Measurement uncertainties can be accessed in Fig. 5.15.

- Analyzing the scavenging coefficient as a function of maximum dimension D of hydrometeors does not show any clear tendency, for the whole size range (Fig. 5.22 (a)). The following mean values averaged over the whole size range were obtained: $(2.9 \pm 0.2) \cdot 10^{-4}\,\mathrm{s}^{-1}$ for $D < 1.0\,\mathrm{mm}$, $(3.1 \pm 0.2) \cdot 10^{-4}\,\mathrm{s}^{-1}$ for $1.0\,\mathrm{mm} \leq D < 1.5\,\mathrm{mm}$, $(3.9 \pm 0.2) \cdot 10^{-4}\,\mathrm{s}^{-1}$ for $1.5\,\mathrm{mm} \leq D < 2.0\,\mathrm{mm}$, $(3.5 \pm 0.2) \cdot 10^{-4}\,\mathrm{s}^{-1}$ for $2.0\,\mathrm{mm} \leq D < 2.5\,\mathrm{mm}$ and $(2.6 \pm 0.1) \cdot 10^{-4}\,\mathrm{s}^{-1}$ for $2.5\,\mathrm{mm} \leq D$.

- Analyzing the scavenging coefficient as a function of hydrometeor volume V shows a tendency to higher scavenging coefficients for smaller volumes (Fig. 5.22 (b)). The difference is especially pronounced for

aerosol particle larger than 30 nm and hydrometeor volumes larger than 5.0 mm^3. The following mean values averaged over the whole size range were obtained: $(3.3 \pm 0.2) \cdot 10^{-4}\,s^{-1}$ for $V < 5.0\,mm^3$, $(2.7 \pm 0.2) \cdot 10^{-4}\,s^{-1}$ for $5.0\,mm^3 \leq V < 10.0\,mm^3$ and $(2.2 \pm 0.1) \cdot 10^{-4}\,s^{-1}$ for $10.0\,mm^3 \leq V$.

- Finally, analyzing the scavenging coefficient as a function of vertical velocity v of hydrometeors does not reveal any clear tendency for the whole size range (Fig. 5.22 (c)). The following mean values averaged over the whole size range were obtained: $(3.0 \pm 0.2) \cdot 10^{-4}\,s^{-1}$ for $v < 1.0\,ms^{-1}$, $(3.4 \pm 0.2) \cdot 10^{-4}\,s^{-1}$ for $1.0\,ms^{-1} \leq v < 1.5\,ms^{-1}$, $(3.6 \pm 0.3) \cdot 10^{-4}\,s^{-1}$ for $1.5\,ms^{-1} \leq v < 2.0\,ms^{-1}$ and $(4.2 \pm 0.2) \cdot 10^{-4}\,s^{-1}$ for $2.0\,ms^{-1} \leq v$.

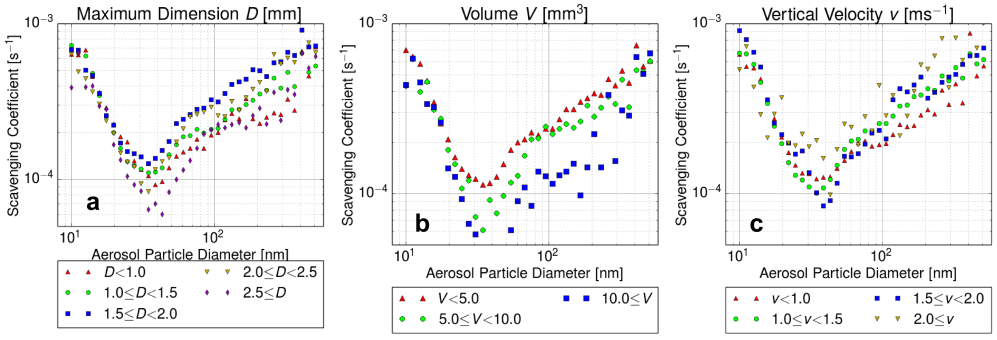

Figure 5.22: Scavenging coefficients as a function of aerosol particle diameter and micro physical parameters of solid hydrometeors: maximum dimension (a), Volume (b), vertical velocity (c). Measurement uncertainties can be accessed in Fig. 5.15.

5.9 Deposition of particle bound radionuclides

5.9.1 Activity size distributions

In the atmosphere, the radionuclides ^{7}Be, ^{137}Cs and ^{210}Pb are predominantly bound to aerosol particles with different sizes. For an investigation of the washout efficiency for particle-bound radionuclides the activity size distribution is an important parameter. Therefore, aerosols were collected in a 14 stage cascade impactor (ELPI+) for periods of three to four weeks. The result of the following gamma spectrometric analysis of the single impactor stages is shown in Fig. 5.23. In this experiment, the collection periods were

from 10^{th} of July 2013 to 2^{nd} of August 2013 (Fig. 5.23 (a)) and from 13^{th} of February 2014 to 11^{th} of March 2014 (Fig. 5.23 (b)). For both sampling periods a clear maximum for the ^{7}Be concentration can be observed for aerosol particle sizes between 300 nm and 500 nm. For the same size range, a slight maximum was also detected for the ^{210}Pb concentration. Finally, the activity size distribution for ^{137}Cs also shows a local maximum for aerosol particles with diameters around 400 nm.

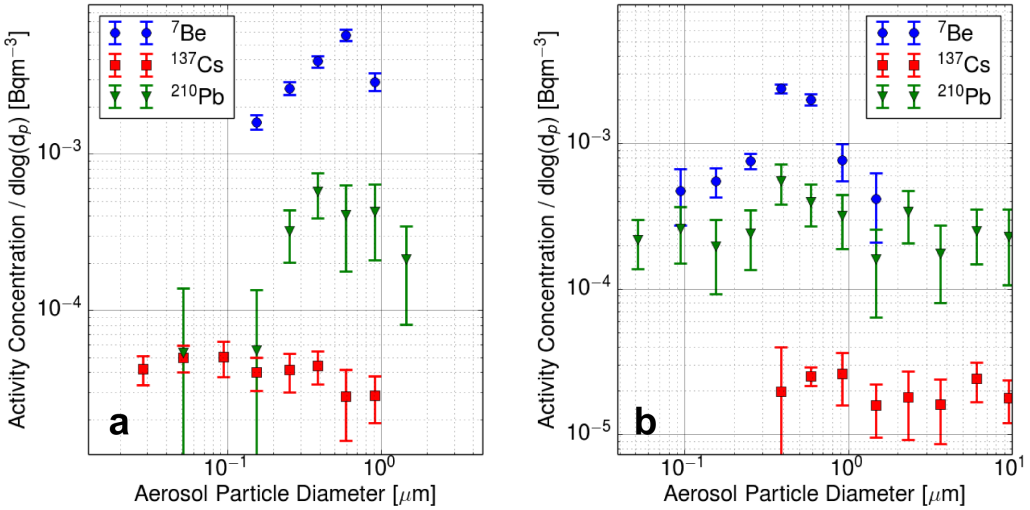

Figure 5.23: Activity size distributions for the radionuclides ^{7}Be, ^{137}Cs and ^{210}Pb. The sampling period was from 10^{th} of July 2013 to 2^{nd} of August 2013 (a) and from 13^{th} of February 2014 to 11^{th} of March 2014 (b).

Table 5.5: Fit parameters A and B for the fitted power function $\lambda = A \cdot (I/I_0)^B$ from Fig. 5.24, for different types of precipitation events.

precipitation type	$A \times 10^{-4}$ [s^{-1}]	B
solid, single	4.7 ± 0.4	0.49 ± 0.05
solid, complex	3.22 ± 0.01	0.45 ± 0.01
solid, pellets	2.8 ± 0.7	0.7 ± 0.08
mixed	4.55 ± 0.01	0.39 ± 0.01
liquid	2.41 ± 0.03	1.38 ± 0.01

Fig. 5.24 shows scavenging coefficients as a function of the precipitation rate for aerosol particle diameters from 300 nm to 500 nm and for different types of precipitation. The fit parameters A and B for the fitted power function $\lambda = A \cdot (I/I_0)^B$ are listed in Tab. 5.5.

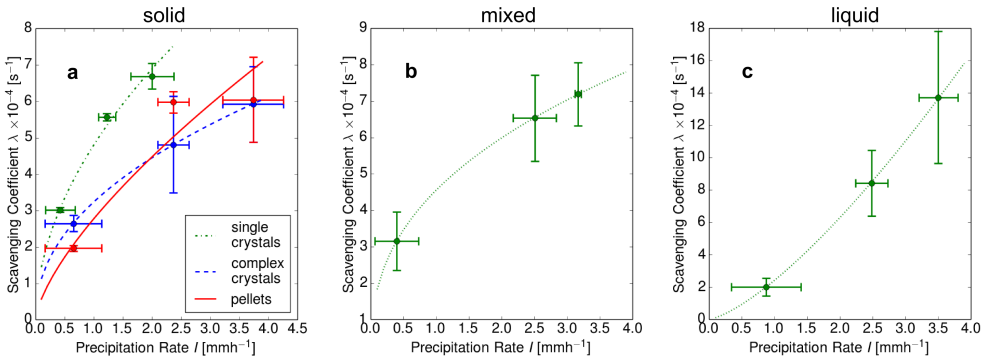

Figure 5.24: Scavenging coefficients as a function of precipitation rate for aerosol particle diameters from 300 nm to 500 nm. Solid phase events are shown in (a), mixed phase events in (b) and liquid phase events in (c). The fit parameters A and B for the fitted power function $\lambda = A \cdot (I/I_0)^B$ are listed in Tab. 5.5.

Calculating the ratio between the fitted power functions for different solid phase precipitation types and liquid phase precipitation makes a direct comparison between parameterizations of scavenging coefficients possible (Fig. 5.25). Complex crystal and pellet events have a ratio which is larger than one, when the water equivalent precipitation rate is below 1.5 mmh^{-1}. For events with water equivalent precipitation rates larger than 1.5 mmh^{-1} the ratio is smaller than one. Comparing solid phase single crystal events to liquid phase events the ratio is larger than one for water equivalent precipitation rates lower than 2.0 mmh^{-1}.

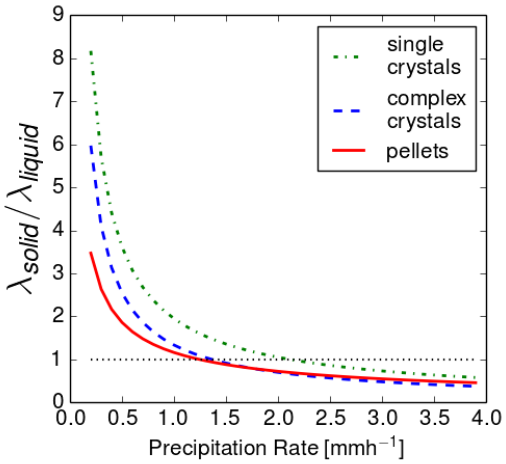

Figure 5.25: The ratio between the fitted power functions for solid and liquid phase events as a function of water equivalent precipitation rate. The ratio is shown for the three different crystal types of solid phase precipitation.

5.9.2 Activity scavenging coefficients

For two precipitation events the decrease in atmospheric activity concentration was observed directly by taking filter samples with a high volume aerosol sampling station (ASS1000, see chapter 4.2.3). The results are shown in Fig. 5.26. With the onset of precipitation a clear decrease in activity concentration can be observed for ^{7}Be and ^{210}Pb. For the shown sampling intervals the activity concentration of ^{137}Cs was always below the detection limit. Calculating activity scavenging coefficients with two consecutive measurements of activity concentration including the onset of precipitation (see chapter 4.2.5) delivers the following values: On 14^{th} of January 2014 the activity scavenging coefficient was $(3.2 \pm 0.1) \cdot 10^{-4}\,\mathrm{s}^{-1}$ for ^{7}Be and $(2.8 \pm 0.4) \cdot 10^{-4}\,\mathrm{s}^{-1}$ for ^{210}Pb. On 30^{th} of September 2014 the activity scavenging coefficient was $(2.2 \pm 0.2) \cdot 10^{-4}\,\mathrm{s}^{-1}$ for ^{7}Be and $(1.3 \pm 0.8) \cdot 10^{-4}\,\mathrm{s}^{-1}$ for ^{210}Pb.

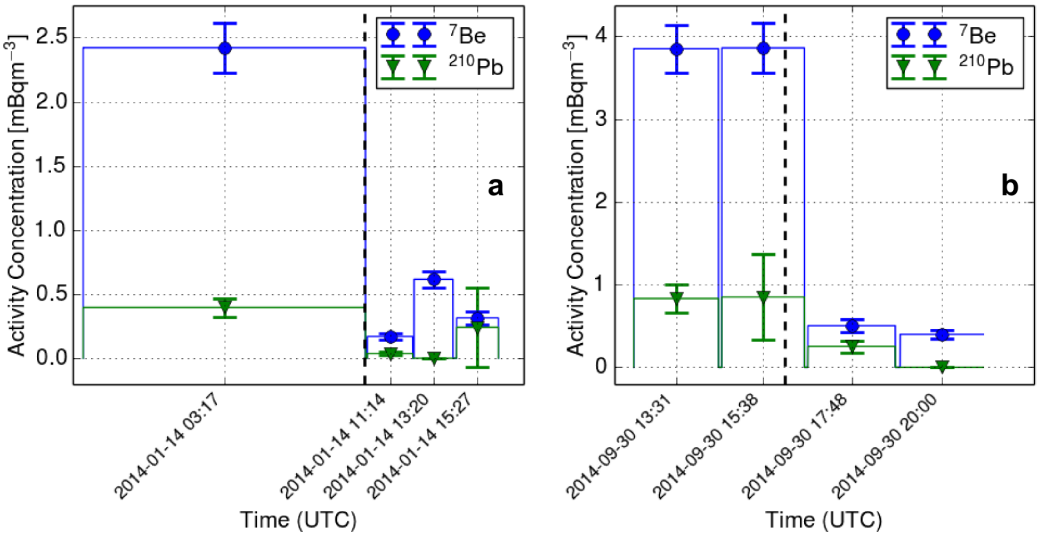

Figure 5.26: Atmospheric activity concentrations for the radionuclides ^{7}Be and ^{210}Pb during a solid phase precipitation event on 1^{st} of January 2014 (a) and for a liquid phase precipitation event on 30^{th} of September 2014 (b). The black dashed line marks the onset of precipitation.

Chapter 6

Discussion

6.1 Evaluation of 2DVD performance

6.1.1 Calibration with solid steel spheres

In the calibration experiments for the 2D-video disdrometer a systematic deviation of the measured diameter of solid spheres compared to their nominal diameter was observed (Fig. 5.1, left panel). The reason for the systematic deviation can be a small misalignment of the optical elements caused by transportation or small deformations of the housing through strong winds. Because of the constant overestimation of the measured size expressed in the intercept t of the regression line, a correction procedure had to be implemented for the pixel width. After this correction the nominal and measured values agree very well (Fig. 5.1 right panel).

6.1.2 Measurement ranges and uncertainties

With a certain threshold partially shaded pixels in the 2DVD images are counted as fully shaded or fully non-shaded. This introduces a non avoidable error that increases with decreasing size of the detected object (Fig. 5.2). For reliable shape and size measurements with a 2DVD it is recommended to take only particles with a minimum dimension of at least 0.5 mm for data evaluation. Size and shape characterization with a relative standard deviation of less than 5% is only possible for particles larger than 1.0 mm. For particles between 0.5 mm and 1.0 mm the relative standard deviation can grow up to 22% for the volume, 17% for size parameters and 14% for shape descriptors.

6.1.3 Validation of 2DVD measurements

The 2DVD measurement with the solid spheres revealed how well shape, size and velocity information gained with 2DVD measurements agree with their nominal values.

a) The expected value of the **elongation**, $E = 1$, was reproduced very well by the 2DVD measurements (Figs. 5.3 a and b). The outliers at 0.5 mm, 2 mm, 3 mm, 4 mm and 5 mm were for single measurements where partially shadowed edge pixels artificially increase the width.

b) Especially for the larger spheres the nominal **roundness** value of $R = 1$ is reproduced very well. With smaller diameters the influence of the pixel shaped edge gets larger. As a consequence the measured shape deviates more from a sphere and the values are spread more widely (Fig. 5.3 c and d).

c) The nominal value for the **shape factor** of a sphere is $S = 1$. In contrast, the measured values were between 0.6 and 0.7. The reason for this deviation is the pixel-shaped perimeter of the pictures. The perimeter of a convex pixel-shaped object is always equal to the perimeter of the surrounding rectangle. For example, a spherical object with a pixel-shaped edge and a diameter of 6 mm has a theoretically calculated shape factor of 0.62. Using a blurring edge filter that spreads over 20 pixels before detecting the perimeter of the object improves the the shape factors to values between 0.90 and 0.95 (Fig. 5.3 e to h). Especially for solid precipitation particles with very fine features image processing with a blurring edge filter is not recommended, because the risk of loosing important information is too high.

d) The measurement quality of the **maximum dimension** (Fig. 5.1),

e) **equivalent diameters** (Fig. 5.4 a) and

f) **volumes** is excellent for particles larger than 0.5 mm (Fig. 5.4 b).

g) The comparison between measured and theoretically calculated vertical **fall velocity** shows very good agreement (5.4 c).

In the experiment with styrofoam particles the mismatch probability was around 3%. For particles with sizes less than 3 mm the theoretical prediction of the vertical velocity for spherical particles with a density of 270.0 kgm^{-3} is plotted in Fig. 5.5. The particles with sizes around 2 mm follow this prediction very well. The measured size and velocity depends strongly on the

orientation of the particle. For this reason a small spread around the single measurements has to be accepted.
For results without matching artifacts it is essential to introduce a suitable matching algorithm. The original matching algorithm produces a large amount of mismatches. Less than 9% of the registered events fulfill the criteria to be simultaneously detected hydrometeors by both cameras (Tab. 5.2). For shape parameter measurements in case of real solid phase precipitation, the 2DVD shows the expected correlations (Figs. 5.6 a to c).

6.2 Evaluation of precipitation event classification

The decision tree based classification method for solid phase hydrometeors, which is based on the dominating degree of riming and crystal type, was validated in the following way: Results from visual picture classification were compared to the automatic 2D-Video Disdrometer classification results. The obtained consistency matrix (Tab. 5.4) shows a very good match between the visual picture classification and the automatic 2DVD classification. The table suggests that an overall probability for wrong classification of about 12%. Barthazy and Schefold (2006) report ranges for the power function exponent β for snow crystals with different degree of riming. In their study they found β between 0.17 and 0.29 for unrimed and moderately rimed crystals, while for densely rimed crystals they found values for β up to 0.51. Finally, for graupel, they found a value for β of 0.61. The values for β which define the classification of the degree of riming in the present study, are in good agreement with this ranges.
Pellets and graupel particles in general do not grow larger than 5 mm, and according to Locatelli and Hobbs (1974) they have densities between $0.05\,\mathrm{gcm}^{-3}$ and $0.45\,\mathrm{gcm}^{-3}$. The bulk density measured for the event shown in Fig. 5.9 exactly covers this range and only very rarely sizes larger than 5 mm were observed. The mean roundness stayed between 0.6 and 0.8 which indicates a large number of nearly spherically shaped hydrometeors. This justifies the 2DVD classification of this period as an event containing mostly densely rimed pellets.
For the period depicted in Fig. 5.10 the temperature curve shows a pattern which proves consistency of the 2DVD classification: The complex crystal periods were associated with higher temperatures above $-7.0°\mathrm{C}$, while temperatures below $-7.6°\mathrm{C}$ were found for the single crystal periods. This can be explained by the fact that snow crystals tend to stick together and build

aggregates at higher temperatures. Also a very low mean bulk density of $0.02\,\mathrm{gcm}^{-3}$ and larger mean maximum dimensions for the complex crystal periods than for the single crystal periods justify the 2DVD classification as single and complex crystals.
During the period shown in Fig. 5.11 the temperature stayed around 0.0°C which made the occurrence of large aggregates of snow crystals very probable. The high mean bulk density of $0.1\,\mathrm{gcm}^{-3}$ and the frequently occurring large maximum dimensions of up to 10 mm confirm the assumption that the event consisted of large aggregates of snow flakes containing a relatively high amount of liquid water. Again the classification as weakly rimed complex crystals is reasonable.
The fact that only 29 of the 468 (6%) classified one-minute events were labeled as *not classified* proves that the algorithm is applicable to most cases of real snowfall.

6.3 The basic set for data analysis and case studies

All measured precipitation events were analyzed for meteorological stability (see chapter 4.2.4), to minimize the influence of any parameter other than precipitation on aerosol particle concentration. Mainly due to strongly varying wind direction and wind speed and due to high wind velocities in general, only 12% of the detected precipitation were finally used for analysis. As expected for a high alpine measurement site, mostly solid phase precipitation (74%) occurred.
The two events selected as an example showed aerosol size distribution patterns that are in good agreement with those reported by Birmili et al. (2007): On 27^{th} of June 2013 (Fig 5.13), a day during summer season, a clear maximum in the accumulation mode can be observed. In contrast, in winter season, on 23^{rd} of January 2014, the maximum in aerosol particle size distribution is clearly shifted to young Aitken mode particles. As expected, both selected events showed a clear decrease of particle concentration with the onset of precipitation. This decrease was particularly pronounced for aerosol particles smaller than 60 nm and for aerosol particles larger than 100 nm. For unstable precipitation periods a decrease and an increase of aerosol particle concentration could be observed (23^{rd} of January 2014, 19:00 UTC to 21:00 UTC). This fact underlines the need of sorting out precipitation events with unstable meteorological conditions, because in these cases other reasons than precipitation can not be excluded to be responsible for the observed change

in aerosol particle concentration.
Additionally, during stable periods of precipitation slightly increasing aerosol particle concentrations can be observed mainly for nucleation and Aitken mode particles (27^{th} of June 2014, 13:00 UTC). The fact that nucleation and Aitken mode particles are present in relatively high concentrations independent from daytime and season suggests that in addition to production by solar irradiation, further processes for nucleation mode particle production exist on Mt. Zugspitze (Birmili et al., 2007). This justifies exclusion of all measurements where a significant increase of particle concentration was observed.

6.4 Scavenging coefficients for rain, solid phase and mixed phase events

For precipitation events for which below cloud scavenging could be identified as the major sink of atmospheric aerosol particle concentration, scavenging coefficients were calculated as a function of aerosol particle diameter. As a result, λ ranged from $(5.0 \pm 0.7) \cdot 10^{-5}\,\mathrm{s}^{-1}$ to $(1.0 \pm 0.2) \cdot 10^{-3}\,\mathrm{s}^{-1}$ (Fig. 5.16). These values are slightly below those reported by Graedel and Franey (1974), and agree quite well with the range of values measured by Schumann et al. (1988) and Volken and Schumann (1993). They are also in agreement with the range of values determined by Chate and Pranesha (2004) (from $1.1 \cdot 10^{-5}\,\mathrm{s}^{-1}$ to $7.6 \cdot 10^{-4}\,\mathrm{s}^{-1}$) for the scavenging of aerosol particles between 13 nm and 750 nm in rain events. In their studies on scavenging of ultra fine particles in boreal and urban sites in Finland, Laakso et al. (2003), Kyrö et al. (2009) and Paramonov et al. (2011) report lower scavenging coefficients in the range from $2.0 \cdot 10^{-6}\,\mathrm{s}^{-1}$ to $5.0 \cdot 10^{-5}\,\mathrm{s}^{-1}$ for rain and snow events. This might be due to the fact that these authors took all measurements for analysis, including those indicating an aerosol particle concentration increase beyond the instrumental background signal.
For all three phases of precipitation, a clear minimum could be identified for diameters between 30 nm and 60 nm (Fig. 5.16). Values for the size range of this so called Greenfield gap reported in a review by Sportisse (2007) range from 10 nm to 2.0 μm. There may be several reasons for the fact that the minimum observed in the present study is at the lower edge of the size range reported in literature. According to Pruppacher and Klett (1978) phoretic effects at high relative humidities (Fig. 6.1, Line 6 shows the collision efficiency for a relative humidity of 95%.) can shift the gap to lower particle diameters. Note that the measurements presented in the present

study mainly took place at a relative humidity above 70%. In addition, the fact that unknown source processes for nucleation and Aitken mode particles are obviously active on Mt. Zugspitze (Birmili et al., 2007) can lead to a relatively efficient reproduction of aerosol particles in the size range from 30 nm and 60 nm and make scavenging in this size range appear less efficient.

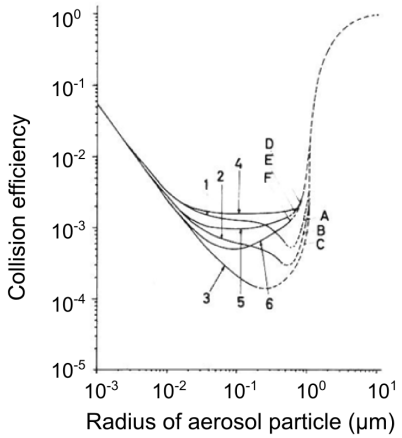

Figure 6.1: The effect of electric charges and relative humidity on the collision efficiency. The different curves relate to different combinations of electric charge and relative humidity. From Pruppacher and Klett (1978)

The largest differences in the scavenging coefficients between the three phases of precipitation can be seen for aerosol particle sizes above 30 nm (Fig. 5.16), and the minimum is most pronounced for liquid phase events. Most likely due to the higher efficiency of interception with a larger surface of hydrometeors, the minimum is less pronounced for solid phase events. For particles with diameters from 30 nm to 60 nm, solid phase events show the highest scavenging coefficients. While for larger aerosol particles mixed phase events are most efficient. This can be explained by a combination of a relatively complex surface structure and the relatively high vertical fall velocities of mixed phase hydrometeors with a high content of partially melted single and complex crystals. This combination makes the processes of interception and impaction more efficient. These processes are important for the removal of intermediate and larger aerosol particles.
All three types of precipitation show an increase of the mean scavenging coefficient with increasing precipitation intensity (Figs. 5.17, 5.18 and 5.19). With an exponent of $B = 0.25 \pm 0.001$ this tendency is most pronounced for liquid phase precipitation. In contrast, a smaller dependency on the precipitation rate and the lowest exponent of $B = 0.17 \pm 0.02$ is observed for solid

phase events. For solid phase events, parameters like the dominating crystal type of hydrometeors are also expected to play an important role.

6.5 Scavenging coefficients for different types of snowfall events

Taking the classification of solid phase precipitation with respect to the degree of riming and crystal type into account, the most dominant dependency can be seen for crystal type. Again, the largest differences can be observed for particles larger than 30 nm. Single crystals show the largest scavenging coefficient (Fig. 5.20 b). A possible reason for this tendency is the fact that single crystals are more affected by microscopic atmospheric turbulences than pellets or complex crystals and their path through the atmosphere is longer. As a consequence, single crystals have a relatively long residence time in the atmosphere and can collect more aerosol particles than for example pellets. In contrast, pellets have the smallest scavenging coefficient. They have a well defined trajectory and a shorter residence time in the atmosphere than single and complex crystals. Interestingly, the scavenging coefficient does not depend strongly on the degree of riming (Fig. 5.20 a). Compared to the crystal type, this parameter is not a strong indicator of surface structure.
Analyzing the scavenging coefficient in terms of micro physical parameters of hydrometeors, parameters reflecting the hydrometeor surface structure appear to have the strongest impact on the scavenging coefficient. For roundness and shape factor, a clear tendency towards higher scavenging coefficients for lower roundness and shape factor can be observed, for aerosol particles between 30 nm and 60 nm (Fig. 5.21). Also more elongated hydrometeors have a larger scavenging coefficient in that size range than less elongated ones. Such a systematic behavior can not be observed for the maximum dimension and the vertical velocity (Fig. 5.22). Hydrometeors with smaller volumes tend to show larger scavenging coefficients for particles larger than 30 nm. This behavior is consistent with the previous observation, taking into account that hydrometeors with larger elongation, smaller volume and lower roundness and shape factor are more likely single crystals.

6.6 Washout of particle bound radionuclides and the implementation into decision support systems

For the implementation of wet deposition of particle bound radionuclides into atmospheric transport models and decision support systems, the activity size distribution is an important parameter. For ^{7}Be and ^{210}Pb, activity size distributions with the highest activity concentrations for particles between 0.3 μm and 0.5 μm were measured (Fig. 5.23). Depending on variations in atmospheric processes, Winkler et al. (1998) measured median activity diameters from 0.44 μm to 0.74 μm for ^{7}Be and from 0.28 μm to 0.74 μm for ^{210}Pb in ground-level air at a semi-rural location in south Germany. In a study on activity size distribution of ^{7}Be in the Arctic atmosphere, Ioannidou and Paatero (2014) determined about 30% of the ^{7}Be activity to be within an aerosol particle diameter range from 0.39 μm to 0.69 μm. The aerosol particle diameters which showed maximum activity concentration for ^{7}Be and ^{210}Pb in the present study (300 nm to 500 nm) agree with these ranges. The activity size distribution for ^{137}Cs also shows a local maximum for aerosol particles with diameters between 300 nm and 500 nm. The diameter range with maximum activity concentration for ^{137}Cs found in the present study agrees well with the mean aerosol particle diameter of 0.4 μm used in literature (Stohl et al., 2012) for modeling wet deposition of ^{137}Cs.
The further analysis of wet deposition of particle bound radionuclides focused on aerosol particle diameters from 0.3 μm to 0.5 μm. This range contains the diameters with maximum activity concentrations measured in the present study. For this size range the scavenging coefficient is plotted as a function of precipitation rate for solid, mixed and liquid phase precipitation in Fig. 5.24. With an exponent of $B = 1.38 \pm 0.01$ liquid phase precipitation showed the strongest dependency on precipitation rate (Tab. 5.5). A relatively high value of $B = 0.7 \pm 0.08$ was also found for solid phase precipitation containing mainly pellets, while the weakest dependency on precipitation rate and the lowest values of $B = 0.45 \pm 0.01$ and $B = 0.39 \pm 0.01$ were found for complex crystals and mixed phase events respectively (Tab. 5.5). As reported in a review on the parameterization of wet deposition by Sportisse (2007), a wide spread for the values of A and B can be found in literature. A can spread from $10^{-6}\,\mathrm{s}^{-1}$ to $10^{-3}\,\mathrm{s}^{-1}$. In most cases B is between 0.5 and 1.0. The values found in the present study are in good agreement with the values reported in a study by Jylhä (1991) on scavenging of radioactive substances released from Chernobyl. She found A in a range from $1.6 \cdot 10^{-5}\,\mathrm{s}^{-1}$ to $4.0 \cdot 10^{-4}\,\mathrm{s}^{-1}$ and B between 0.3 and 1.2. The values found in the present work confirm

the assumption that the type of precipitation and the surface structure of solid phase hydrometeors play an important role for the parameterization of the scavenging coefficient.
The power function $\lambda = A \cdot (I/I_0)^B$ is commonly used in atmospheric transport models and decision support systems. Comparing the fitted power functions for solid and liquid phase events leads to the conclusion that solid phase events consisting of complex crystals or pellets have larger scavenging coefficients than liquid phase events, when the water equivalent precipitation rate is below $1.5\,\mathrm{mmh}^{-1}$. Solid phase events consisting of single crystals have larger scavenging coefficients than liquid phase events for precipitation rates lower than $2.0\,\mathrm{mmh}^{-1}$ (Fig. 5.25). Implementing wet deposition with the mentioned power function, solid phase precipitation events can have up to eight times higher scavenging coefficients than liquid phase events with the same water equivalent precipitation rate below $0.5\,\mathrm{mmh}^{-1}$. This can be one reason for the discrepancies between modeled and observed wet deposition mentioned for example by Morino et al. (2011) and Yasunari et al. (2011) in studies about deposition of radionuclides released during the Fukushima Dai-Ichi Nuclear Power Plant accident.
Additionally, for two precipitation events the decrease of atmospheric activity concentration was measured directly for the radionuclides ^{7}Be and ^{210}Pb (Fig. 5.26). On 14^{th} of January 2014 a solid phase precipitation event with a mean precipitation rate of $0.6\,\mathrm{mmh}^{-1}$ was detected. The corresponding activity scavenging coefficients calculated from two consecutive activity measurements are $(3.2 \pm 0.1) \cdot 10^{-4}\,\mathrm{s}^{-1}$ for ^{7}Be and $(2.8 \pm 0.4) \cdot 10^{-4}\,\mathrm{s}^{-1}$ for ^{210}Pb. These values are in good agreement with the scavenging coefficients calculated with the SMPS-measurement for aerosol particle diameters from $0.3\,\mu$m to $0.5\,\mu$m (Fig. 5.24 a). For a rain event with a precipitation intensity of $1.5\,\mathrm{mmh}^{-1}$ on 30^{th} of September the filter measurements yield a scavenging coefficient of $(2.2 \pm 0.2) \cdot 10^{-4}\,\mathrm{s}^{-1}$ for ^{7}Be and $(1.3 \pm 0.8) \cdot 10^{-4}\,\mathrm{s}^{-1}$ for ^{210}Pb (Fig. 5.26 (b)). These values are approximately half of the scavenging coefficients calculated with the SMPS-measurements (Fig. 5.24 c). One reason for the deviation may be that the high volume sampling station has no clearly defined cut-off size for aerosol particles. This means that also small hydrometeors and cloud droplets may be partially deposited on the filter, that, ideally, should only collect aerosol particles. Thus, the scavenging coefficient calculated with the filter measurement appears smaller.
Comparing the scavenging coefficients calculated for ^{7}Be to those calculated for ^{210}Pb, shows that the scavenging coefficients are very similar within the uncertainties. This is a strong indicator that ^{7}Be and ^{210}Pb are bound to aerosol particles with the same size, which was already confirmed by the activity size distribution measurements (Fig. 5.23).

The scavenging coefficients calculated with the filter measurements also confirm the previous observation that for precipitation rates below $1.5\,\mathrm{mmh}^{-1}$ snowfall can have higher scavenging coefficients than rain (see Fig. 5.25).

Chapter 7

Conclusion

The aim of the presented work was to analyze the mechanism of below-cloud scavenging for different types of precipitation including liquid, mixed and solid phase precipitation. The work focused on the differentiation between crystal types and surface structures of solid phase hydrometeors (e.g. snowflakes). Linking precipitation event classification, aerosol particle size dependent scavenging coefficients, activity size distributions and activity concentrations measured during precipitation events, detailed statements were formulated, regarding the efficiency of below-cloud scavenging of particle bound radionuclides in different types of precipitation events.
The presented study showed that 2D-Video Disdrometers are suitable instruments for measuring micro physical parameters of solid phase precipitation, after implementing a special matching algorithm. Decision tree based classification of solid precipitation events is possible with shape parameters and velocity of single hydrometeors, measured by means of a 2D-Video Disdrometer. For 34680 minutes of precipitation, aerosol particle size dependent scavenging coefficients were calculated with the results of SMPS-measurements. The scavenging coefficients showed good agreement with those reported in previous studies. In addition to the well established dependencies of the scavenging coefficient on aerosol particle size and precipitation rate, a clear dependence on the type of precipitation and on the crystal type of solid phase hydrometeors was found. The largest differences between the three phases of precipitation were found in the Greenfield gap and for aerosol particles larger than 60 nm. In the Greenfield gap, solid phase precipitation showed the highest scavenging coefficients, most likely due to a high efficiency of the interception mechanism which is important for intermediate aerosol particles. In case of solid phase precipitation, single crystal events showed the highest scavenging coefficients, followed by complex crystals. The lowest scavenging coefficients were found for events containing mainly pellets. To link these

results to the washout of particle bound radionuclides, activity size distributions were measured and the activity scavenging coefficients for ^{7}Be and ^{210}Pb were calculated on the basis of filter measurements. The results from these measurements showed good self-consistency and were in good agreement with the results from the SMPS-measurements.
One predominant result of this work is that wet deposition by different types of precipitation can be parametrized by different values for A and B using the equation $\lambda = A \cdot (I/I_0)^B$ where λ is the scavenging coefficient and I is the precipitation rate. In this work it was shown that, especially for precipitation rates of less than $1.5\,\mathrm{mmh}^{-1}$, the scavenging coefficients for snow can be significantly higher than those for rain. This can be one reason for the discrepancies between observed and predicted wet deposition as reported for the vicinity of Fukushima, Japan, after the Fukushima Dai-Ichi nuclear power plant accident. The values for A and B found in this study can easily be implemented to currently used decision support systems. To quantify the consequences of this implementation for wet deposition predictions, further studies are necessary. These studies should especially compare observed and predicted wet deposition in the near- and far field of a source of released radionuclides.
The presented work is a further step in better understanding wet deposition processes for particle bound radionuclides and therefore, it helps to better quantify the effects on human health induced by accidentally released radionuclides. Washout of atmospheric aerosol does not only concern human health but is also of high interest for the input of pollutants to our ecosystem. Further investigations should not only consider particle bound radionuclides but also other atmospheric pollutants which may have an impact on human health, such as soot. For weather forecast and climate modeling, wet deposition is also an important process. Finally, for further understanding of wet deposition, in-cloud processes should also be taken into account, and a more detailed differentiation between different hydrometeor types is necessary.

Bibliography

Andronache, C., Grönholm, T., Laasko, L., Phillips, V., and Venäläinen, A.: Scavenging of ultrafine particles by rainfall at a boreal site: observations and model estimations, Atmospheric Chemistry and Physics, 6, 4739–4754, 2006.

Arnold, D., Biernacka, M., Fischer, U., Isajenko, K., Jagielak, J., Lipinski, P., Wershofen, H., Zak, A., and Zarucki, R.: Practical Experience and Improvements in Aerosol Sampling for Trace Analysis of Airborne Radionuclides in Ground Level Air, Tech. Rep. PTB-Ra-42, Physikalisch Technische Bundesanstalt, 2000.

Atlas, D., Shrivastava, R., and Sekhon, R.: Doppler radar characteristics of precipitation at vertical incidence, Reviews of Geophysics and Space Physics, 2, 135, 1973.

Barthazy, E. and Schefold, R.: Fall velocity of snowflakes of different riming degree and crystal types, Atmospheric Research, 82, 391–398, 2006.

Barthazy, E., Goke, S., Schefold, R., and Högl, D.: An Optical Array Instrument for Shape and Fall Velocity Measurements of Hydrometeors, Journal of Atmospheric and Oceanic Technology, 21, 1400–1416, 2004.

Battaglia, A., Rustmeier, E., Tokay, A., Blahak, U., and Simmer, C.: PARSIVEL Snow Observations: A Critical Assessment, Journal of Atmospheric and Oceanic Technology, 27, 333–344, 2010.

Bell, D. A. and Saunders, C. P. R.: An experimental study of aerosol scavenging by hexagonal plate ice crystals, Atmospheric Research, 38, 9–19, 1995.

Birmili, W. and Wiedensohler, A.: New particle formation in the continental boundary layer: Meteorological and gas phase parameter influence, Geophysical Research Letters, 27, 3325–3328, 2000.

Birmili, W., König, K., Sonntag, A., Cheng, Y. F., Tuch, T., and Wiedensohler, A.: Ermittlung des nordhemisphärischen Hintergrunds an der GAW-Station Zugspitze unter besonderer Berücksichtigung des Ferntransportes von Feinstäuben, Tech. Rep. (UFOPLAN) 204 42 202/01, Leibniz-Institut für Troposphärenforschung e.V., 2007.

Brandes, E. A., Ikeda, K., Zhang, G., Schönhuber, M., and Rasmussen, R. M.: A Statistical and Physical Description of Hydrometeor Distributions in Colorado Snowstorms Using a Video Disdrometer, Journal of Applied Meteorology and Climatology, 46, 634–650, 2007.

Chate, D. M.: Below-thunderstorm rain scavenging of urban aerosols in the health hazardous modes, Natural Hazards, 56, 81–91, 2011.

Chate, D. M. and Pranesha, T. S.: Field studies of scavenging of aerosols by rain events, Aerosol Science, 35, 695–706, 2004.

Chate, D. M., Murugavel, P., Ali, K., Tiwari, S., and Beig, G.: Below-cloud rain scavenging of atmospheric aerosols for aerosol deposition models, Atmospheric Research, 99, 528–536, 2011.

Croft, B., Lohmann, U., Martin, R. V., Stier, P., Wurzler, S., Feichter, J., Posselt, R., and Ferrachat, S.: Aerosol size-dependent below-cloud scavenging by rain and snow in the ECHAM5-HAM, Atmospheric Chemistry and Physics, 9, 4653–4675, 2009.

Doering, C.: Measurements of the distribution and behaviour of Beryllium-7 in the natural environment, Ph.D. thesis, Queensland University of Technology, 2007.

Fabry, F. and Szyrmer, W.: Modeling of the Melting Layer. Part II: Electromagnetic, Journal of the Atmospheric Sciences, 56, 3593–3600, 1999.

Feind, R. E.: Comparison of three classification methodologies for 2D probe hydrometeor images obtained from the armored T-28 aircraft, Tech. rep., Institute of Atmospheric Sciences, South Dakota School of Mines and Technology, Rapid City, SD, USA, tech. Rep. SDSMT/IAS/R08-01, 2008.

Feng, J.: A size-resolved model for below-cloud scavenging of aerosols by snowfall, Journal of Geophysical Research, 114, D08 203, 2009.

Frank, G., Härtl, T., and Tschiersch, J.: The pluviospectrometer: classification of falling hydrometeors via digital image processing, Atmospheric Research, 34, 367–378, 1994.

Gavrilov, S., Kubo, M., Tran, V. A., Ngo, D. L., Nguyen, N. G., Nguyen, L. A. T., Lumbanraja, F. R., Phan, D., and Satou, K.: Feature Analysis and Classification of Particle Data from Two-Dimensional Video Disdrometer, Advances in Remote Sensing, 4, 1–14, 2015.

Graedel, T. E. and Franey, J. P.: Field measurements of submicron aerosol washout by snow, Geophysical Research Letters, 2, 325–328, 1974.

Grazioli, J., Tuia, D., Monhart, S., Schneebeli, M., Raupach, T., and Berne, A.: Hydrometeor classification from two-dimensional video disdrometer data, Journal of Atmospheric Measurement Technique, 7, 2869–2882, 2014.

Greenfield, S. M.: Rain scavenging of radioactive particulate matter from the atmosphere, Journal of Meteorology, 14, 115–125, 1957.

Gunn, R. and Kinzer, G. D.: The terminal velocity of fall for water droplets in stagnant air, Journal of Meteorology, 6, 243–248, 1949.

Hanesch, M.: Fall Velocity and Shape of Snowflakes, Ph.D. thesis, Swiss Federal Institute of Technology, Zürich (Supervisor: A. Waldvogel), 1999.

Heymsfield, A., Bansemer, A., and Schmitt, C.: Effective ice particle densities derived from aircraft data, Journal of the Atmospheric Sciences, 61, 982–1003, 2004.

Hiroshi, I.: Radar backscattering computations for fractalshaped snowflakes, Journal of the Meteorological Society of Japan, 86, 459–469, 2008.

Hoeve, J. E. T. and Jacobson, M. Z.: Worldwide health effects of the Fukushima Daiichi nuclear accident, Energy and Environmental Sciences, 5, 8743–8757, 2012.

Huang, G. J., Bringi, V. N., Cifelli, R., Hudak, D., and Petersen, W. A.: A methodology to derive radar reflectivity–liquid equivalent snow rate relations using C-band radar and a 2D Video Disdrometer, Journal of Atmospheric and Oceanic Technology, 27, 637–651, 2010.

Ioannidou, A. and Paatero, J.: Activity size distribution and residence time of ^{7}Be aerosols in the Arctic atmosphere, Atmospheric Environment, 88, 99–106, 2014.

Ioannidou, A. and Papastefanou, C.: Precipitation scavenging of ^{7}Be and ^{137}Cs radionuclides in air, Journal of Environmental Radioactivity, 85, 121–136, 2006.

Jiao, L. and Liu, Y.: Analyzing the shape characteristics of land use classes in remote sensing imagery, ISPRS Annals of Photogrammetry, Remote Sensing and Spatial Information Sciences, I-7, 135–140, 2012.

Joss, J. and Waldvogel, A.: Raindrop size distribution and sampling size error, Journal of the Atmospheric Sciences, 26, 566–569, 1969.

Jylhä, K.: Empirical scavenging coefficients of radioactive substances released from Chernobyl, Atmospheric Environment, 25A, 263–270, 1991.

Kruger, A. and Krajewski, W. F.: Two-Dimensional Video Disdrometer : A Description, Journal of Atmospheric and Oceanic Technology, 19, 602–617, 2002.

Kulan, A.: Seasonal ^{7}Be and ^{137}Cs activities in surface air before and after the Chernobyl event, Journal of Environmental Radioactivity, 90, 140–150, 2006.

Kyrö, E.-M., Grönholm, T., Vuollekoski, H., Virkkula, A., Kulmala, M., and Laakso, L.: Snow scavenging of ultrafine particles: field measurements and parameterization, Boreal Environment Research, 6095, 527–538, 2009.

Laakso, L., Grönholm, T., Rannik, U., Kosmale, M., Fiedler, V., Vehkamäki, H., and Kulmala, M.: Ultrafine particle scavenging coefficients calculated from 6 years field measurements, Atmospheric Environment, 37, 3605–3613, 2003.

Lim, S., Chandrasekar, V., and Bringi, V. N.: Hydrometeor Classification System Using Dual-Polarization Radar Measurements: Model Improvements and In Situ Verification, IEEE Transactions on Geoscience and Remote Sensing, 34, 792–801, 2005.

Liu, H. and Chandrasekar, V.: Classification of Hydrometeors Based on Polarimetric Radar Measurements: Development of Fuzzy Logic and Neuro-Fuzzy Systems, and In Situ Verification, Journal of Atmospheric and Oceanic Technology, 17, 140–164, 2000.

Locatelli, J. D. and Hobbs, P. V.: Fall speeds and masses of solid precipitation particles, Journal of Geophysical Research, 79, 2185–2197, 1974.

Löffler-Mang, M. and Joss, J.: An optical disdrometer for measuring size and velocity of hydrometeors, Journal of Atmospheric and Oceanic Technology, 17, 130–139, 2000.

Magono, C., Endoh, T., Harimaya, T., and Kubota, S.: Measurement of scavenging effect of falling snow crystals on the aerosol concentration, Journal of the Meteorological Society of Japan, 5, 407–416, 1974.

Marjamäki, M., Keskinen, J., Chen, D.-R., and Pui, D. Y. H.: Performance Evaluation of the Electrical Low-Pressure Impactor (ELPI), Journal of Aerosol Science, 31, 249–261, 2000.

Marshall, J. S. and Palmer, W. M.: The distribution of raindrops with size, Journal of Meteorology, 5, 165–166, 1948.

Mitra, S., Barth, U., and Pruppacher, H.: A laboratory study of the efficiency with which aerosol particles are scavenged by snow flakes, Atmospheric Environment, 24A, 1247–1254, 1990.

Morino, Y., Ohara, T., and Nishizawa, M.: Atmospheric Behavior, Deposition, and Budget of Radioactive Materials from the Fukushima Daiichi Nuclear Power Plant in March 2011, Geophysical Research Letters, 38, L00G11, 2011.

Nasstrom, J. S., Sugiyama, G., Baskett, R. L., Larsen, S. C., and Bradley, M. M.: The National Atmospheric Release Advisory Center modelling and decision-support system for radiological and nuclear emergency preparedness and response, International Journal of Emergency Management, 4, 524, 2007.

Nešpor, V., Krajewski, W. F., and Kruger, A.: Wind-Induced Error of Raindrop Size Distribution Measurement Using a Two-Dimensional Video Disdrometer, Journal of Atmospheric and Oceanic Technology, 17, 1483–1492, 2000.

Paramonov, M., Grönholm, T., and Virkkula, A.: Below-cloud scavenging of aerosol particles by snow at an urban site in Finland, Boreal Environment Research, 16, 304–320, 2011.

Pruppacher, H. R. and Klett, J. D.: Microphysics of Clouds and Precipitation, D. Reidell Publ. Co., Dordrecht, Holland, 1978.

Raskob, W. and Ehrhardt, J.: The RODOS System: Decision Support For Nuclear Off-Site Emergency Management In Europe, Tech. Rep. 99, Forschungszentrum Karlsruhe, Institut für Kern- und Energietechnik, 1999.

Roedel, W.: Physik unserer Umwelt: die Atmosphäre, Springer, Berlin, 3. Auflage, in German, 2000.

Sauter, D. P. and Wang, P. K.: An experimental study of the scavenging of aerosol particles by natural snow crystals, Journal of the Atmospheric Sciences, 46, 1650–1655, 1989.

Schaefer, V. J.: The preparation of snow crystal replicas-VI, Weatherwise, 9, 132–135, 1956.

Schumann, T., Zinder, B., and Waldvogel, A.: Aerosol and hydrometeor concentrations and their chemical composition during winter precipitation along a mountain slope — I. Temporal evolution of the aerosol, microphysical and meteorological conditions, Atmospheric Environment, 22, 1443–1459, 1988.

Schuur, T. J., Ryzhkov, A. V., Zrnic, D. S., and Schönhuber, M.: Drop size distributions measured by a 2D video disdrometer: Comparison with dual-polarization radar data, Journal of Applied Meteorology, 40, 1019–1034, 2001.

Sparmacher, H., Fuebler, K., and Bonka, H.: Below-cloud scavenging of aerosol particles: particle-bound radionuclides - experimental, Atmospheric Environment, 27A, 605–618, 1993.

Sportisse, B.: A review of parameterizations for modelling dry deposition and scavenging of radionuclides, Atmospheric Environment, 41, 2683–2698, 2007.

Starka, J. M., Zrinic, D. S., and Ryzhkov, A.: Bulk Hydrometeor Classification and Quantification Using Polarimetric Radar Data: Synthesis of Relations, Journal of Applied Meteorology, 39, 1341–1372, 2000.

Stohl, A., Seibert, P., Wotawa, G., Arnold, D., Burkhart, J. F., Eckhardt, S., Tapia, C., Vargas, A., and Yasunari, T. J.: Xenon-133 and caesium-137 releases into the atmosphere from the Fukushima Dai-ichi nuclear power plant: determination of the source term, atmospheric dispersion, and deposition, Atmospheric Chemistry and Physics, 12, 2313–2343, 2012.

Terada, H., Furuno, A., and Chino, M.: Improvement of Worldwide Version of System for Prediction of Environmental Emergency Dose Information (WSPEEDI), (I), Journal of Nuclear Science and Technology, 41, 632–640, 2004.

Terada, H., Katata, G., Chino, M., and Nagai, H.: Atmospheric discharge and dispersion of radionuclides during the Fukushima Dai-ichi Nuclear Power Plant accident. Part II: verification of the source term and analysis of regional-scale atmospheric dispersion, Journal of Environmental Radioactivity, 112, 141–154, 2012.

Thurai, M. and Bringi, V. N.: Drop axis ratios from a 2D video disdrometer, Journal of Atmospheric and Oceanic Technology, 22, 966–978, 2005.

Thurai, M., Szakall, M., Bringi, V. N., Beard, K. V., Mitra, S., and Borrmann, S.: Drop shapes and axis ratio distributions: comparison between 2D video disdrometer and wind-tunnel measurements, Journal of Atmospheric and Oceanic Technology, 26, 1427–1432, 2009.

Thurai, M., Williams, C. R., and Bringi, V. N.: Examining the correlations between drop size distribution parameters using data from two side-by-side 2D-video disdrometers, Atmospheric Research, 144, 95–110, 2014.

Thykier-Nielsen, S., Deme, S., and Mikkelsen, T.: Description of the Atmospheric Dispersion Module RIMPUFF, Tech. Rep. RODOS(WG2)-TN(98)-02, RisøNational Laboratory, 1999.

Tokay, A., Kruger, A., and Krajewski, W. F.: Comparison of Drop Size Distribution Measurements by Impact and Optical Disdrometers, Journal of Applied Meteorology, 40, 2083–2097, 2001.

Tschiersch, J., Frank, G., and Winkler, R.: Scavenging of aerosol-fixed radionuclides with rain and snow, Tech. Rep. BMU–2001-564, Bundesministerium fuer Umwelt, Naturschutz und Reaktorsicherheit, 2000.

UNSCEAR: Sources and Effects of Ionizing Radiation, Volume I: Report to the General Assembly, Sientific Annexes A and B; Volume II: Scientific Annexes C, D and E, Tech. Rep. UNSCEAR 2008, United Nations Scientific Committee on the Effects of Atomic Radiation, 2011.

Volken, M. and Schumann, T.: A Critical Review of Below-Cloud Aerosol Scavenging Results on Mt. Rigi, Water, Air and Soil Pollution, 68, 15–28, 1993.

Wahl, W.: $\alpha\beta\gamma$ Table - Radionuclide Handbook for Laboratory Workers in Spectrometry, Radiation Protection and Medicine, Tech. Rep. Version 4.3, Institute for Spectrometry and Radiation Protection, 2007.

Wang, X., Zhang, L., and Moran, M. D.: Uncertainty assessment of current size-resolved parameterizations for below-cloud particle scavenging by rain, Atmospheric Chemistry and Physics, 10, 5685–5705, 2010.

Wang, X., Zhang, L., and Moran, M. D.: On the discrepancies between theoretical and measured below-cloud particle scavenging coefficients for rain – a numerical investigation using a detailed one-dimensional cloud microphysics model, Atmospheric Chemistry and Physics, 11, 11 859–11 866, 2011.

Whitby, K. T.: The physical characteristics of sulfur aerosols, Atmospheric Environment, 12, 135–159, 1978.

Winkler, R., Dietl, F., Frank, G., and Tschiersch, J.: Temporal variation of ^{7}Be and ^{210}Pb size distributions in ambient aerosol, Atmospheric Environment, 32, 983–991, 1998.

Winkler, R. U. and Rosner, G.: Seasonal and long-term variation of 210 Pb concentration in air , atmospheric deposition rate and total deposition velocity in south Germany, The Science of the Total Environment, 263, 57–68, 2000.

WMO/GAW: WMO/GAW aerosol measurement procedures guidelines and recommendations, Tech. Rep. 153, World Meteorological Organization Global Atmosphere Watch, 2003.

WMO/GAW: WMO Global Atmosphere Watch (GAW) Strategic Plan: 2008 – 2015, Tech. Rep. 172, World Meteorological Organization Global Atmosphere Watch, 2007.

Xue, M., Droegemeier, K. K., and Wong, V.: The Advanced Regional Prediction System (ARPS); A multi-scale nonhydrostatic atmospheric simulation and prediction model. Part I: model dynamics and verification, Meteorology and Atmospheric Physics, 75, 161–193, 2000.

Yasunari, T. J., Stohl, A., Hayano, R. S., Burkhart, J. F., Eckhardt, S., and Yasunari, T.: Cesium-137 deposition and contamination of Japanese soils due to the Fukushima nuclear accident, Proceedings of the National Academy of Sciences, 108, 19 530–19 534, 2011.

Zhang, G., Xue, M., Cao, Q., and Dawson, D.: Diagnosing the intercept parameter for exponential raindrop size distribution based on video disdrometer observations: model development, Journal of Applied Meteorology and Climatology., 47, 2983–2992, 2008.

Zhang, G., Luchs, S., Ryzhkov, A., and Xue, M.: Winter Precipitation Microphysics Characterized by Polarimetric Radar and Video Disdrometer Observations in Central Oklahoma, Journal of Applied Meteorology and Climatology, 50, 1558–1570, 2011.

Zhang, L., Wang, X., Moran, M. D., and Feng, J.: Review and uncertainty assessment of size-resolved scavenging coefficient formulations for below-cloud snow scavenging of atmospheric aerosols, Atmospheric Chemistry and Physics, 13, 10 005–10 025, 2013.

Zikmunda, J.: Fall velocities of spatial crystals and aggregates, Journal of the Atmospheric Sciences, 29, 1511–1515, 1972.

Danksagung

- Diese Arbeit wurde gefördert vom Bundesministerium für Bildung und Forschung (BMBF) unter der Vertragsnummer 02NUK015B.

- Allen voran möchte ich jenen danken, die mit ihrer konstruktiven Kritik und ihren wertvollen Erfahrungen zum fachlichen Gelingen dieser Arbeit beigetragen haben. In diesem Sinne vielen Dank an Herrn Werner Rühm und Herrn Jochen Tschiersch.

- Wegen seiner kompetenten Beratung im Bereich der Aerosolphysik möchte ich ganz besonders Herrn Ludwig Ries vom Umweltbundesamt hervorheben. Beim Umweltbundesamt bedanke ich mich außerdem für das zur Verfügung stellen der SMPS-Daten.

- Dem Deutschen Wetterdienst danke ich für das Bereitstellen der Wetterdaten der Wetterstation Zugspitze.

- Einen großen Anteil am Gelingen dieser Arbeit hat meine Kollegin Kerstin Hürkamp. Durch ihre aufmunternden und motivierenden Beiträge fiel es leichter, unvermeidliche Durststrecken zu meistern.

- Vielen Dank, liebe Kollegen aus der Radioökologie, dafür, dass ihr mir bei allem so selbstverständlich geholfen habt.

- Herrn Martin Hagen vom Deutschen Zentrum für Luft- und Raumfahrt möchte ich dafür danken, dass er seine wertvolle Expertise mit dem 2DVD mit mir teilte.

- Herrn Stefan Kneifel von der Universität zu Köln danke ich für die Leihgabe des Pluvio-Sensors.

- Der gesamten Besatzung des Schneefernerhauses gebührt besonderer Dank, vor allem für ihre geduldige und tatkräftige Unterstützung bei Aufbau und Wartung der Messgeräte.

- Herrn Martin Schwinzerl, und Herrn Günter Lammer von Joanneum Research möchte ich für ihre kompetente Unterstützung bei der Behebung von Problemen verschiedenster Art mit dem 2DVD danken.

- Ganz besonders möchte ich in diesem Zusammenhang meine Familie erwähnen. Ohne ihre permanente Zuversicht, dass ich das Richtige tue, hätte sich meine Begeisterung für die Naturwissenschaft nicht entwickeln können.

- Vielen Dank, Ines, für Deine Geduld mit mir und dafür, dass Du es immer problemlos akzeptiert hast, wenn ich tage- und nächtelang auf der Zugspitze verschwunden war.

Publikationen

Veröffentlichungen (Peer reviewed)

- Bernauer, F., Hürkamp, K., Rühm, W. and Tschiersch, J., On the consistency of 2D-video disdrometers in measuring microphysical parameters of solid precipitation, *Atmos. Meas. Tech.*, 8, 3251–3261, 2015

- Bernauer, F., Hürkamp, K., Rühm, W. and Tschiersch, J., Snow event classification with a 2D-Video Disdrometer - a decision tree approach, *Atmos. Res.*, submitted, 2015

- Bernauer, F., Hürkamp, K., Ries, L., Rühm, W. and Tschiersch, J., Below cloud scavenging for different types of precipitation, ..., in preparation

Vorträge

- Bernauer, F., Hürkamp, K., Shinonaga, T., Rühm, W. and Tschiersch, J., Atmospheric washout of radioactive aerosols in case of snow, *Seminar of the Department of Radiation Sciences, Helmholtz Zentrum München*, 13^{th} of April 2015

- Bernauer, F., Schwinzerl, M., Hürkamp, K., Rühm, W. and Tschiersch, J., Ground Based In-situ Measurements of Snow Fall with a 2D-Video Distrometer on Mt. Zugspitze, Germany, *Verhandl. DPG (VI)*, 50,4, 2015

Posterpräsentationen

- Bernauer, F., Hürkamp, K., Rühm, W. and Tschiersch, J., Ground Based In-situ Measurements of Snowfall with a 2D-Video Distrometer on Mt. Zugspitze, Germany, *American Geophysical Union Fall Meeting*, December 15^{th} - 19^{th} 2014

- Bernauer, F., Ries, L., Hürkamp, K., Rühm, W. and Tschiersch, J., Scavenging of Ultra Fine Particles in Different Types of Snowfall Events, *International Aerosol Conference*, Busan, Korea, August 28^{th} - September 2^{nd} 2014

- Bernauer, F., Hürkamp, K. and Tschiersch, J., Washout Coefficients for Particle Bound Radionuclides in Rain and Snow Events, *Verhandl. DPG (VI)*, 48,4, 2013

Eidesstattliche Versicherung

Bernauer, Felix

Name, Vorname

Ich erkläre hiermit an Eides statt,

dass ich die vorliegende Dissertation mit dem Thema

Atmospheric washout of radioactive aerosol for different types of precipitation events

selbständig verfasst, mich außer der angegebenen keiner weiteren Hilfsmittel bedient und alle Erkenntnisse, die aus dem Schrifttum ganz oder annähernd übernommen sind, als solche kenntlich gemacht und nach ihrer Herkunft unter Bezeichnung der Fundstelle einzeln nachgewiesen habe.

Ich erkläre des Weiteren, dass die hier vorgelegte Dissertation nicht in gleicher oder in ähnlicher Form bei einer anderen Stelle zur Erlangung eines akademischen Grades eingereicht wurde.

München, 22.05.2015

Ort, Datum

Unterschrift Doktorandin/Doktorand